Properties of Rotating Compact Stars with Exotic Matter

THESIS

Submitted in partial fulfillment
of the requirements for the degree of
DOCTOR OF PHILOSOPHY

By

SMRUTI SMITA LENKA
ID No. 2013PHXF0417H

Under the supervision of

Prof. SARMISTHA BANIK

BITS Pilani
Pilani | Dubai | Goa | Hyderabad

BIRLA INSTITUTE OF TECHNOLOGY AND SCIENCE, PILANI
February 2019

BIRLA INSTITUTE OF TECHNOLOGY AND SCIENCE, PILANI

Certificate

This is to certify that the thesis entitled, "**Properties of Rotating Compact Stars with Exotic Matter**" and submitted by SMRUTI SMITA LENKA, ID No. 2013PHXF0417H for award of Ph.D. of the Institute embodies original work done by her under my supervision.

Signature of Supervisor
Prof. SARMISTHA BANIK
Associate Professor,
Birla Institute of Technology and
Science-Pilani, Hyderabad Campus
Date:

Acknowledgements

This thesis would not have been possible without the help of several individuals who in one way of the other extended their valuable assistance in the completion of this study.

First and foremost, my utmost gratitude to my supervisor Prof. Sarmistha Banik. It has been a real honor to be her PhD student. She has always kept her door open to answer my unending queries and guided me in the right direction. Her energy and enthusiasm for theoretical physics is contagious and has motivated me during the tough period of PhD. I could not have asked for a better advisor.

I would like to thank my institute Birla Institute of Technology and Science-Pilani, Hyderabad for giving me an opportunity to carry out my research work. I greatly acknowledge Department of Science and Technology, Government of India for providing the funding through INSPIRE fellowship which made my PhD work possible.

I express my sincere thanks to Dr. Rahul Nigam and Dr. Sashideep Gutti who kindly agreed to serve as my Doctoral Advisory Committee (DAC) members. Their constructive suggestions helped me to improve the quality of my thesis.

I take the opportunity to thank Head of the Department, all the faculty members and staffs of Department of Physics for being helpful at every point of time. I would also like to thank my colleagues at my institute who provided me a healthy environment to work. I would like to thank my collaborator Dr. Prasanta Char for his help and support. I express my gratitude to my research group members Dr. Neelam D. Batra and Mr. Krishna P. Nunna for their help. I am thankful to my friends Prakruti, Priyanka, Kiran and Rahul for making my Phd journey enjoyable. I would like to specifically thank Ms. Ramadevi for being a constant source of support and motivation for me.

I would like to thank my parents, in-laws, siblings, and friends for their constant support and motivation. Special thanks to my husband for encouraging me throughout my PhD journey and being patient with me at every point of time. My love to my son, Ayansh for being a stress buster during this period.

Last but not the least, my sincere gratitude to the almighty.

Thank you

Smruti Smita Lenka

Abstract

Neutron stars are believed to be born in the aftermath of type II supernova explosions, that occur when a massive star (M$\geq 8M_{solar}$) exhaust all its nuclear fuel. Almost all physical properties of neutron stars are extreme compared to other objects found in the universe. They are the densest form of matter, existed in the present universe with a mass in the range of M$\sim 1-2M_{solar}$, confined in a sphere of radius R $\sim$ 10 kms. Being tiny, massive and at the same time located far ($\sim$ few hundred pc) from us, the direct observation of the neutron star (NS) interior is not feasible. Several theoretical models have been predicted to construct the equation of state (EoS) i.e. the relation between pressure and energy density for NS matter and study the NS interior structure. EoS of the high density core constitutes a key input for determining the structure of the NS. In real astrophysical environment NSs typically have a non-zero angular momentum. Various structural properties (mass, radius, moment of inertia etc.) are closely related to the dynamics and hence the observable properties of pulsars, the rotating NSs. This, on the other hand, gives an insight about the high density matter relevant to NSs. Any model that doesn't satisfy the observational constraints are ruled out.

More than three decades of theoretical investigations, we are yet to reach any consensus on the EoS of NSs interior. It can be a few times denser than the normal nuclear matter and is comprised of neutrons, protons and leptons. However, for such a high density, other intriguing possibilities exist. These include the appearance of strange particles in the form of hyperons and/or Bose-Einstein condensation of K^- mesons. In this thesis, we construct the EoS for isolated, non-magnetic and cold NS matter with hyperons and antikaon condensates following the relativistic mean field (RMF) model with density dependent (DD2) couplings. We investigated the static structural properties such as mass, radius for such a perfectly spherical NS. We also study the structural properties of massive, rapidly rotating, and cold NSs and calculate their mass, radius, moment of inertia, angular momentum and quadrupole moment for a fixed baryonic mass. Also, we follow the quasi-stationary evolution of a rotating star along constant rest mass sequences. Next, we investigate the quasi-stationary evolution of a lepton-rich neutrino-trapped protoneutron star (PNS) in an approximate way at four different stages. For this, we construct EoS of hot NS at constant entropy per baryon. The static mass, energy density and temperature profiles are generated for these EoSs. The role of the exotic matter on the structural parameters are thoroughly investigated.

The other focus of the thesis is to study the universality relations and check the role of the strange particles on them. Recently it has been observed that there exist universal relations between the characteristic NS parameters that are to a very good approximation independent of the NS's internal structure. These studies are not only theoretically simulating, they also provide a practical way to improve the measurement accuracy of NS properties substantially by

distinguishing NSs from strange stars, and testing general relativity in a NS structure–independent fashion. However, the earlier works were limited to nuclear matter EoS. To explore the universality relations in the presence of exotic matter, we calculate the dimensionless critical mass and studied its variation with normalized angular momentum. Next, we move on to the universal relations between normalized momentum of inertia and compactness ($\mathcal{C}$:=M/R) for the hot and young compact object. Universal relations are investigated for fixed frequency stars. Since the relations are not exact, we investigate the validity in different physical regimes i.e. from low compactness to high compactness. Our study continued to calculate the quadrupole moment, love number and tidal deformability to account for the rotation powered deformation of the star.

Contents

List of Figures

List of Tables

Abbreviations

AMANDA	Antarctic Muon And Neutrino Detector Array
ANTARES	Astronomy with a Neutrino Telescope and Abyss environmental Research
ATHENA	Advanced Telescope for High Energy Astrophysics
BH	Black Hole
CXO	Chandra X-ray Observatory
DD	Density Dependent
EFLD	Equilibrium Flux-Limited Diffusion
EFT	Effective Field Theory
EoS	Equation of State
FAST	Five-hundred-meter Aperture Spherical radio Telescope
FGST	Fermi Gamma-ray Space Telescope
G	Gauss
GR	General Relativity
GRB	Gamma Ray Burst
GW	Gravitational Wave
HETE	High Energy Transient Explorer
Hz	Hertz
IMB	Irvine-Michigan-Brookhaven
INO	India-based Neutrino Observatory
INTEGRAL	International Gamma-Ray Astrophysics Laboratory
K	Kelvin
KEH	Komatsu Eriguchi Hachisu
kg	Kilogram
kHz	Kilo Hertz

km	Kilometre
KM3NET	Cubic Kilometre Neutrino Telescope
LIGO	Laser Interferometer Gravitational-Wave Observatory
LISA	Laser Interferometer Space Antenna
LMXB	Low Mass X-ray Binary
LORENE	Langage Objet pour la RElativité NumériquE
m	metre
MeV	Mega electron Volt
MHz	Mega Hertz
ms	milli second
NICER	Neutron star Interior Composition Explorer
NS	Neutron Star
pc	parsec
PN	post Newtonian
PNS	Protoneutron Star
PSR	Pulsar
RMF	Relativistic Mean Field
RXTE	Rossi X-ray Timing Explorer
s	second
SKA	Square Kilometer Array
SN	Super Novae
SNO	Sudbury Neutrino Observatory
SO	Spin-Orbit
TOV	Tolman Oppenheimer Volkoff
VLT	Very Large Telescope
XMM	X-ray Multi Mirror

Physical Constants

Boltzmann Constant	k_B	$=$	1
Gravitational Constant	G	$=$	1
Speed of Light	c	$=$	1

Chapter 1

Introduction

1.1 Neutron Stars

NSs are the densest form of matter found in the universe. Landau, in the year 1931, was the first person to speculate the existence of a star, more compact than white dwarfs containing very dense matter. The possible existence of NS was proposed by Baade and Zwicky [1] in 1934 only two years after the discovery of neutrons by Chadwick. They coined the term 'supernovae' and predicted the existence of NS as the end product of SNe explosions, while Landau anticipated a single-nucleus star. Five year later, Robert Oppenheimer and George Volkoff derived the equations that describe the structure of a static star with spherical symmetry in general relativity and performed the first theoretical calculations to estimate the upper mass limit of NS mass [2]. Tolman [3] also did the calculations independently in the same year. Incidentally, Chandrasekhar and von Neumann already obtained the same equations of hydrostatic equilibrium in 1934, but they did not publish their results. Oppenheimer and Volkoff considered a matter consisting of non-interacting neutrons and got a very low value ($0.7M_{solar}$) for the maximum mass of the stable static NS, that was quite smaller than the Chandrasekhar mass limit of white dwarfs i.e. $1.44M_{solar}$. The low upper limit indicated the importance of a realistic EoS of the NS matter, or in other words, the role of the fundamental nuclear forces became evident.

Towards the end of the year 1945, people started working on the formulation of more realistic EoS for NS matter. The EoS for a non-interacting neutron-proton-electron gas under β-equilibrium condition was constructed by Harrison et. al in mid 1950s [4]. Cameron [5] investigated the effect of nucleon-nucleon interaction on the EoS and structure of a NS of maximum mass $\sim 2M_{solar}$ by using Skyrme-type forces [6]. He was also the first person to investigate the effect of hyperons in NS. One year later, Salpeter studied the role of hyperon in NSs [7]. Ambartsumyan and Saakyan presented the first detailed calculation of the EoS for the NS matter which is composed of an equilibrium mixture of degenerate free Fermi gases of baryon, mesons and leptons [8]. The effect

of baryon-baryon interaction on the dense matter EoS with hyperon content was studied by Tsuruta and Cameron [9]. Various studies show the role of pion condensates on NS properties [10, 11, 12]. Kaplan and Nelson investigated kaon condensation in NS matter in the year 1986 [13]. The nuclear EoS model proposed by Walecka and Serot in the year 1986 is the most commonly used model [14]. On the other hand, just after a year of the introduction of quark model [15, 16], Ivanenko and Kurdgelaidze investigated the existence of deconfined quark matter in NS core in 1965 [17, 18]. Though many authors have paid their effort to construct the EoSs for describing the extreme NS interior, still the exact nature of EoS at very high density is unknown [19].

Despite the theoretical efforts, the astronomical community took almost thirty years to take the NS idea seriously until Jocylen Bell and Antony Hewish discovered the first pulsar (PSR) in 1967 accidentally. This source was identified to have a frequency of 81.5 MHz with a pulsating period of 1.377 s. Pulsars are rotating NSs with strong magnetic field and remarkable stable pulse period and was the first observational evidence for NS. Their magnetic axes are not aligned to their rotation axes and the continuous radio emission from the magnetic poles sweeps our line of sight periodically. However, this identification of pulsars with NS took some more theoretical explanation. Gold [20] predicted a small increase in the period due to loss of rotational energy through radiation, that was observationally confirmed when a slowdown of the Crab PSR was discovered. The Crab nebula is the remnant of the historical supernova explosion observed by Chinese astronomers in 1054 A.D. The simultaneous discoveries of the Crab and the Vela PSR in 1968, both of which are located in supernova remnants, confirmed the prediction of Baade and Zwicky that the NSs are formed in supernova explosions. The NS observation took a further step when Hulse and Taylor [21] discovered the first binary pulsar PSR J1913+16 in 1974. Even though PSRs were first discovered as radio sources, optical telescopes and several satellites with onboard X-ray and γ-ray telescopes have been able to observe more than 2000 PSRs till date [22].

1.2 Observational scenario

NSs are nature's own unique laboratories to study matter under extreme conditions of gravity and density. Such a cold and dense matter is not reachable in terrestrial facilities. They are very compact objects with mass $\sim 1.5-2M_{solar}$ in a sphere of ~ 10 km radius and rotational period of 1.5 ms–1000 s. NS observations are very difficult to measure mainly because they are very small objects and are far away from us. Thanks to new generations of X-ray and γ-ray facilities (e.g. Chandra, XMM-Newton, Swift, Integral, Agile, Fermi) as well as ground-based radio telescopes, the observational study of NS has entered into a new era. The X-ray instrument onboard ASTROSAT, the space based Indian observatory, can reveal characteristics of X-ray PSRs in a wide temporal range. In addition, new ambitious projects, such as the gravitational-wave (GW)

detectors Advanced LIGO and Advanced VIRGO are being completed, and even more ambitious projects are in the pipeline [23, 24]. Particularly, the Square kilometer array (SKA) telescope will take a leading role in the study of fundamental physics in strong gravitational fields of PSRs and black holes. Apart from the obvious discovery of many more PSRs (even those with very low luminosity), and the extremely accurate timing analysis of the current PSR population, SKA will measure moment of inertia (I) of a PSR quicker than what is possible presently thanks to its extraordinary sensitivity and large field of view.

1.2.1 Telescopes for NS observations

The NSs are unique objects whose emission encompasses all the available multi-messenger tracers: electromagnetic waves (ranging from radio, infrared, optical, ultraviolet, X-ray and γ-ray), cosmic rays, neutrinos, and gravitational waves. We briefly review few aspects of their observation starting with the different types of telescopes that are used.

Electromagnetic Observations: PSR astronomy research has come a long way, since the discovery of first radio pulse by Jocylyn Bell and Antony Hewish on the so-called "dipole array". This is no longer in use. The Lovell telescope at Jodrell Bank Observatory (Manchester, UK) and the Parkes (Australia), Arecibo (Puerto Rico), Nançay (France), Effelsberg (Germany), the Green Bank Telescope (USA) and LOFAR (Netherlands) are some of the active radio telescopes in pulsar research. The high sensitivity of the GMRT at Pune, India makes it an outstanding telescope for pulsar surveys at low frequencies ($\lesssim$ 800 MHz). The Five-hundred-meter Aperture Spherical radio Telescope (FAST) is world's largest single-dish telescope, built in China. The SKA, world's largest radio telescope, is expected to begin operation early in the next decade [25].

The high precision timing technique in the SKA would quicken the determination of I of the double PSR J0737-3039A. The distinguishable effect of PSR moment of inertia on the PSR timing in SKA will be of the order of the 2PN level correction to the advance of periastron $\dot{\omega}$, due to highly improved precision of timing measurements over its predecessors. It can also measure I by estimating the spin-orbit misalignment angle δ in double NSs. SKA can potentially discover highly relativistic binaries, exotic system like PSR-black hole (BH) binary and sub-millisecond PSR [26]. Simultaneous measurement of high mass and high spin stars would be particularly helpful in constraining the mass-radius (M-R) relation, which is closely related to our EoS studies.

The Neutron star Interior Composition Explorer (NICER) is a NASA Explorers program, dedicated to the study the extraordinary gravitational, X-ray, and nuclear physics environments embodied by NS. Large ground-based telescopes like the Very Large Telescope (VLT) in the Atacama desert in Chile can be used to perform observations in the near infrared and the optical bands. Observations in the extreme ultraviolet, X-ray and γray require the use of space

observatories. Hubble Telescope normally sees NS in X-rays, γ-rays, and radio waves. The Chandra X-ray Observatory (CXO), the X-ray Multi Mirror (XMM-Newton) and the Rossi X-ray Timing Explorer (RXTE) perform observation in X-ray while the High Energy Transient Explorer (HETE-2), the International Gamma-Ray Astrophysics Laboratory (INTEGRAL) and the Fermi Gamma- ray Space Telescope (FGST) do it in γ-rays [19].

Although NSs are of interest in many areas of physics, our study is deeply connected to the interplay between nuclear and astrophysics. We look forward to the new generation of exotic beam facilities in France (SPIRAL), Germany (FAIR), Japan (RIKEN, J-PARC), USA (RIA) or the EU (EURISOL); their experimental studies of very exotic nuclei would allow us probe the fundamental nuclear interaction [19].

Neutrino Observations: The birth of NS in supernova explosions is accompanied by the most powerful neutrino burst. The emission of neutrinos and antineutrinos of three flavors take an important role in the cooling of the newly born hot neutron stars (PNS). Neutrinos carry away most of the gravitational binding energy of the compact remnant and drives its evolution from the PNS to the cold final state (NS). It is followed by the emission of photons at the surface. The supernova explosion, SN1987A, in the Giant Magellanic Cloud has been an amazing and extraordinary event; approximate 25 events were observed in real time in three different experiments: Kamiokande II (12), Irvine-Michigan-Brookhaven (IMB) (8), and Baksan (5) in a burst lasting less than 13 seconds. The under-ice telescopes AMANDA (Antarctic Muon And Neutrino Detector Array) in the South Pole and the under-water projects ANTARES (Astronomy with a Neutrino Telescope and Abyss environmental Research), and the underground observatory SNO (Sudbury Neutrino Observatory) located 2100 meters underground in Ontario, Canada have provided us with valuable data. A few thousands of neutrinos from the next Galactic supernova are expected to be captured in deep-underground experiments like IceCube at the South Pole, SuperKamiokande in Japan, KM3NET (Cubic Kilometre Neutrino Telescope) in the Mediterranean sea, and Borexino in the Gran Sasso Laboratory. Unfortunately lots of social movements have stopped the construction of India based neutrino observatory (INO).

Gravitational wave Observations: On August 17, 2017 the GW signal from a binary NS merger was detected [27] for the first time by the Advanced LIGO (Laser Interferometer Gravitational-Wave Observatory) and Advanced VIRGO (from the European Gravitational Observatory) collaborations. This historic detection, GW170817, has ushered in a new era of NS observations and has provided us with a new tool to explore the EoS at large densities and obtain information on the structural properties such as mass and radii [28]. GWs from the oscillation modes of NSs or during the coalescence of NS binaries or BH-NS binaries can also be a valuable source of information. When two NSs orbit each other very closely, they spiral inward due to gravitational radiation with time. As the two stars meet, their merger results in the formation of either a more massive NS or a BH. The mergers marks the first cosmic event observed in both

gravitational waves and electromagnetic waves. As the two NSs spiraled together, they emitted gravitational waves that were detected for about 100 seconds. When they collided, a flash of light in the form of γ rays was emitted and seen on Earth about two seconds after the GW detection. In the days and weeks following the merger, other forms of electromagnetic radiation such as X-ray, ultraviolet, optical, infrared and radio waves, were detected, making the event truly multi-messenger.

The detected signal of GW, GW170817 manifest many interesting facts about dense NS matter. Having a combined signal-to-noise ratio 32.4, this GW-signal is loudest one observed till date. They found the component masses to be in the range 1.17–1.60 M_{solar} and the total mass of the system as $2.74^{+0.04}_{-0.01}$ M_{solar} for low spin prior. The detection of a short ($\sim 2s$) gamma ray burst, GRB 170817A after 1.7 s of the coalescence time provides a clear evidence of association of short gamma ray bursts with NS mergers. This discovery yields important information about short GRB, binary chirp mass, tidal deformability and dense matter in NS interior along with GW speeds and heavy element synthesis through r-process. The observation of GW170817 has provided the chirp mass $M_c = \frac{(m_1 m_2)^{3/5}}{(m_1+m_2)^{1/5}}$ of the binary system, where m_1 and m_2 are the individual masses of the binary NS [27]. The tidal deformability depends inherently on the properties of NS. The phase-shift analysis of the observed signal has set a limit to the tidal deformability parameter, which on the other hand limits the NS radius between 12 and 13 km and excludes very soft EoS [29]. The observational data from GW event GW170817 and NS mass limit of $M_{max} \geq 1.97 M_{solar}$ in conjunction with laboratory measurements of neutron skin thickness have constrained the EoS more stringently [30]. The future European Space Agency mission LISA (Laser Interferometer Space Antenna) is planned to be launched approximately in 2034 and LIGO-India is expected to be ready by 2024. The combined input of all these projects will be crucial to collect data to advance our understanding of compact stars.

1.2.2 NS Observable

NSs are very strange objects. Newly born NSs are hot with a temperature of $10^{11} - 10^{12}$ K, but they cool down to around 10^9 K on a timescale of a day due to neutrino emission. NSs are really massive objects having masses in the order of M_{solar} (mass of sun) and have smaller radii $\sim$ 10 kms. These are highly dense with core density $\sim 10^{17}$ kgm^{-3}. They have largest magnetic field strength $\sim 10^{15}$ G. These are believed to be the only place in the universe except for the big bang where neutrinos become trapped. In this section, we discuss some of the gross properties such as, mass (M) and radius (R) that are determined from observations. These measured quantities can shed light on the EoS, composition etc.

Mass: Out of estimated total galactic population of a few tens of thousands of pulsars beaming towards the earth, we observed $\sim$ 2500 radio PSRs in our galaxy so far [22]. Among these known

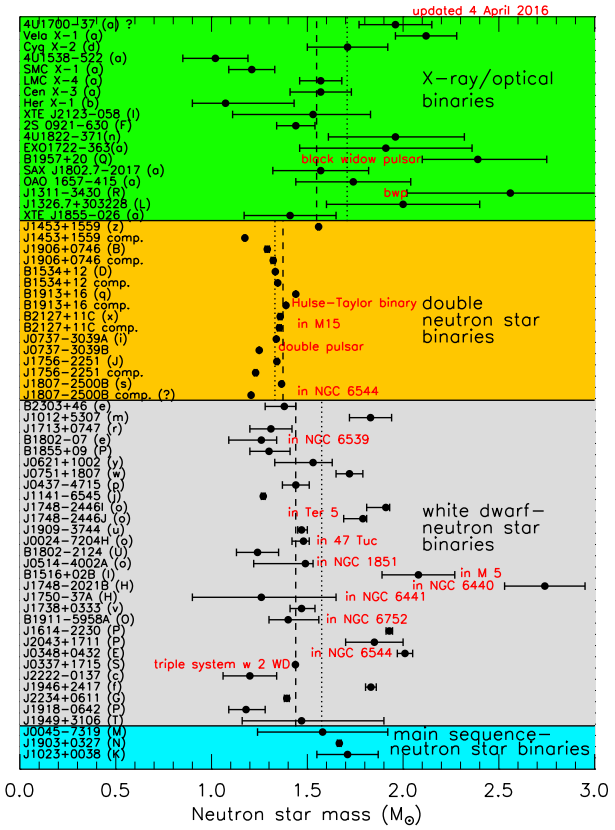

FIGURE 1.1: Neutron Star Mass
Picture Courtesy: J. Lattimer, Annual Review of Nuclear and Particle Science, Vol. 62, 485, 2012

sources, fewer than 10% are in binary systems and only their mass could be measured precisely using Shapiro delay or a combination of post-Keplerian orbital parameters such as orbital period decay, advance of periastron, and constraints from spectroscopic modeling of the companion star [26]. The Hulse-Taylor pulsar, PSR J0737-3039 is one of the best studied PSR in the NS binaries. Masses are determined not only for double NS systems, but for several NS-white dwarf binaries as well, since they allow measurement of orbital period decay. Mass of accreting NSs can also be constrained by measuring the motion and spectral properties of the companions, but this process has large uncertainties. Currently the accurately measured high-mass pulsars are PSRs J1614-2230 and J0348+0432 with masses 1.928 ± 0.017 and $2.01 \pm 0.04\, M_{solar}$ respectively [31, 32, 33]. The first major observational constraint of the EoS came from these $2M_{solar}$ mass observations, that rule out most of the soft EoS, as the matter pressure is not sufficient enough to support stars to maintain this maximum mass limit against gravitational collapse. Measured and estimated masses with 1σ uncertainties for NSs in radio binary pulsars and in x-ray accreting

binaries are summarized in Fig. 1.1. Vertical dotted lines show the average masses of each group ($1.62M_{solar}$, $1.33M_{solar}$, and $1.56M_{solar}$).

Radius: Besides mass the other important observable of the NS is radius. However, a possible way to determine R is to use the thermal emission of low-mass X-ray binaries. The observed X-ray flux (F) and temperature (T), assumed to be originated from a uniform blackbody, together with the distance (D) of the star can be used to obtain an effective radius,

$$R_{\infty} = \sqrt{\frac{FD^2}{\sigma T^4}}. \tag{1.1}$$

where, σ is the Stefan-Boltzmann constant and the NS radius can be obtained from R_{∞} by using the relation,

$$R = R_{\infty}\sqrt{1 - \frac{2GM}{c^2 R}}. \tag{1.2}$$

Here, M is the mass of the star. However, simultaneous M-R measurement for a single NS is yet to come. There are several methods to constrain R utilizing various properties of thermonuclear bursts, accretion-powered millisecond PSRs, kHz QPOs, relativistic broadening of iron lines, quiescent emissions, and binary orbital motions, but they are not free from systematic uncertainties [34]. These systematic errors in current radius estimation are so large that they are not useful inputs to nuclear theories. Independent M and R measurement for the same compact star without invoking their combination, for example red-shift, is yet to happen due to various uncertainties such as the estimated distance of the source, the unknown chemical compositions of the atmosphere, interstellar absorption, and the presence of magnetic field [35]. Currently, transient low-mass X-ray binaries (LMXBs) can give reliable constraints on radii, as their atmosphere can be reliably modelled and their distance in globular clusters can be accurately determined [28]. Further information on radii are expected from high-precision telescopes and missions like SKA [25], NICER [36], and ATHENA [37] in near future.

Spin frequency: The mass-radius profiles from different models can intersect among themselves. Therefore, we need a third independent parameter to constrain the EoS, i.e. spin, which is the first measured quantity. So, at least three independent global parameters, for example, mass, radius and spin frequency, of the same star are required in order to constrain the EoS models, and hence to understand the dense core [34].

NSs are mostly observed in radio and are known as PSRs. The major part of the known NSs are observed as radio PSRs, many of which exhibit very stable rotational periods of approximately 1 ms to 10 s [22]. Most of the PSRs discovered so far, take nearly $\sim$ 0.6 s to complete one revolution. Depending on the observed rotation period, PSRs can be classified into two different classes i) the normal PSRs with rotational periods of the order of $\sim$ 1s, ii) the millisecond PSRs with rotational periods of $\sim$ 0.001 s. A young PSR rotates rapidly whereas an old one rotates slowly. The maximum spin frequency for a star of mass M and radius R can be estimated as

$\nu_{max} = 1250Hz \left(\frac{M}{M_{solar}}\right)^{1/2} \left(\frac{R}{10km}\right)^{-3/2}$[38]. Interestingly, this can be as high as $\sim$ 1500–2000 Hz, beyond which a self-gravitating star would fly apart due to centrifugal acceleration. Till date the highest frequency of a PSR ever established is 716 Hz, for PSR J1748–2446ad in the globular cluster Terzan 5 [39]. However, the highest spin frequency of a NS in a binary with another NS is only 44 Hz [40]. The slowest one, observed in 2011, takes an exceptionally large amount of time (1062 s) compared to the rest [41].

Owing to highly accurate PSR timing, the rotational period $\mathcal{P}$ and the first time derivative $\dot{\mathcal{P}}$ and in certain cases, even the second $\ddot{\mathcal{P}}$ of many radio PSRs have been observed. The famous $\mathcal{P}$ $\dot{\mathcal{P}}$ diagram encodes a lots of information about the PSR age, its magnetic field strength or spin-down power.

1.3 Birth of a NS

A massive progenitor star ($\geq 8M_{solar}$) completes all the nuclear burning phases starting from hydrogen to silicon burning towards the end of its life cycle. It leaves a core consisting of mainly iron-56 nuclei which is surrounded by concentric shells of silicon, oxygen, neon, carbon, helium and hydrogen. Iron-56, having the maximum binding energy, can't undergo further thermonuclear fusion to release energy. The core contracts raising its temperature which results in breaking the iron nuclei to lighter nuclei and free nucleons through nuclear photodisintegration. Free electrons combine with protons to produce neutrons by electron capture process which is also referred as neutronization. As soon as the core reaches nuclear densities, a strong repulsive nuclear force comes into existence and suppresses further collapse. The collapsing core starts rebound and generates a shock wave. This shock wave travels through the infalling material and blows out the stellar envelope. This is called as type II supernova explosion. When the mass of core exceeds the Chandrasekhar mass limit (1.44 M_{solar}), it may collapse to a BH under its own gravity. The lepton rich and neutrino-trapped, hot (T$\sim$ few tens of MeV) collapsed core may settle into hydrostatic equilibrium after few milliseconds of the bounce. This is known as the PNS. Neutrino diffusion carries out most of its energy leaving behind a cold NS.

1.4 NS Structure

The NS structure can be split into four main layers: an outer crust, an inner crust, an outer core and the inner core (see Figure 1.2). These layers are surrounded by an atmosphere. Different particle species and states of matter are believed to be present in different density regimes. The outer parts of the star consist of an elastic crust of neutron-rich atomic nuclei, permeated by superfluid neutrons. In the outer core, the protons coexist as superconducting fluid along with

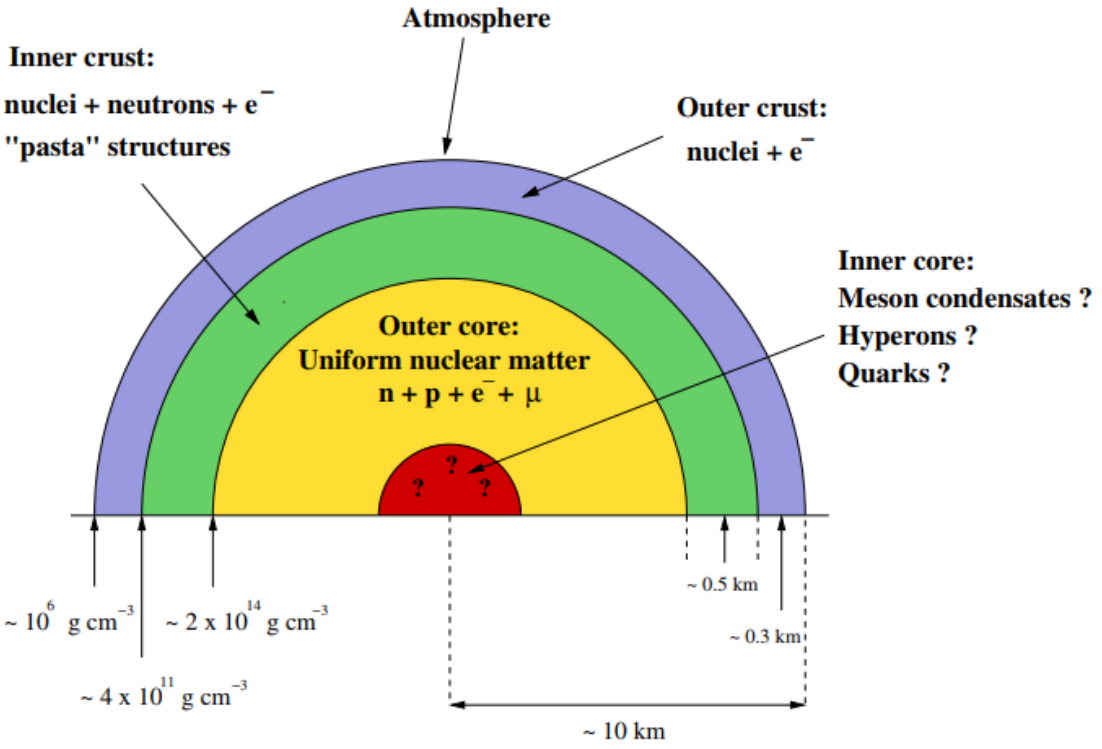

FIGURE 1.2: Structure of Neutron Stars.
Picture Courtesy: Isaac Vidana, "A short walk through the physics of neutron stars"
The European Physical Journal Plus, Vol. 133, 445, 2018

superfluid neutrons and relativistic gas of electrons. At the high density interior, the chemical potential of nucleons and leptons increase rapidly. Consequently, depending upon the stellar mass and the relative stiffness of matter, it may contain several novel phases with large strangeness fraction such as hyperon matter, Bose-Einstein condensates of strange mesons and deconfined quark matter.

1.4.1 High dense core matter

The density of compact star matter varies from normal nuclear matter density at the surface to few times of that at the core. As the density increases towards the core, an equilibrium mixture of neutrons, protons and electrons is expected to exist. The reactions which lead to the β-equilibrium in the system are,

$$n \rightarrow p + e^{-} + \bar{\nu}_e,$$

$$p + e^{-} \rightarrow n + \nu_e.$$

Neutrinos escape freely from the star. Therefore, the condition of chemical equilibrium is,

$$\mu_n = \mu_e + \mu_p. \tag{1.3}$$

The neutrons are more abundant than protons, experimental value of a positive symmetry energy ($\sim$ 30 MeV) for normal nuclear matter add support to this [42].

Hyperons

NS matter core is mainly composed of neutrons and a small mixture of protons and electrons at normal nuclear matter density. The particle population is arranged in such a manner that they attain minimum energy configuration and maintain electric charge neutrality along with chemical equilibrium. At the high density core, the Fermi energy of nucleons become sufficiently large; according to Pauli principle, the formation of hyperons becomes energetically favorable. The total energy and also the pressure of the system are lowered by sharing baryon number among several baryon species. As the nucleon chemical potential hyperons outweighs their in-medium mass in the high dense core, they are populated [43]. Hyperons are generated by strong reactions in the star interior. For example, Λ hyperons appear in the system through,

$$N + N \longrightarrow N + \Lambda + K. \tag{1.4}$$

The associated kaon is free to decay unless it is driven by some phase transition to condensed phases. Some of the decays are,

$$\begin{aligned} K^0 &\longrightarrow 2\gamma \\ K^- &\longrightarrow \mu^- + \bar{\nu} \\ \mu^- + K^+ \longrightarrow \mu^- + \mu^+ + \nu &\longrightarrow 2\gamma + \nu. \end{aligned} \tag{1.5}$$

As the temperature falls with neutrino loss, strong reactions like Eq. 1.4 are no longer possible because of the energy required to create the kaon. Nevertheless the growth of strangeness continues through direct weak flavor changing reactions such as,

$$n + N + \mu^- \longrightarrow N + \Sigma^- + 2\gamma + \nu. \tag{1.6}$$

The neutrinos and photons leak out of the star lowering its energy. Consequently, Λ hyperons become Pauli-blocked and a net strangeness evolves. The in-medium mass of hyperons and the meson-hyperon coupling constants are determined from experimental inputs such as the nature of the nuclear-hyperon interaction. Analysis of hypernuclei events predict an attractive potential for Λ and Ξ whereas a repulsive potential for Σ in symmetric nuclear matter.

Bose-Einstein condensates of antikaons

The original problem of antikaon condensation dates back to 1986-87 when Kaplan and Nelson first demonstrated within a chiral $SU(3)_L \times SU(3)_R$ model that K^- mesons may undergo Bose-Einstein condensation in dense matter formed in heavy ion collisions as well as in NSs [13]. The isospin doublet for kaons is $K \equiv (K^+, K^0)$ and that for antikaons $\bar{K} \equiv (K^-, \bar{K}^0)$. The net effect of K^- condensates in NS matter is to maintain charge neutrality replacing electrons and to soften the EoS resulting in the reduction of maximum mass of the NS [44, 45]. The s-wave condensation sets in when its effective in-medium mass equals to electron chemical potential. This occurs through,

$$\begin{aligned} n &\rightleftharpoons p + K^-, & n &\rightleftharpoons p + \pi^- \\ e^- &\rightleftharpoons K^- + \nu_e, & e^- &\rightleftharpoons \pi^- + \nu_e \end{aligned} \tag{1.7}$$

The threshold condition is met only if the interaction of mesons in nuclear medium is attractive, which reduces its effective mass. The fact that antikaons experience an attractive potential and kaons have a repulsive interaction in nuclear matter, can be inferred from various experimental data [44, 46, 47]. The threhold of antikaon condensation depends sensitively on the optical potential, whose value in nuclear medium is not known exactly. Various groups studied K^- condensation in the core of NSs using a chiral model [48] and in the traditional meson-exchange picture [44, 45, 46, 49]. It was noted in all these calculations that the typical threshold density of K^- condensation in nucleons-only NS matter was about 3-4 times normal nuclear matter density [43].

1.4.2 The crust

NS crust is divided into two parts - outer and inner crusts. The outer crust spans over the density range from $\sim 10^4$ g/cm^3 to 10^{11} g/cm^3 and is composed of nuclei and electrons. The outer crust was extensively studied by Baym, Pethick and Sutherland (BPS) [50]. In this model, nuclei are arranged in a lattice to minimize the Gibbs free energy. The density (4×10^{11} g/cm^3), at which neutrons drip out of the nuclei mark the end of outer crust. Above this density, a sea of superfluid neutrons may accompany the nuclei and becomes more abundant at higher densities. The inner crust extends from the neutron drip density up to the density at which the matter becomes uniform. In this density regime, the system displays rich and complex structures which result from the competition between nuclear and coulomb interactions.

The solid crust of a NS with a mass $M > 1M_{solar}$ though contains only about 1% of star's total mass, it is believed to play an important role in many NS phenomena, e.g. pulsar glitches, X-ray bursts, gamma-ray flares of magnetars, cooling of NS etc [51]. Few unified EoSs are available where core and crust are described using the same nuclear model. However, Fortin et. al has

shown that the use of non-unified EoS with a simplified matching between the crust and the core can introduce a lots of uncertainties in the radius determination [52].

1.5 Universality Relations

The internal structure of a compact star depends on its EoS and can be inferred by many astrophysical observations. We have discussed the observational scenario of the NS in details in section 1.2. Though mass measurement has been done with high accuracy, direct measurements of radii do not exist. Simultaneous M-R measurement can be done with accuracy $\sim 10\%$ by X-ray bursters and LMXB observations. Double NS pulsar observation may allow to measure I ($I \propto MR^2$) with the same accuracy. GW observation can infer the tidal love number, which relates I and Q, from binary NS inspirals with second generation ground based detectors like Advanced LIGO, Advanced VIRGO [23, 24]. Though these observations allow us to study the properties of compact stars with good accuracy but still none of these observations are accurate enough to choose proper EoS among many proposed.

In recent years, there has also been an alternative approach to study the structure of the NS, namely the study of universal relations among several quantities that characterizes a compact object. These quantities explicitly depend on the internal structure of the star and the relations among themselves are supposed to be independent of the EoS of the star. Therefore if one of them is measured, the other can be estimated from an analytical expression without taking into consideration the internal structure of the star. For example, radius of a NS can be determined if we know its M and I. But, many of these universality relations are approximate as they exist only in some particular regime such as slow rotation approximation and not very strong magnetic field.

It has been shown that at very high rotational frequencies, the universality between I and Q breaks down as both the deviations due to EoS and spin frequency are comparable at high spin frequency [53]. It has also been shown that a comparatively slowly rotating star ($\mathcal{P} \gtrsim 10s$) and strong magnetic fields ($B \gtrsim 10^{12}$ G), the universality between I and Q breaks down [54]. The slowly rotating stars are found to abide by universal relations as reported in Refs. [55, 56]. Many authors tried to highlight a relation between normalized I (I/MR^2) and stellar compactness ($\mathcal{C} := M/R$) [35, 53, 57, 58, 59, 60]. Breu and Rezzolla [59] studied such universal relations in great detail. Apart from the normalized moment of inertia (I/MR^2), they have used another normalization (I/M^3) and showed that universality relation holds more tightly than the previous case. It has been discovered that such relations exist among I, the Love number associated with the tidal deformation (λ) and spin induced Q [55, 56]. The relations among I, Q and λ are termed as I-love-Q relations. Physically I quantifies how fast a fixed angular momentum star rotates, while Q reflects how much a spherically symmetric star is deformed. The tidal

deformability quantifies how easily a star can be deformed [28]. Two possible reasons can explain the weak dependence of universal relations on EoS. One is that these relations preferably depend on the internal structure of the star far from the the core where all realistic EoSs approach each other. The second reason can be inferred on the aspect that the I-love-Q trio advances that of a BH as the $\mathcal{C}$ of NS increases. These relations are independent of internal structure of BH due to the no-hair theorem [56].

1.6 Objective of my Work

In this study, we investigate the effect of appearance of exotic constituents on the universal relations associated with different physical quantities in cold NSs and isentronic lepton rich PNSs. We consider G = c = k_B = 1 throughout our work, G, c and k_B being the universal gravitational constant, speed of light and Boltzmann constant respectively.

1.6.1 Critical mass, moment of inertia and universal relations of rapidly rotating neutron stars with exotic matter

We calculate I of NSs with different exotic constituents such as hyperons and antikaon condensates and study its variation with mass and spin frequency. The sets of EoSs, generated within the framework of RMF model with DD2 couplings are adopted for this purpose. We follow the quasi-stationary evolution of rotating stars along the constant rest mass sequences, that varies considerably with different constituents in the EoS. We also explore the universal relations associated with some of the normalized properties, such as critical mass and I for specific EoS or as a matter of fact constituents of the dense matter. Deviations in the universal relations for I are observed at higher $\mathcal{C}$. We study these relations for cold NS. The earlier authors in their analysis considered a large set of nucleonic EoSs with different stiffness. They satisfy the two solar mass limit, but many of them use non-relativistic interactions, and some of the relativistic EoSs also use the parameter sets that are not favorable in view of the symmetry energy nuclear experimental data. It was not known if the inclusion of exotic components or a phase transition inside the NS core would effect the universality relations. This is one of the main goals of the present work. We are also motivated to study the effect of higher rotational frequencies on the universality relation between normalized I and stellar compactness. This study presents important results concerning the properties of NSs, that could be observationally verified in the near future using SKA telescope.

1.6.2 Properties of Massive Rotating Protoneutron Stars with Hyperons: Structure and Universality

Next, we study the properties and structure of a massive and rapidly rotating PNS with hyperon content. We follow several stages of quasi-stationary evolution in an approximate way at four discrete steps. We use the RMF model with DD2 parameter set and construct the EoSs for these four stages starting from neutrino-trapped, isentropic PNS to cold catalyzed β-equilibrated NS. We use these EoSs to study the initial stages of PNS evolution and calculate different quantities such as M, R, I, and Q to get different rotating configurations upto the mass-shedding limit. We study the effect of the appearance of Λ, the lightest of all hyperons, on each of the evolutionary stages of the PNS. We also check its sensitivity to the inclusion of ϕ vector meson as a mediator of $\Lambda - \Lambda$ interaction in detail. Earlier studies investigated the effect of hyperons mostly by using older EoS parametrizations which are not consistent with the recent observations or the latest experimental data. We address the hyperon-puzzle with a more realistic microphysical input. Finally, we investigate the universal relations between I and $\mathcal{C}$ in the context of a hot and young compact object. We employ our newly-constructed finite entropy EoSs for this study.

1.6.3 Role of antikaon condensation on the universality relations of hot and rapidly rotating neutron stars

We generate profiles of several structural properties such as M, energy density (ϵ), and temperature (T) of a rotating NS comprising of nucleons and antikaon condensates using both cold as well as finite entropy EoSs. The density dependent DD2 model is used to formulate the EoSs. The parameters like M, R, I, Q and angular momentum (J) are calculated as a function of rotation frequency for a NS with fixed baryonic mass. Next, we investigate the relation of normalized I and Q with $\mathcal{C}$ and also check the universal relations between I and Q. It is found that I and Q are individually independent of EoS for cold as well as hot NS. Finally, we extend our study to calculate the tidal deformability parameter and love number and show their variation with $\mathcal{C}$.

Chapter 2

Formalism

2.1 Introduction

The NS core is the novel site in the universe where highly dense and strongly interacting matter exists. The interior of such a highly dense star is far beyond direct astronomical observations as they are too tiny (radius $\sim$ 10km) and at the same time too far (typically around a few hundreds of pc) from the earth. Hence, many theoretical models have been proposed to study the the NS interior. The Walecka model is one of such model which uses a Lorentz covariant theory of dense matter and is referred as relativistic field theoretical model [14]. It describes the interaction among nucleons in a medium via the exchange of scalar σ and vector ω mesons and has been widely used for the study of dense matter in the context of compact astrophysical objects as well as heavy ion physics [61]. The attractive and repulsive parts of the nuclear force are taken into account by σ and ω mesons respectively. Later, the Walecka model has been extended to incorporate ρ meson as well as other baryons of the baryon octet [43]. The ρ mesons take care of the isospin asymmetry of the system. All the model parameters are adjusted to reproduce the bulk properties such as saturation density, binding energy and compressibility, K of symmetric nuclear matter along with the effective mass. Though this meson-exchange model could well explain the nuclear matter and nuclei below saturation density, extrapolating the nuclear matter properties beyond saturation density leads to uncertainties. Regime above saturation density is not well understood. To represent the high dense behaviour of matter, nonlinear self interaction terms for scalar and vector fields are used in most of the RMF calculations [61]. But, they are not free from instabilities and higher order field dependence at high density [62].

An alternative approach is to include the many body correlations in a RMF model by making the meson-baryon couplings density dependent [45, 63, 64]. The variational derivatives of vertices with respect to baryon fields give rise to rearrangement terms in baryon field equations [65]. The

rearrangement term in baryon chemical potential significantly changes the pressure, consequently the EoS at higher densities [45, 63, 64].

Nuclear symmetry energy i.e the energy associated with isospin asymmetry plays a major role in EoS behaviour at high densities, by altering its stiffness. It is of great importance, along with its density dependence, in studying many crucial problems in astrophysics, such as neutronization in core collapse supernova explosion, neutrino emission from PNS, NS radii, crust thickness, cooling among various others [66]. The symmetry energy and density dependence near the saturation density n_0 are denoted by S_ν=$E_{sym}(n_0)$ and slope parameter L=$3n_0 dE_{sym}/dn|_{n=n_0,T=0}$. These parameters can be constrained by the findings of precise nuclear physics experiments (heavy ion collision analysis, dipole polarizability analysis etc.) as well as astrophysical observations. The bounds on the parameters are found to be 29 MeV $< S_\nu <$ 32.7 MeV and 40.5 MeV $< L <$ 61.9 MeV respectively [66, 67]. The RMF model with DD2 parameter set, where $S_\nu = 31.67$ MeV and $L = 55.04$ MeV, is fully consistent with the above experimental and observational constraints [64]. In fact, it is the only relativistic EoS model with linear couplings. Also DD2 EoS model agrees well with the predictions by Chiral EFT [67]. However, it should be noted that density dependent parametrization was in use [68, 65, 45] even before this symmetry energy experimental data was available. The current DD2 model differs form the previous model only by the use of experimental nuclear masses [64].

2.2 Model

The starting point in a field theoretical model of dense matter is the strong interaction Lagrangian. In the present approach, the model Lagrangian density is given as,

$$\begin{aligned}\mathcal{L}_B &= \sum_B \bar{\psi}_B \left(i\gamma_\mu \partial^\mu - m_B + g_{\sigma B}\sigma - g_{\omega B}\gamma_\mu \omega^\mu - g_{\rho B}\gamma_\mu \boldsymbol{\tau}_B \cdot \boldsymbol{\rho}^\mu\right) \psi_B \\ &\quad + \frac{1}{2}\left(\partial_\mu \sigma \partial^\mu \sigma - m_\sigma^2 \sigma^2\right) - \frac{1}{4}\omega_{\mu\nu}\omega^{\mu\nu} + \frac{1}{2}m_\omega^2 \omega_\mu \omega^\mu - \frac{1}{4}\boldsymbol{\rho}_{\mu\nu} \cdot \boldsymbol{\rho}^{\mu\nu} + \frac{1}{2}m_\rho^2 \boldsymbol{\rho}_\mu \cdot \boldsymbol{\rho}^\mu. \quad (2.1)\end{aligned}$$

Leptons are considered as non-interacting particles and the Lagrangian density for leptons is of the form,

$$\mathcal{L}_l = \sum_l \bar{\psi}_l \left(i\gamma_\mu \partial^\mu - m_l\right) \psi_l \ . \quad (2.2)$$

Here, ψ_l is lepton spinor and ψ_B denotes the baryon octets. The baryons interact via the exchange of scalar σ, vector ω, and ρ mesons, $\boldsymbol{\tau_B}$ is the isospin operator. The field strength tensors for the vector mesons are given by $\omega^{\mu\nu} = \partial^\mu \omega^\nu - \partial^\nu \omega^\mu$ and $\boldsymbol{\rho}^{\mu\nu} = \partial^\mu \boldsymbol{\rho}^\nu - \partial^\nu \boldsymbol{\rho}^\mu$. The coupling strength

of the mesons with baryons is specified by $g_{\alpha B}(\hat{n})$ where $\alpha = \sigma,\ \omega$ and ρ. They are density-dependent. The density operator $\hat{n}$ is given by, $\hat{n}$=$\sqrt{\hat{j}_\mu \hat{j}^\mu}$, where $\hat{j}_\mu = \bar{\psi}\gamma_\mu\psi$. The meson-baryon couplings also become function of total baryon density n i.e. $< g_{\alpha B}(\hat{n}) >= g_{\alpha B}(< \hat{n} >) = g_{\alpha B}(n)$ [45, 64].

The above model has been extended to accommodate the whole baryon octet. The hyperons-nucleons interaction is considered through meson exchange in similar fashion as the nucleon-nucleon interaction. However, an additional vector meson ϕ is included here. It has role only for the hyperon-hyperon interaction. [62, 69]. The Lagrangian density for this interaction is,

$$\mathcal{L}_{YY} = \sum_B \bar{\psi}_B(g_{\phi B}\gamma_\mu\phi^\mu)\psi_B - \frac{1}{4}\phi_{\mu\nu}\phi^{\mu\nu} + \frac{1}{2}m_\phi^2\phi_\mu\phi^\mu\ . \tag{2.3}$$

The equations of motion for mesons, baryon fields and antikaon condensations are derived from total Lagrangian density using Euler-Lagrange equation,

$$\partial^\mu\left[\frac{\partial\mathcal{L}}{\partial(\partial^\mu\phi)}\right] - \frac{\partial\mathcal{L}}{\partial\phi} = 0. \tag{2.4}$$

where ϕ denotes any of the fields. The meson field equations for baryons are given by,

$$\begin{aligned}
\partial^\mu(\partial_\mu\sigma) + m_\sigma^2\sigma &= \sum_B g_{\sigma B}\bar{\psi}_B\psi_B \\
\partial^\nu\omega_{\mu\nu} + m_\omega^2\omega_\mu &= \sum_B g_{\omega B}\bar{\psi}_B\gamma_\mu\psi_B \\
\partial^\nu\phi_{\mu\nu} + m_\phi^2\phi_\mu &= \sum_B g_{\phi B}\bar{\psi}_B\gamma_\mu\psi_B \\
\partial^\nu\rho_{\alpha\mu\nu} + m_\rho^2\rho_{\mu\alpha} &= \frac{1}{2}\sum_B g_{\rho B}\bar{\psi}_B\gamma_\mu\tau_{\alpha B}\psi_B
\end{aligned} \tag{2.5}$$

The exact solutions of the mesons equations are complicated because of the presence of the source terms on the right hand side of equations 2.5. Again, in the strong interaction, coupling constants $g_{\omega B}$, $g_{\sigma B}$ and $g_{\rho B}$ are too large to use the perturbative approach. So, the mean field approximation is used to solve the meson equations of motion self-consistently. In this approximation, the meson fields are replaced by their classical values. $\sigma \rightarrow < \sigma >$, $\omega_\mu \rightarrow < \omega_\mu >$ and $\rho_\mu \rightarrow < \rho_\mu >$. For a static system, all space time derivatives of the fields vanish. Also, in the rest frame of the matter the space components of ω_μ and ρ_μ vanish. The third component of ρ meson couples to nucleons because the expectation values of the sources for charged ρ mesons vanish in the ground state of the system. The mean meson fields are denoted by σ, ω_0 and ρ_{03}.

Charge neutrality and baryon number conservation conditions are imposed to solve meson field equations self-consistently. The Dirac equation for baryons under mean field approximation reduces to,

$$[\gamma_\mu \left(i\partial^\mu - \Sigma_B\right) - m_B^*]\psi_B = 0. \tag{2.6}$$

Here $m_B^* = m_B - g_{\sigma B}\sigma$ is the effective baryon mass, with m_B as the vacuum rest mass of baryon B whereas $\Sigma_B = \Sigma_B^{(0)} + \Sigma_B^{(r)}$ is the vector self-energy. The first term in the vector self-energy consists of the usual non-vanishing components of the vector mesons i.e. $\Sigma_B^{(0)} = g_{\omega B}\omega_0 + g_{\rho B}\tau_{3B}\rho_{03} + g_{\phi B}\phi_0$ and the second term is rearrangement term. It arises due to density-dependence of the meson-baryon coupling constants [45] and is given by,

$$\Sigma_B^{(r)} = \sum_B [-g'_{\sigma B}\sigma n_B^s + g'_{\omega B}\omega_0 n_B + g'_{\rho B}\tau_{3B}\rho_{03} n_B + g'_{\phi B}\phi_0 n_B] \ , \tag{2.7}$$

where $g'_{\alpha B} = \frac{\partial g_{\alpha B}}{\partial \rho_B}$, $\alpha = \sigma,\ \omega,\ \rho,\ \phi$ and τ_{3B} is the isospin projection of B=n, p, Y. The baryons and leptons are in chemical equilibrium in NSs interior with the equilibrium condition $\mu_i = b_i\mu_n - q_i\mu_e$, where b_i is the baryon number and q_i, the charge of ith baryon and μ_n is the chemical potential of neutrons and μ_e is that of electrons. This condition determines the threshold of a particular hyperon. When the chemical potential of the neutron and electron become sufficiently large at high density and eventually the threshold of hyperons are reached, they are populated. The chemical potential for the baryon B is $\mu_B = \sqrt{k_B^2 + m_B^{*2}} + g_{\omega B}\omega_0 + g_{\rho B}\tau_{3B}\rho_{03} + g_{\phi B}\phi_0 + \Sigma_B^{(r)}$. The term $g_{\phi B}\phi_0$ in μ_B is applicable for hyperons only.

We choose the antikaon-baryon interaction on the same footing as the baryon-baryon interaction. The Lagrangian density for antikaons in the minimal coupling scheme is given by [44, 46, 47, 70],

$$\mathcal{L}_K = D_\mu^* \bar{K} D^\mu K - m_K^{*2}\bar{K}K \ . \tag{2.8}$$

Here, the covariant derivative is $D_\mu = \partial_\mu + ig_{\omega K}\omega_\mu + ig_{\rho K}\boldsymbol{\tau}_K \cdot \boldsymbol{\rho}_\mu + ig_{\phi K}\phi_\mu$ and $m_K^* = m_K - g_{\sigma K}\sigma$ is the effective mass of antikaons where m_K is the bare kaon mass. The isospin doublet for kaons is, $K \equiv (K^+, K^0)$ and that for antikaons is $\bar{K} \equiv (K^-, \bar{K}^0)$.

The meson field equations in presence of antikaon condensates in mean field approximation have an additional contribution from the antikaon condensates and are given by,

$$m_\sigma^2\sigma = \sum_B g_{\sigma B} n_B^s + g_{\sigma K} \sum_{\bar{K}} n_{\bar{K}} , \tag{2.9}$$

$$m_\omega^2\omega_0 = \sum_B g_{\omega B} n_B - g_{\omega K} \sum_{\bar{K}} n_{\bar{K}} , \tag{2.10}$$

$$m_\rho^2\rho_{03} = \sum_B g_{\rho B}\tau_{3B} n_B + g_{\rho K} \sum_{\bar{K}} \tau_{3\bar{K}} n_{\bar{K}} , \tag{2.11}$$

$$m_\phi^2\phi_0 = \sum_B g_{\phi B} n_B - g_{\phi K} \sum_{\bar{K}} n_{\bar{K}} . \tag{2.12}$$

Here, ${n_B}^s$ and n_B are the scalar number density and number density of baryons respectively. Similarly, $n_{\bar{K}}$ is the number density for kaons. The in-medium energy of the $K^\pm$ mesons is given by,

$$\omega_{K^\pm} = \sqrt{(k^2 + m_K^*)} \pm (g_{\omega K}\omega_0 + g_{\rho K}\rho_{03}). \tag{2.13}$$

Here, the effective mass of the antikaons is $m_K^* = m_K - g_{\sigma K}\sigma$ with m_K is the bare kaon mass. The momentum dependence vanishes in $\omega_{K^\pm}$ for s-wave ($\mathbf{k} = 0$) condensation. $\mu_{K^-} = \omega_{K^-}$ is the threshold condition for s-wave K^- condensate. The chemical potential of K^- is determined through the chemical equilibrium in the reaction $n \leftrightarrow p + K^-$ as,

$$\mu_{K^-} = \mu_n - \mu_p = \mu_e. \tag{2.14}$$

The ω_{K^+} won't drop to satisfy the threshold condition of $\omega_{K^+} = \mu_e$ but ω_{K^-} decreases from its vacuum value m_K with increasing density as the meson fields grow. Thus only K^- condensates appear in the system [48].

2.2.1 EoS of PNS and cold NS core

When a massive star ($M \gtrsim 8M_{solar}$) reaches the end of its life, its core collapses. This leads to supernova explosion leaving its center as a dense compact remnant, called a PNS. Initially, the PNS is very hot, lepton-rich and rapidly rotating. It deleptonizes releasing the trapped neutrinos. In the process, the neutrinos heat up the PNS while decreasing the net lepton fraction. After that, the PNS enters a steady cooling phase and becomes a cold, catalyzed NS [48, 71, 72]. Here we describe how the EoS for the dense core is calculated solving the meson field equations described in the previous section. First, we will discuss the zero temperature EoS, appropriate to a cold NS. Next we move on to isentropic, finite temperature EoS, which best describes the hot and neutrino-trapped PNS.

Zero temperature EoS

The temperature of the stable NS is low ($\sim$ a few MeV), compared to the momenta ($\sim$ a few hundreds of MeV) of the constituents Fermions. Hence, the dense interior of the cold NS can be suitably represented by zero-temperature EoS. The number density and scalar number density for the baryons are given by,

$$n_B = <\bar{\psi}_B\gamma_0\psi_B>= \frac{k_{F_B}^3}{3\pi^2} , \tag{2.15}$$

$$\begin{aligned} n_B^s &= <\bar{\psi}_B\psi_B>= \frac{2J_B+1}{2\pi^2}\int_0^{k_{F_B}} \frac{m_B^*}{(k^2+m_B^{*2})^{1/2}}k^2\ dk \\ &= \frac{m_B^*}{2\pi^2}\left[k_{F_B}\sqrt{{k_{F_B}}^2+m_B^{*2}} - m_B^{*2}ln\frac{k_{F_B}+\sqrt{{k_{F_B}}^2+m_B^{*2}}}{m_B^*}\right] . \end{aligned} \tag{2.16}$$

The energy density due to baryons can be expressed as,

$$\begin{aligned} \varepsilon_B &= \frac{1}{2}m_\sigma^2\sigma^2+\frac{1}{2}m_\omega^2\omega_0^2+\frac{1}{2}m_\rho^2\rho_{03}^2+\frac{1}{2}m_\phi^2\phi_0^2+ \\ &\sum_B \frac{2J_B+1}{2\pi^2}\int_0^{k_{F_B}}(k^2+m_B^{*2})^{1/2}k^2\ dk+\sum_l\frac{1}{\pi^2}\int_0^{K_{F_l}}(k^2+m_l^2)^{1/2}k^2\ dk. \end{aligned} \tag{2.17}$$

The rearrangement term won't contribute to energy density but appears in pressure through baryon chemical potentials. It accounts for the energy-momentum conservation and thermodynamic consistency of the system [45]. The expression for pressure (P_B) is given as,

$$\begin{aligned} P_B &= -\frac{1}{2}m_\sigma^2\sigma^2+\frac{1}{2}m_\omega^2\omega_0^2+\frac{1}{2}m_\phi^2\phi_0^2+\frac{1}{2}m_\rho^2\rho_{03}^2+\Sigma_B^{(r)}\sum_B n_B \\ &+\frac{1}{3}\sum_B\frac{2J_B+1}{2\pi^2}\int_0^{k_{F_B}}\frac{k^4\ dk}{(k^2+m_B^{*2})^{1/2}}+\frac{1}{3}\sum_l\frac{1}{\pi^2}\int_0^{k_{F_l}}\frac{k^4\ dk}{(k^2+m_l^2)^{1/2}} . \end{aligned} \tag{2.18}$$

The Gibbs-Duhem relation gives the relation between pressure (P_B) and energy density (ϵ_B),

$$P_B = \sum_i \mu_i n_i - \varepsilon_B . \tag{2.19}$$

The scalar and vector densities of antikaon condensates at T=0 for s-wave ($\mathbf{k}$=0) are same and given by, [70]

$$n_{K^-,\,\bar{K}^0} = 2\left(\omega_{K^-,\bar{K}^0}+g_{\omega K}\omega_0+g_{\phi K}\phi_0\pm g_{\rho K}\rho_{03}\right)\bar{K}K . \tag{2.20}$$

The energy density of antikaons is given by $\epsilon_{\bar{K}}= m_K^*\left(n_{K^-}+n_{\bar{K}^0}\right)$. However, antikaon condensates do not contribute to the pressure directly. The pressure arises due to baryons and leptons only. The total energy density of the NS interior is $\epsilon=\epsilon_B+\epsilon_{\bar{K}}+\epsilon_l$ which has contribution from the baryons, leptons, and the antikaons.

Finite entropy EoS

As we proceed to construct isentropic EoS for PNS, the expressions for number density and scalar number density of baryons are modified to,

$$n_B = 2\int \frac{d^3k}{(2\pi)^3}\left(\frac{1}{e^{\beta(E^*-\nu_B)}+1} - \frac{1}{e^{\beta(E^*+\nu_B)}+1}\right). \tag{2.21}$$

$$n_B^S = 2\int \frac{d^3k}{(2\pi)^3}\frac{m_B^*}{E^*}\left(\frac{1}{e^{\beta(E^*-\nu_B)}+1} + \frac{1}{e^{\beta(E^*+\nu_B)}+1}\right) . \tag{2.22}$$

where, $\beta = 1/T$ and $E^* = \sqrt{(k^2 + m_B^{*2})}$. The explicit form of the energy density is

$$\begin{aligned}\epsilon_B &= \frac{1}{2}m_\sigma^2\sigma^2 + \frac{1}{2}m_\omega^2\omega_0^2 + \frac{1}{2}m_\rho^2\rho_{03}^2 + \frac{1}{2}m_\phi^2\phi_0^2 \\ &\quad +2\sum_{B=n,p,Y}\int \frac{d^3k}{(2\pi)^3}E^*\left(\frac{1}{e^{\beta(E^*-\nu_B)}+1} + \frac{1}{e^{\beta(E^*+\nu_B)}+1}\right) .\end{aligned} \tag{2.23}$$

The pressure due to baryons is calculated as [43],

$$\begin{aligned}P_B &= -\frac{1}{2}m_\sigma^2\sigma^2 + \frac{1}{2}m_\omega^2\omega_0^2 + \frac{1}{2}m_\rho^2\rho_{03}^2 + \frac{1}{2}m_\phi^2\phi_0^2 + \Sigma_B^{(r)}\sum_B n_B \\ &\quad +2T\sum_{B=n,p,Y}\int \frac{d^3k}{(2\pi)^3}[ln(1+e^{-\beta(E^*-\nu_B)}) + ln(1+e^{-\beta(E^*+\nu_B)})].\end{aligned} \tag{2.24}$$

We adopt the finite entropy treatment of antikaon condensates by Pons. et. al [73]. The net antikaon number density is given by $n_K = n_K^C + n_K^T$, where n_K^C is the K^- condensate density and n_K^T is the thermal density [74]. The expressions for these densities are

$$n_K^C = 2\left(\omega_{K^-} + g_{\omega K}\omega_0 + \frac{1}{2}g_{\rho K}\rho_{03}\right)\bar{K}K = 2m_K^*\bar{K}K . \tag{2.25}$$

$$n_K^T = \int \frac{d^3k}{(2\pi)^3}\left(\frac{1}{e^{\beta(\omega_{K^-}-\mu)}-1} - \frac{1}{e^{\beta(\omega_{K^+}+\mu)}-1}\right) . \tag{2.26}$$

The condensates do not contribute to pressure, but implicitly change the rearrangement term of Eq. 2.7 via the values of meson fields. The energy density of K^- condensates is given by,

$$\begin{aligned}\epsilon_K &= m_K^* n_K^C + \left(g_{\omega K}\omega_0 + \frac{1}{2}g_{\rho K}\rho_{03}\right)n_K^T \\ &\quad + \int \frac{d^3k}{(2\pi)^3}\left(\frac{\omega_{K^-}}{e^{\beta(\omega_{K^-}-\mu_{K^-})}-1} + \frac{\omega_{K^+}}{e^{\beta(\omega_{K^+}+\mu_{K^+})}-1}\right) .\end{aligned} \tag{2.27}$$

The first term of energy density is the contribution due to K^- condensate and second, third terms are the thermal contributions.

In addition to nucleons and K^- mesons, we also consider non-interacting leptons in the system. We calculate number densities, energy densities and pressures of leptons in similar way as baryons. When the electron chemical potential μ_e becomes equal to the muon mass in a NS, the electrons are converted to muons by the reaction, $e^- \rightarrow \mu^- + \bar{\nu}_\mu + \nu_e$. Thus, the appearance of muons is determined by the condition $\mu_e = \mu_\mu$. Usually muons are ignored in hot dense matter because of their high rest mass ($m_\mu \sim 105.66 MeV/c^2$), which suppresses their appearance. However, at high temperatures the electron chemical potential exceeds m_μ leading to a significant number of muons. But in our study, the energetically favoured antikaon condensates replace the leptons as soon as they are formed. As the formation of μ^+s is strongly suppressed we ignored them. Thus, the total energy density in the presence of K^- condensates is, $\epsilon = \epsilon_B + \epsilon_K + \epsilon_l$.

We construct the hot EoS at constant entropy per baryon (s_B). The entropy density ($\mathcal{S}_B$) of baryons is related to energy density and pressure through Gibbs-Duhem relation as $\mathcal{S}_B = \beta\left(\epsilon_B + P_B - \sum_i \mu_i n_i\right)$, where, $i = n, p, Y$. The entropy density of antikaons is, $\mathcal{S}_K = \beta(\epsilon_K + P_K - \mu_{K^-} n_K)$, where, $n_K = n_K^C + n_K^T$. The entropy per baryon is given by $s_B = \mathcal{S}/n_B$, where n_B is the total baryon density and S is the total entropy density, which has contribution from the baryons, antikaons and leptons.

2.2.2 Some important features of the formalism

Matching different parts of the EoS

In this section, we briefly discuss some of the important features of the formalism, we follow. Our NS and PNS EoSs are constructed in a unified way by smoothly matching the high density and low density parts following Banik et al. [49]. For the low-density part, nuclear statistical model of Hempel and Schaffner-Bielich [75] is used to treat the heavy and light nuclei as well as the interacting nucleons, including the excluded volume effects and other in-medium effects. It consists of non-uniform matter of light and heavy nuclei along with unbound nucleons at low temperatures and densities that are below nuclear saturation. Interaction among the unbound nucleons are described by considering the same Lagrangian density as in Eq. 2.1 and using the density dependent formalism [64, 75]. As the hyperons and K^- condensates appear only at high densities and at relatively high temperatures, the nuclei and exotic matter are never found to coexist. Therefore, we simply use the non-uniform part of the nucleons-only HS(DD2) EoS [49, 75] following the standard prescription of minimisation of free energy as is given in Banik et. al. [49]. Although the above procedure allows for a smooth transition between the different parts of EoS at around nuclear saturation density, it is of course not completely consistent as was emphasised in Marques et. al. [76]. Recently, Fortin et. al. [52] have shown that the

TABLE 2.1: Parameters of the meson-nucleon couplings in DD2 model

meson α	$g_{\alpha B}$	a_α	b_α	c_α	d_α
ω	13.342362	1.369718	0.496475	0.817753	0.638452
σ	10.686681	1.357630	0.634442	1.005358	0.575810
ρ	3.626940	0.518903			

core-crust matching does not have any effect on the maximum mass allowed for the star, but the uncertainty in radius calculations can be $\sim 4\%$ depending on the way core-crust matching is done.

The constraints

For NS matter, other than charge neutrality and baryon number conservation, we impose an additional condition of β equilibrium on the chemical potentials, $\mu_n - \mu_p = \mu_e$. On the other hand, the chemical equilibrium condition for the lepton-trapped PNS is $\mu_n - \mu_p = \mu_e - \mu_\nu$. Also, just after its birth, the PNS initially has trapped neutrinos and the lepton fraction is fixed at $Y_L = 0.4$.

2.2.3 Model parameters

The nucleon-meson density-dependent couplings are determined following the prescription of Typel et. al [63, 64]. The functional dependence of the couplings on density was first introduced in [77] and is described as,

$$g_{\alpha B}(n_B) = g_{\alpha B}(n_0) f_\alpha(x). \tag{2.28}$$

with $x = n_B/n_0$, n_B being the baryon density, and $f_\alpha(x)$ is

$$f_\alpha(x) = a_\alpha \frac{1 + b_\alpha(x + d_\alpha)^2}{1 + c_\alpha(x + d_\alpha)^2}. \tag{2.29}$$

Here, $\alpha = \omega,\ \sigma$. the number of parameters are reduced by constraining the functions as $f_\sigma(1) = f_\omega(1) = 1$, $f'_\sigma(0) = f'_\omega(0) = 0$ and $f_\sigma(1) = f_\omega(1) = 1$, $f''_\sigma(1) = f''_\omega(1)$ [63]. The $\boldsymbol{\rho}_\mu$ coupling decreases at higher densities, therefore, an exponential density-dependence is assumed for the isovector meson ρ i.e. $f_\alpha(x) = \exp[-a_\alpha(x-1)]$ [77]. These functional dependence is now widely used [78, 79, 80]. The saturation density, the mass of σ meson, the couplings $g_{\alpha B}(n_0)$ and the coefficients a_α, b_α, c_α, d_α are found by fitting the finite nuclei properties [63, 64] and are tabulated in Table 2.1 [81]. The fit gives the saturation density $n_0 = 0.149065 fm^{-3}$, binding energy per nucleon as -16.02 MeV and incompressibility $K = 242.7$ MeV. The masses of neutron, proton, ω and ρ mesons are 939.56536, 938.27203, 783, 763 MeV respectively [64].

Next, we determine the hyperon-meson couplings. In the absence of density-dependent Dirac-Bruekner calculation for hyperon couplings, we use scaling factors [62, 81] and nucleon-meson couplings of Table 2.1 to determine the hyperon-meson couplings. The vector coupling constants for hyperons are determined from the SU(6) symmetry [62] as,

$$\begin{aligned} \frac{1}{2}g_{\omega\Sigma} = g_{\omega\Xi} = \frac{1}{3}g_{\omega N}, \\ \frac{1}{2}g_{\rho\Sigma} = g_{\rho\Xi} = g_{\rho N}; \quad g_{\rho\Lambda} = 0, \\ 2g_{\phi\Lambda} = g_{\phi\Xi} = -\frac{2\sqrt{2}}{3}g_{\omega N} \ . \end{aligned} \tag{2.30}$$

The scalar meson (σ) coupling to hyperons is obtained from the potential depth of a hyperon (Y) in the saturated nuclear matter,

$$U_Y^N(n_0) = -g_{\sigma Y}\sigma + g_{\omega Y}\omega_0 + \Sigma_N^{(r)}, \tag{2.31}$$

where $\Sigma_N^{(r)}$ involves only the contributions of nucleons. The analysis of energy levels in Λ-hypernuclei suggests a potential well depth of Λ in symmetric matter $U_\Lambda^N(n_0) = -30$ MeV [82, 83]. On the other hand, recent analysis of a few Ξ-hypernuclei events predict a Ξ well depth of $U_\Xi^N(n_0) = -18$ MeV [84, 85]. The potential Σ hyperons feel in nuclear matter is quite uncertain. The analyses of (π^-, K^+) reactions off nuclei suggest a moderate repulsive potential, whereas σ^--atomic data indicates an attractive potential at the surface to a repulsive one inside the nucleus. Hence Σ hyperons are not considered in our studies. The experimental studies of HICs and the theoretical studies derived from chiral effective forces [86] are expected to narrow down these uncertainties of hyperon-nucleon interactions in dense matter. However, the particular choice of hyperon-nucleon potential does not change the maximum mass of NSs [87]. We use these values and find the scaling factor $R_{\sigma\Lambda} = 0.62008$ and $R_{\sigma\Xi} = 0.32097$. Finally, we compute the meson-antikaon couplings on the same footing as that of meson-hyperon couplings. However, we do not consider any density-dependence for antikaon-nucleon couplings. According to the quark model and isospin counting rule, the vector coupling constants are given by,

$$g_{\omega K} = \frac{1}{3}g_{\omega N}; \qquad g_{\rho K} = g_{\rho N}\ \sqrt{2} \qquad \text{and} \qquad \sqrt{2}\ g_{\phi K} = 6.04. \tag{2.32}$$

The scalar coupling constant ($g_{\sigma K}$) is obtained from the real part of the K^- optical potential at the normal nuclear matter density, [44, 45, 46, 62]

$$U_{\bar{K}}\,(n_0) = -g_{\sigma K}\sigma - g_{\omega K}\omega_0\ + \Sigma_N^{(r)}\ . \tag{2.33}$$

The study of kaon atoms clearly suggests an attractive antikaon nucleon optical potential. However, there is controversy about how deep the potential is, whether the antikaon optical potential is extremely deep, as it is preferred by the phenomenological fits to kaonic atoms

TABLE 2.2: Parameters of the scalar σ meson -antikaon couplings in DD2 model

$U_{\bar{K}}$ in MeV	-60	-80	-100	-120	-140
$g_{\sigma\bar{K}}$	-1.24609	-0.72583	-0.20557	0.31469	0.83495

data, or shallow, as it comes out from unitary chiral model calculations. Different experiments also suggest a range of values for $U_{\bar{K}}$ from -50 to -200MeV and do not come to any definite consensus [88]. The coupling constants for kaons with σ-meson, $g_{\sigma K}$ at the saturation density for different values of $U_{\bar{K}}$ for DD2 model is listed in Table 2.2.

2.3 Structural properties of NS

NSs are relativistic objects and computations of their structure should be carried out in a general-relativistic (GR) framework. A rotating star is accurately described by a stationary, axisymmetric solution to the Einstein field equation

$$G^{\alpha\beta} = 8\pi T^{\alpha\beta} \tag{2.34}$$

where $G^{\alpha\beta}$ is the Einstein tensor, describing the curvature of spacetime and $T^{\alpha\beta}$ is the stress energy tensor, describing matter/energy sources of spacetime curvature. For a perfect fluid, the stress-energy tensor is given by, $T^{\alpha\beta} = (\epsilon + P)u^{\alpha}u^{\beta} + Pg^{\alpha\beta}$, where ϵ is energy density, P is pressure, both in the fluid frame and u^{α} is the fluid 4-velocity.

2.3.1 Static structure of a spherically symmetric star

The interior Schwarzschild metric for a static star gives the following line element:

$$g_{\alpha\beta}dx^{\alpha}dx^{\beta} = -\exp^{2\nu(r)}dt^2 + \left(1 - \frac{2m(r)}{r}\right)^{-1} dr^2 + r^2d\theta^2 + r^2sin^2\theta d\phi^2. \tag{2.35}$$

m(r) is the gravitational mass inside radius r, where r is defined such that the circumference of a circle about the origin at that space location is $2\pi r$. In hydrostatic equilibrium, the structure of a spherically symmetric, static relativistic NS is determined by the Tolman-Oppenheimer-Volkoff (TOV) equations. Tolman, Oppenheimer, and Volkoff basically reformulated Einstein's equation using Eq. 2.35 and the expression for stress energy tensor, where $u^{\alpha} = (c, 0, 0, 0)$. These ordinary

differential equations are:

$$\begin{aligned} \frac{dm}{dr} &= 4\pi\epsilon r^2 \\ \frac{d\nu}{dr} &= \left(1 - \frac{2m(r)}{r}\right)^{-1} \left(\frac{m(r)}{r^2} + 4\pi r P\right) \\ \frac{dP}{dr} &= -\left(\epsilon + P\right)\frac{d\nu}{dr}. \end{aligned} \tag{2.36}$$

The NS matter can be approximated as a perfect fluid at zero temperature except immediately after its birth, whose EoS can be written as $\epsilon = \epsilon(n_B)$ and $P = P(n_B)$, where n_B is the baryon number density in the fluid frame. This is known as barotropic EoS. Given a barotropic EoS, the stellar structure can be computed by numerically integrating Eqs. 2.36 from the centre at r=0 out to the star surface at r=R. The sensible choice of boundary conditions are $P(r = R) = 0$, $P(r = 0) = P_c(\rho_c)$, $m(r = 0) = 0$, and $\nu(r = R) = \frac{1}{2}ln(1 - \frac{2M}{R})$. M is the enclosed gravitational mass given by M(r)=$4\pi \int_0^R \epsilon(r)r^2dr$.

2.3.2 Structure of the rotating relativistic star

The line element for a rotating star has four independent potentials N, A, B and ω, each a function of r and θ and is given by,

$$g_{\alpha\beta}dx^\alpha dx^\beta = -N^2dt^2 + A^2\left(dr^2 + r^2d\theta^2\right) + B^2r^2sin^2\theta(d\phi - \omega dt)^2. \tag{2.37}$$

When the star is non-rotating, the exterior geometry is that of the isotropic Schwarzschild metric (Eq. 2.35) with $\omega = 0$, $\nu \coloneqq ln(N)$. Since we are interested in rotating stars, the fluid 4-velocity can be written as,

$$\vec{u} = \Gamma(\vec{n} + \vec{U}). \tag{2.38}$$

where, $\vec{n}$ are the 4-velocity of the ZAMO (zero angular momentum observers). $\Gamma = (1 - U^2)^{-1/2}$ and $\vec{U}$ are the Lorentz factor and 3-velocity of the fluid with respect to ZAMO respectively. [89].

The equations of motion are the energy-momentum conservation law,

$$\nabla_\alpha T^{\alpha\beta} = 0 \tag{2.39}$$

and the baryon number conservation law $\nabla_\alpha(n_B u^\alpha) = 0$. Inserting the perfect fluid form of $T^{\alpha\beta}$ in Eq. 2.39, we get the relativistic Euler equation [90],

$$(\epsilon + P)u^\beta\nabla_\beta u^\alpha = q^{\alpha\beta}\nabla_\beta P. \tag{2.40}$$

where $q^{\alpha\beta}$ is the projection operator orthogonal to the fluid trajectories and given as $q^{\alpha\beta}$= $g^{\alpha\beta}$+$u^{\alpha}u^{\beta}$. For a rotating star, we consider a circular fluid motion around the rotation axis. For rigid rotation, it leads to the first integral,

$$H + \nu - ln\Gamma = const. \tag{2.41}$$

where the log-enthalpy $H \coloneqq ln(\frac{h}{M_B})$, M_B being the mean baryon mass $\simeq 1.66 \times 10^{-27}$ kg, and the enthalpy per baryon $h \coloneqq \frac{\epsilon+P}{n_B}$. The first integral of motion, Eq.2.41, can be rewritten as $H = H_c + \nu_c - \nu + ln\Gamma$, where H_c and ν_c are the values of H and ν at r=0. For a barotropic EoS of the form $\epsilon = \epsilon(H)$ and $P = P(H)$, starting with some initial value of the metric functions N, ω, A and B, and input parameter H_c, the Einstein equations are solved. The surface of the star is defined by the vanishing the pressure, where $H = H_0$ also generally vanishes. Using Eq. 2.41, H is computed in all space and a rotating stellar model is constructed numerically. As H_c remains larger than H_0, for a given value of H_c, there exists a maximum rotation velocity at the stellar equator, which physically corresponds to Keplerian limit denoted by Ω_K [89].

The equation for stationary motion is given by [91],

$$\partial_i \left(H + ln\frac{N}{\Gamma} \right) = Te^{-H}\partial_i s_B. \tag{2.42}$$

The global properties of the rotating stars i.e. total baryon number, gravitational mass, angular momentum and quadrupole moment are given respectively as [92, 93, 94],

$$n_B = \frac{\epsilon + P}{M_B} \exp(-H), \tag{2.43}$$

$$M = \frac{1}{4\pi} \int \sigma_{lnN}\ r^2 \sin^2\theta dr d\theta d\phi\ , \tag{2.44}$$

$$J = \int A^2 B^2 (E + P) U r^3 \sin^2\theta dr d\theta d\phi\ , \tag{2.45}$$

$$Q = -M_2 - \frac{4}{3}\left(b + \frac{1}{4} \right) M^3\ , \tag{2.46}$$

where,

$$M_2 = -\frac{3}{8\pi} \int \sigma_{lnN} \left(\cos^2\theta - \frac{1}{3} \right) r^4 \sin^2\theta dr d\theta d\phi\ . \tag{2.47}$$

Here, σ_{lnN} is the source term in the expression for lnN (given by the RHS of Eq. 3.19 of [95]); $E = \Gamma^2(\epsilon$ + P) - P. The quantity b is given by [94],

$$b = -\frac{8}{\pi M^2} \int Pr \sin\theta e^{\nu} dV. \tag{2.48}$$

dV being the volume element. Then, the I of the rotating star is defined as, I=J/Ω, where Ω is the stellar angular velocity.

In this thesis work, we use two open-source codes RNS [96] and LORENE [97] to compute accurate stellar models for our set of realistic EoSs. RNS needs a zero-temperature EoS consisting of four inputs - energy density (in gm/cm^3), pressure (in dynes/cm^2), enthalpy (in cm^2/s^2), and baryon number density (in cm^{-3}). The enthalpy is defined as,

$$H(P) = \int_0^P \frac{c^2 dP}{(\epsilon + P)}. \tag{2.49}$$

where c is the speed of light. The number of points should be limited to 200. The NS models RNS computes are assumed to be stationary, axisymmetric, uniformly rotating perfect fluid solutions of the Einstein field equations. LORENE, on the other hand, is primarily formulated for cold EoS, or a barotropic EoS [91]. Our EoSs for PNS are temperature dependent as we have considered isoentropic profile for the stars. This homoentropic flow makes the EoS barotropic, which enables us to use the LORENE formalism to study the PNS stages.

Chapter 3

Critical mass, moment of inertia and universal relations of rapidly rotating neutron stars with exotic matter

3.1 Introduction

After the discovery of highly relativistic binary systems such as the double pulsar system PSR J0737-3039 for which masses of both PSRs are known accurately, it was argued that a precise measurement of I of one PSR might overcome the uncertainties in the determination of R since dimensionally $I \propto MR^2$ [35]. In relativistic binary systems, higher order post Newtonian (PN) effects could be measured. Furthermore, the relativistic spin-orbit (SO) coupling may manifest in an extra advancement of periastron above the PN contributions such that the total advance of periastron is $\dot{\omega} = \dot{\omega}_{1PN} + \dot{\omega}_{2PN} + \dot{\omega}_{SO}$ [98]. The SO contribution has a small effect and could be measured when it is comparable to the 2PN contribution. The measurement of the SO effect leads to the determination of I of a PSR in the double PSR system [26, 99]. However simulations assuming 5μs timing precision for the pulsar A of PSR J0737-3039 predict that it would take another 20 years to measure I at 10% accuracy [100]. This situation would change vastly with the advent of world's largest telescope SKA, when it begins its operation and measure I of the double PSR J0737-3039A. Moreover, the spin off from the measurement of I in the SKA looks promising. The first consequence is the estimation of radius in highly relativistic binaries where mass of each NS is accurately determined. Secondly, if the back bending effect is observed, it might reveal a phase transition from nuclear matter to some exotic form of matter (hyperon or quark) in NS interior [101]. Furthermore, I measurement would shed light on the I-love-Q

relation, masses, radii, backbending and stability for rotating NSs with hyperon and quark cores [101]. Some earlier studies also reported backbending in NSs with quark core [102, 103].

Here in this chapter, we present important results concerning the properties of NSs, that could be observationally verified in the near future using SKA telescope. We calculate I of NS with different exotic constituents such as hyperons and antikaon condensates and study its variation with mass and spin frequency. We consider a β-stable NS, whose interior temperature becomes $\sim 10^9 K$ within the few years of formation. This is quite negligible compared to the Fermi energy of the constituent dense matter. Hence, the effect of finite temperature is ignored. For different compositions, we generate the EoS under the framework of RMF model with DD2 parameter set [45, 81] and study the variation of M-R profile for different EoSs. The high-dense core is surrounded by a crust made of heavy and light nuclei, also the interacting neutrons. The NS is modeled by a stationary, axisymmetric, perfect fluid space-time. The presence of solid crust contributes to negligible departure (of the order of 10^{-5}) from perfect fluid equilibrium. Also with time, the outer crust becomes superfluid and the nucleons form an array of vortices due to rotation. The characteristic length over which the gravitational field of the rotating star varies is much larger than distance between the vortices. So the relativistic star is modeled as a uniformly rotating, zero-temperature perfect fluid [94]. We study the maximum mass sustainable for rotating configuration, expressed in terms of dimensionless critical mass and normalized angular momenta. Next, we follow the variation of I with gravitational mass and observe how rotation affects I for different constituents of dense matter relevant to the NS core. If the I is measured with 10% uncertainty, this would constrain the radius of a $1.4M_{\odot}$ star with $6\% - 7\%$ uncertainty [35]. But again, there will be a family of EoS models in I-M curve lying in that range. Thus, it is crucial to examine the dependence of I on EoS.

Finally, we investigate if there exists a universal relation between I and $\mathcal{C}$. We use two types of normalized I relations prescribed by Ref [35, 59] for EoS with nucleon, hyperon and antikaon condensates degrees of freedom for rapidly rotating compact stars. Many authors tried to highlight a relation between normalized I (I/MR^2) and $\mathcal{C}$ [35, 53, 57, 58, 59, 60]. Also, having a universal relation will allow us to determine the radius with a very high accuracy once we have simultaneous measurements of I and mass of the same star. Breu and Rezzolla [59] studied such universal relations in great detail. They have also used another normalisation for I as (I/M^3) and showed that universality relation holds more tightly than the previous case. In their analysis, they have taken a large set of EoSs with different stiffness. However, the matter they considered is nucleonic. They satisfy the two solar mass limit, but many of them use non-relativistic interactions, and some of the relativistic EoSs also use the parameter sets that are not favorable in view of the symmetry energy nuclear experimental data. It is not known if the inclusion of exotic components like hyperons, antikaon condensates or a phase transition inside the NS core would effect the universality relations. This is one of the main goals of the

present work. We are also motivated to study the effect of higher rotational frequencies on the universality relation between normalized I and $\mathcal{C}$.

3.2 Results

We generate the EoS of cold, β-stable NS within the frame work of RMF model with DD2 parameter set. We study various properties of rotating NSs for our EoSs. As there is no analytical self-consistent solution for the space-time, several numerical codes are developed to study the rotating relativistic stars. We use RNS code [104], which constructs models of rapidly rotating, relativistic, compact stars using Komatsu, Eriguchi and Hachisu (KEH) scheme [105]. Here the field equations and the equation of hydrostatic equilibrium are solved iteratively by fixing the central energy density and any of the other variables such as mass, rest mass, angular velocity, angular momentum or the ratio of polar radius to the equatorial radius until convergence. We run the code for our tabulated, zero-temperature EoSs, consisting of energy density, pressure, enthalpy and number density. The code also incorporates modifications by Cook, Shapiro and Teukolsky [106], where a new radial variable is introduced that maps semi-infinite region to the closed region, unlike KEH scheme. In KEH scheme, the region of integration was truncated at a finite distance from the star.

The different sets of EoSs (P versus ϵ) are plotted in Fig. 3.1 and denoted by their respective compositions. In the Fig. 3.1(a), we plot the nucleons-only (np) EoS in red; neutron, proton, Λ (npΛ) EoS in blue; neutron, proton, Λ, Σ^-, Ξ^0 (np$\Lambda\Sigma\Xi$) EoS in cyan; neutron, proton, Λ, Ξ^0, Ξ^- (np$\Lambda\Xi$) EoS in green and neutron, proton, Λ, Ξ^0, Ξ^-, antikaon condensates (np$\Lambda\Xi K$) EoS in maroon. Presence of hyperon makes the EoS softer compared to nucleons-only case. For npΛ EoS Λ appears at $2.20n_0$, for np$\Lambda\Sigma\Xi$ EoS Σ^- and Ξ^0 appear at $2.48n_0$ and $6.26n_0$ respectively. Presence of Σ^- does not allow Ξ^- in the system. Finally for np$\Lambda\Xi$, Ξ^- and Ξ^0 appear at $2.44n_0$ and $7.93n_0$ respectively [81].

The study of kaonic atoms suggests an attractive optical potential for the antikaons in nuclear matter. However, there is no definite consensus how deep the potential is. We report our results for a set of values of $U_{\bar{K}}$ from -60 to -140 MeV in Fig. 3.1(b). These EoSs are for neutron, proton and antikaon condensates (denoted by np$K$). The deeper the antikaon potential in nuclear medium, softer is the EoS. In Fig. 3.1(a), we also consider the presence of Λ and Ξ hyperons as well as the antikaon condensates. Since early presence of hyperons delay the appearance of K^- condensates to higher density, effect of K^- condensates is only considerable for $|U_{\bar{K}}| \geq 140$ MeV. So we consider neutron, proton, Λ, Ξ, antikaon condensates (np$\Lambda\Xi K$) for $U_{\bar{K}} = -140$ MeV only in Fig. 3.1(a).

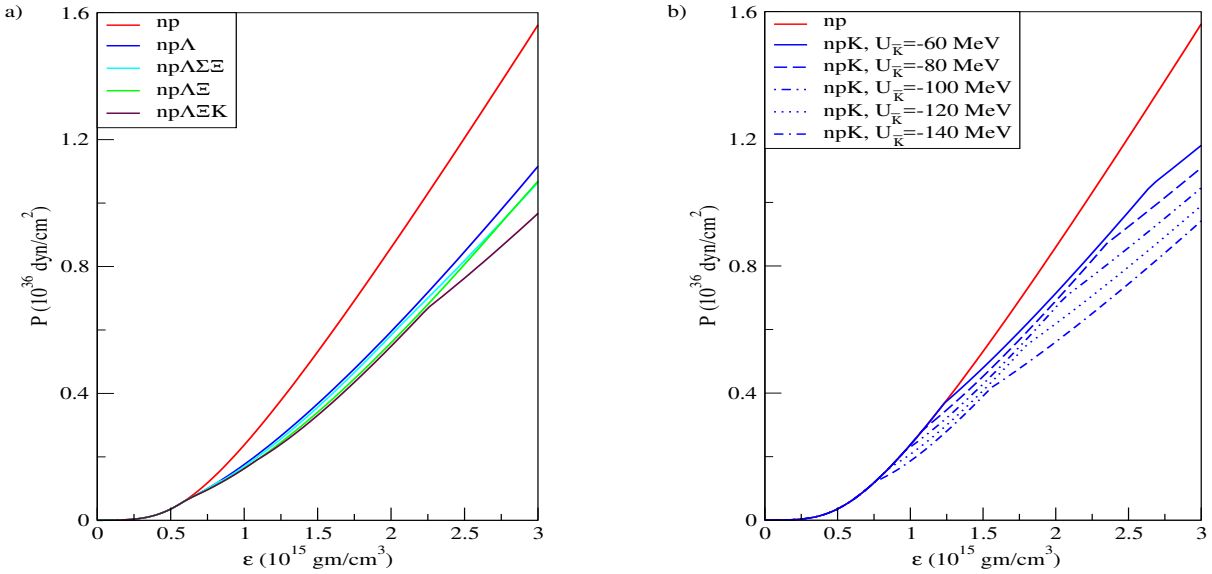

FIGURE 3.1: EoS for different compositions: a) np=red, npΛ=blue, npΛΣΞ=cyan, npΛΞ=green, npΛΞK=maroon respectively. b)np and npK for different $U_{\bar{K}} = -60$ to -140 MeV.

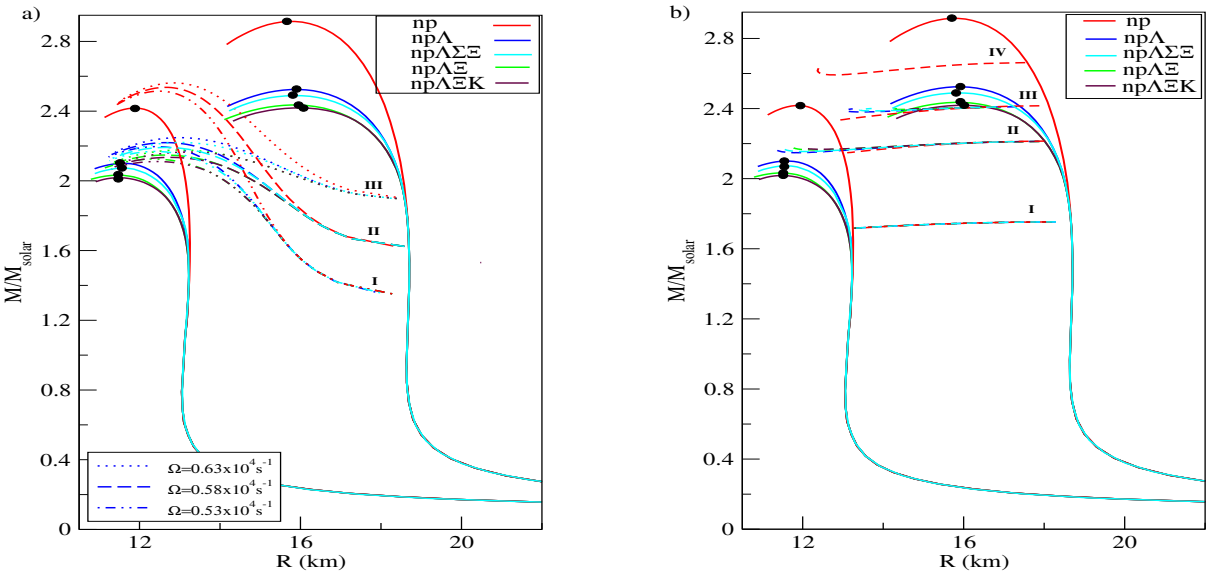

FIGURE 3.2: M-R profiles for NSs with different compositions at static & Kepler limit. In between static and Kepler sequences are a)Fixed angular frequency curves I, II and III for Ω=5300,5800 and 6300 s^{-1} respectively. b) Rest mass curves I, II, III and IV for rest mass M_R= 1.92, 2.49, 2.75, and 3.23 M_{solar} respectively.

In Figures 3.2(a) and 3.2(b), we plot the gravitational mass as a function of equatorial radius for different compositions (np, npΛ, npΛΣΞ, npΛΞ, npΛΞK, denoted by red, blue, cyan, green and maroon respectively). The gravitational mass of NS for static sequence and the sequence rotating at their Kepler frequencies are represented by solid lines at the left and right extremes. The solid circles on these sequences indicate the maximum masses for the sequences. We notice in Fig. 3.1(a), the overall EoS is softer as we increase the degrees of freedom in the form of exotic particles. This leads to fall of maximum mass values from np to npΛΞK in both the

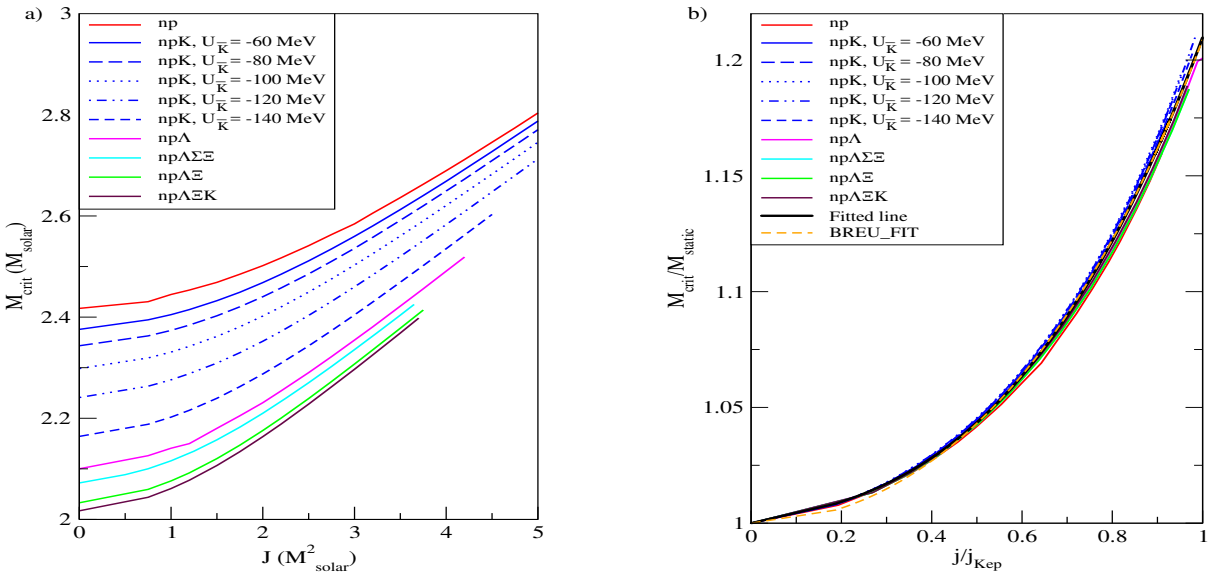

FIGURE 3.3: a) Critical mass versus the angular momentum. b)Normalized critical mass (M_{crit}/M_{static}) versus normalized angular momentum, where, $j = J/M^2_{crit}$.

static and mass shedding sequences. However, the corresponding radius does not change much with the composition.

The maximum mass and corresponding radius of the star with different composition for static and Kepler sequences are listed in Tables 3.1 and 3.2. We would like to study the effect of rapid rotation on the universal relations in case of millisecond or sub-millisecond PSRs. The fastest rotating PSR observed until now has a frequency 716 Hz or angular velocity $\Omega \approx 4500 s^{-1}$. Our choice of angular velocity (Ω) values ($5300, 5800$ & $6300 s^{-1}$) are slightly more but of the same order of magnitude. We notice that a star rotating at its maximum possible frequency i.e. Kepler frequency, can support more mass compared to the static one. As the centrifugal force increases with the rotational velocity, the stars tend to have larger radii. For each set of EoS the maximum mass increases almost by 20% from static to Kepler. In between static and Kepler sequences, three fixed angular velocity sequences are plotted in Fig. 3.2(a) for $\Omega = 6300, 5800$, and $5300\ s^{-1}$ denoted by dotted, dashed and dash-dotted line respectively. The lines with different constituents but same frequency converge for relatively larger stars, whereas for smaller stars different frequency lines merge for same set of constituents. Or in other words, mass sequence of the small(large) rotating stars are dependent(independent) of EoS.

In a rapidly rotating NS model, we can follow the quasi stationary evolution of a single star along the constant rest mass sequences. We have two equilibrium sequences termed as "normal" and "supramassive". Normal sequences start rotating with Keplerian frequencies and end up on the static limit, which is stable to quasi-radial perturbation. On the other hand, the supra-massive sequence does not have a corresponding static solution. They have rest masses that are higher than their static (TOV) counterparts. In Fig. 3.2(b), we draw the fixed rest mass curves in between the static and Kepler limits. The horizontal curves denoted by I, II, III and IV are for

rest mass, $M_R = 1.92$, 2.49, 2.75 and 3.23 M_{solar} respectively. All the lines in I, np (red) in II and III are normal sequence; np (red) in IV, npΛ (blue), npΛΣΞ (cyan), npΛΞ (green) and npΛΞK (maroon) lines in II and III are supramassive. The red dashed line marked as IV is for $M_R = 3.23 M_{solar}$. This value is well above the maximum mass for the exotic EoS, here we have a single sequence corresponding to np EoS only. Stars on the supramassive sequence may evolve keeping their rest mass constant but changing the spin rate. The stars on the supramassive sequences typically lose energy and angular momentum very slowly by emitting radiation. As they reach the point of quasi-radial instability, they rapidly spin up before collapsing into a black hole [107].

In Fig. 3.3(a), we plot the critical masses i.e., the maximum masses of the constant angular momentum stellar models, such that $(\partial M/\partial \rho_c)_J = 0$, where ρ_c is the central density. Beyond this point the stellar models become unstable. The critical masses vary considerably when plotted with the angular momentum as seen in Fig. 3.3(a). Each sequence starts at $M_{crit} = M_{static}$, where M_{static} is the maximum mass of a non-rotating sequence and ends at maximum angular momentum $J = J_{Kepler}$ with $M_{crit} = M_{Kepler}$. They vary for different EoS. Larger mass of stellar configurations, for example np, supports higher Kepler frequency or angular momentum as can be seen from Fig. 3.3(a). However, the percentage change of stable mass configuration as the static star spins up to its Kepler limit is similar ($\sim 16 - 20\%$) for all the EoSs. So we draw the same plots in Fig. 3.3(b), but in terms of dimensionless quantiles M_{crit}/M_{static} and normalized angular momentum where, $j = J/M_{crit}^2$ and $j_{Kepler} = J_{Kepler}/M_{Kepler}^2$. We observe that the relation between normalized critical masses and normalized angular momentum does not vary much with the given EoS. We find a universality (a 20% rise of M_{crit} value over M_{static} for all the EoSs) in the normalized mass-angular momentum profile. We plot a best-fit line $M_{crit}/M_{static} = 1 + a_1 x + a_2 x^2 + a_3 x^3$, where $x = j/j_{Kepler}$ and the coefficients are $a_1 = 0.3363$, $a_2 = 0.3829$, $a_3 = 0.138$. This treatment is particularly useful to compute the maximum mass configuration allowed by uniform rotation in terms of its corresponding static sequence for all the EoS. Similar features have been reported in Ref [59] for nucleonic EoS, though their best fit parameters are slight different from ours. The dashed line with their parameters does not fit our data well at lower j/j_{kep}.

In Fig. 3.4(a), we plot the variation of I with gravitational mass for EoS with different constituents at the Kepler frequency. For a NS of known mass and I, we can deduce the radius using I versus M and M versus R graphs. This eventually would help us constrain the EoS and confirm if the NS contains exotic core or not. In Fig. 3.4(a) I values are plotted for np, npΛ, npΛΣΞ, npΛΞ and npΛΞK ($U_{\bar{K}} = -140$ MeV) as well as for np$K$; $U_{\bar{K}}$ varies from -60 to -140 MeV. It is noted that I is maximum for stiffer EoS, i.e. for np, it can support a heavier and more compact star. The maximum I curve however does not correspond to the maximum NS mass and the corresponding radius. The values of maximum I and the corresponding masses, radii and angular velocity are listed in Tables 3.3 and 3.4. Currently, for PSR J1614-2230, the lower

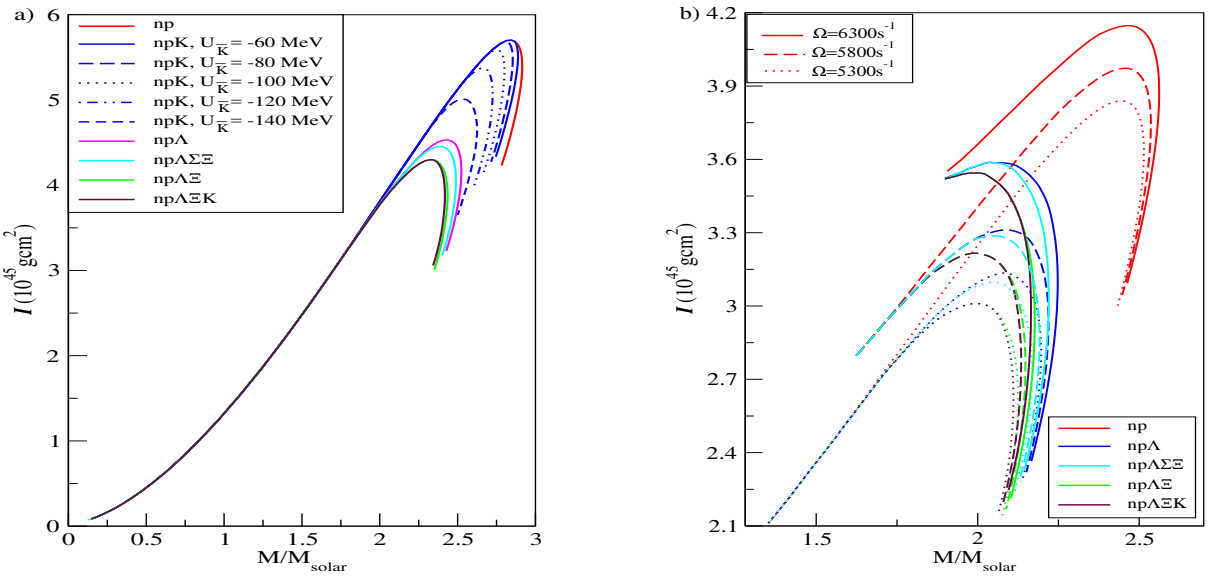

FIGURE 3.4: I versus M for different compositions of NSs rotating a)at Kepler frequency b)at different angular frequencies.

limit of I is estimated to be $10^{45} g\, cm^2$ from γ-ray flux measurement [108]. This value is not very constraining due to uncertainty in the distance of the pulsar. The accuracy is expected to improve highly with the upcoming SKA results.

In Fig. 3.4(b), I is plotted for different angular velocities (Ω=5300,5800 and 6300 s^{-1}). We have considered np, npΛ, npΛΣΞ, npΛΞ and npΛΞK EoS. I is less for a star rotating at $\Omega = 5300 s^{-1}$ compared to that of $6300 s^{-1}$.

The I versus the angular velocity for all np, npΛ, npΛΣΞ, npΛΞ and npΛΞK cases are plotted in Fig. 3.5(a). Here also the same colour scheme is used for different compositions as in Fig. 3.1. We find that I is lower for softer EoS (npΛΞK) compared to the stiffer ones (np, npΛ etc) at a particular angular frequency. The four solid lines represent I at Kepler frequency, each of those increase to a peak but falls for a relatively slower pulsar. For stiffest EoS, np, I peaks at $\Omega = 8740 s^{-1}$, while the maximum occurs at $\Omega = 7840 s^{-1}$, $7660 s^{-1}$, $7520 s^{-1}$, $7510 s^{-1}$ for npΛ, npΛΣΞ, npΛΞ and npΛΞK ($U_{\bar{K}} = -140 MeV$) respectively (See Table 3.3). We notice that the maximum angular velocity of rotating NSs is quite sensitive to the EoS. An EoS predicting smaller Keplerian frequency than the observed frequency can be ruled out and thus be useful in constraining EoS. We also plot fixed rest mass (M_R) sequences in the same figure, which show different behaviour for different M_R and EoS. To understand the nature of I curves in Fig. 3.5(a), we study the variation of mass and radius terms with respect to angular frequency. We mention these results only qualitatively to analyze Fig. 3.5(a) (not shown in separate graphs). For $M_R = 1.92 M_{solar}$, the sequences are found at lower Ω region. Stars that are less massive can not sustain rapid rotation. We notice both the mass and radius decrease monotonically at this angular frequency range, which explains the nature of I curves. Also, The variation of I with different compositions is negligible in this case. This is quite expected as we find in

TABLE 3.1: Maximum mass (in M_{solar}) and the corresponding radius (in km) of compact stars with nucleons, hyperons and antikaons in DD2 model. $U_{\bar{K}}$ =-140 MeV for $np\Lambda\Xi K$ matter. The values in the parentheses are for the Kepler sequences.

	$M_{static[Kepler]}$ (M_{solar})	$R_{static[Kepler]}$ (km)
np	2.42[2.91]	11.91[15.68]
npΛ	2.10[2.52]	11.55[15.94]
npΛΣΞ	2.07[2.48]	11.56[15.82]
npΛΞ	2.03[2.43]	11.49[15.97]
npΛΞK	2.01[2.41]	11.49[16.02]

TABLE 3.2: Same as Table 3.1 but for compact stars with nucleons and antikaons for different values of optical potential depth in the DD2 model. The values in the parentheses are for the Kepler sequences.

$U_{\bar{K}}$(MeV)	$M_{static[Kepler]}$ (M_{solar})	$R_{static[Kepler]}$ (km)
-60	2.37[2.88]	12.19[16.10]
-80	2.34[2.85]	12.20[16.38]
-100	2.29[2.80]	12.18[16.45]
-120	2.24[2.72]	12.05[16.47]
-140	2.16[2.62]	12.03[16.27]

TABLE 3.3: Maximum I and corresponding masses, radii and angular velocity of compact stars with nucleons, hyperons and antikaons in the DD2 model. $U_{\bar{K}}$ =-140 MeV for $np\Lambda\Xi K$ matter.

	I $(10^{45} g\ cm^2)$	M (M_{solar})	R (km)	Ω $(10^4\ s^{-1})$
np	5.70	2.84	16.8	0.874
npΛ	4.53	2.43	17.2	0.784
npΛΣΞ	4.45	2.38	17.4	0.766
npΛΞ	4.30	2.32	17.5	0.752
npΛΞK	4.30	2.32	17.5	0.751

TABLE 3.4: Same as Table 3.3 but for compact stars with nucleons and antikaons for different values of optical potential depth in the DD2 model.

	I $(10^{45} g\ cm^2)$	M (M_{solar})	R (km)	Ω $(10^4\ s^{-1})$
-60	5.70	2.84	16.8	0.874
-80	5.68	2.81	16.94	0.860
-100	5.59	2.74	17.22	0.832
-120	5.37	2.67	17.33	0.814
-140	5.01	2.53	17.5	0.780

horizontal curve I of Fig. 3.2(b) that all EoSs merge together for $M_R = 1.92 M_{solar}$. The central energy density of a $1.92 M_{solar}$ static star differs from 7 to $7.96 \times 10^{14} g/cm^3$ for np to npΛΞK, whereas hyperons start populating at $5.91 \times 10^{14} g/cm^3$. The corresponding central density for a $M_R = 1.92 M_{solar}$ star rotating with Kepler frequency is only $5.9 \times 10^{14} g/cm^3$, so the effect of exotic particles is not there. The supra-massive star sequence $M_R = 2.49 M_{solar}$ also falls monotonically as Ω decreases in case of all EoSs (long dashed lines). However the monotonic fall is followed by a sudden spin-up with a slight loss of I for this supra-massive sequence when the star contains exotic components.

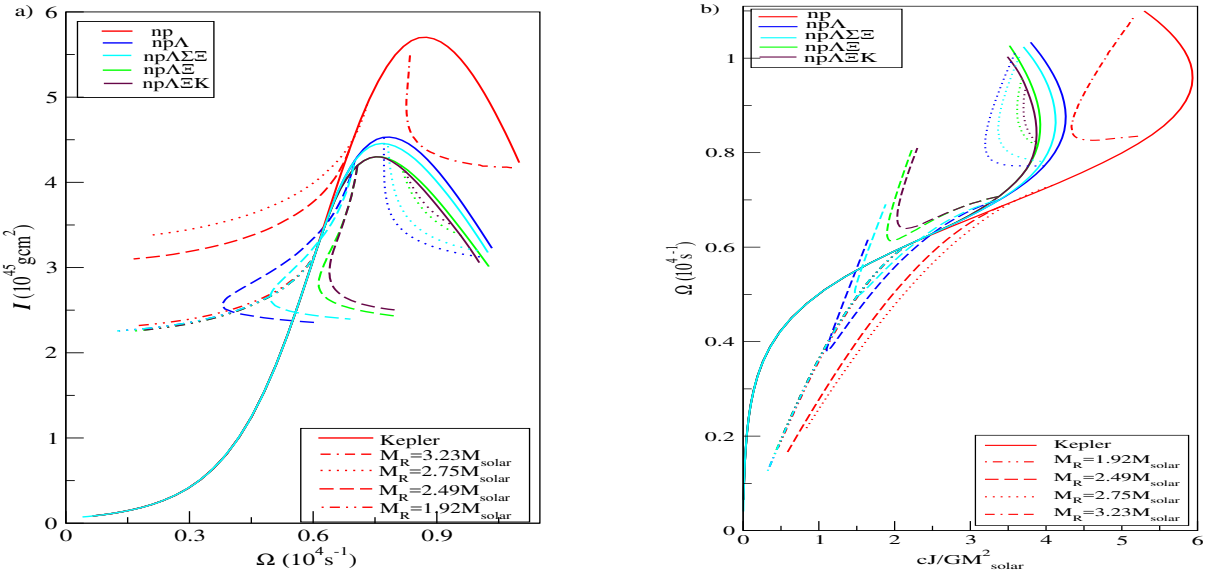

FIGURE 3.5: a)I versus Ω. b)Ω versus angular momentum (cJ/GM^2_{solar}). The solid lines correspond to Kepler frequency. Others are for different fixed rest mass sequences.

The nature of bending is different for different EoS and can be justified by following the variation of mass and radius with Ω. Both of them decrease initially with decreasing Ω to rebound at a particular angular frequency suddenly. Along a supra-massive sequence of a pulsar as Ω decreases, a spin up followed by a second spin down after the initial one in the I versus Ω plane was reported in Ref [109, 110, 111]. This phenomenon is known as the back bending (S-shaped curve in the plot) and was attributed to the phase transition from nuclear matter to some exotic (hyperon, antikaon condensed or quark) matter. Interestingly, for the supra-massive sequence ($M_R = 2.75 M_{solar}$, the dotted curves), value of I falls off with higher angular velocity for the exotic EoS. However, $M_R = 2.49$ as well $2.75 M_{solar}$, corresponding to red long dashed and dotted lines, are normal sequences for np EoS and follow the same characteristic fall with decreasing Ω like the normal sequence ($M_R = 1.92 M_{solar}$). Stars at normal sequences do not exhibit spin up even if they lose energy and angular momentum. This was also observed by Cook et. al [107]. The red dot dashed line is supramassive for np ($M_R = 3.23 M_{solar}$) and follows the same nature as the other exotic supramassive sequences with $M_R = 2.75 M_{solar}$. For supramassive sequences, we also notice that the size of the star increases at low rotation speed. Though it can

support a higher mass at higher rotation speed like the normal sequence, at low speed a higher mass star can be supported again. We show the variation of Ω with the angular momentum J in Fig. 3.5(b) for the same sets of parameters as in Fig. 3.5(a). This helps us to check the stability of the rotating configurations [110]. The condition for instability along a constant rest mass sequence is $\frac{dJ}{d\epsilon_c} \geq 0$ [43]. Supramassive sequences terminate at different values of Ω below which the instability appears. It is found that angular momentum initially decreases with central energy density. After the stable region, J starts increasing with ϵ_c. We notice the increase of J as the star spins up subsequently. This marks the instability in the configurations with respect to axisymmetric perturbations.

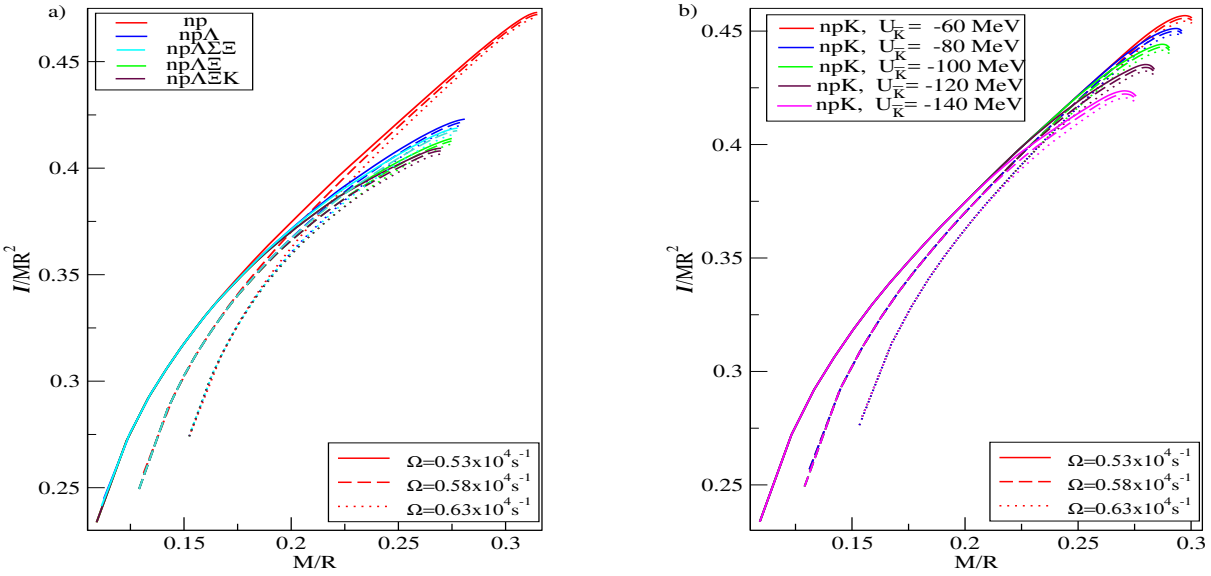

FIGURE 3.6: Normalized $I(I/MR^2)$ with $\mathcal{C}$ for a)np, npΛ, npΛΣΞ, npΛΞ, npΛΞK, $U_{\bar{K}} = -140MeV$ b)np$K$ with different $U_{\bar{K}}$

The dependence of I/MR^2 with $\mathcal{C}$ is drawn in Fig. 3.6(a). It was shown by Lattimer and Schutz that other than very soft EoS, which gives a maximum mass of the order of $1.6M_{solar}$, a relatively unique relation existed between I/MR^2 and M/R [35]. We, however note that though at lower $\mathcal{C}$, I/MR^2 is independent of EoS, it clearly varies differently for different EoS at higher $\mathcal{C}$; it is quite less for the soft EoS compared to nucleons-only EoS. I/MR^2 term on the other hand depends on angular velocity Ω at lower $\mathcal{C}$. It is less for a star spinning at higher rotational speed. The dependence on Ω is not that prominent at higher $\mathcal{C}$. At this point we recall that all our EoSs yields a maximum mass not less than $2M_{solar}$ (See Tables 3.1, 3.2). Still we find deviation from universality at higher $\mathcal{C}$ for different constituents. We notice at low $\mathcal{C}$, which is near Kepler frequency, the central energy density is such that hyperons or antikaons do not populate. So all the EoSs are identical. Naturally, here I/MR^2 is independent of EoS. However, at higher $\mathcal{C}$ when the central energy density is high enough to populate exotic particles, I/MR^2 varies differently for different EoS. The deviation for a particular $\mathcal{C}$ (say 0.25-0.27) varies between 5-7%

from np to npΛΞK EoS. If we consider the highest Keplerian frequency, the difference between np and npΛΞK EoS can be as high as 14%.

Similar trend is noticed for rapidly rotating stars from Fig. 3.6(b) also: I/MR^2 for np$K$ at different $U_{\bar{K}}$, is independent of EoS only at low $\mathcal{C}$. The difference of I/MR^2 for softest and stiffest EoS at Keplerian frequency is $\sim 7\%$, whereas for a compactness 0.27, this varies around 2.5% as we change the optical potential of antikaons in nuclear matter from -60 MeV to -140 MeV. On an average these deviation from universality is of the same order as reported by Breu and Rezzolla for nucleonic EoS [59].

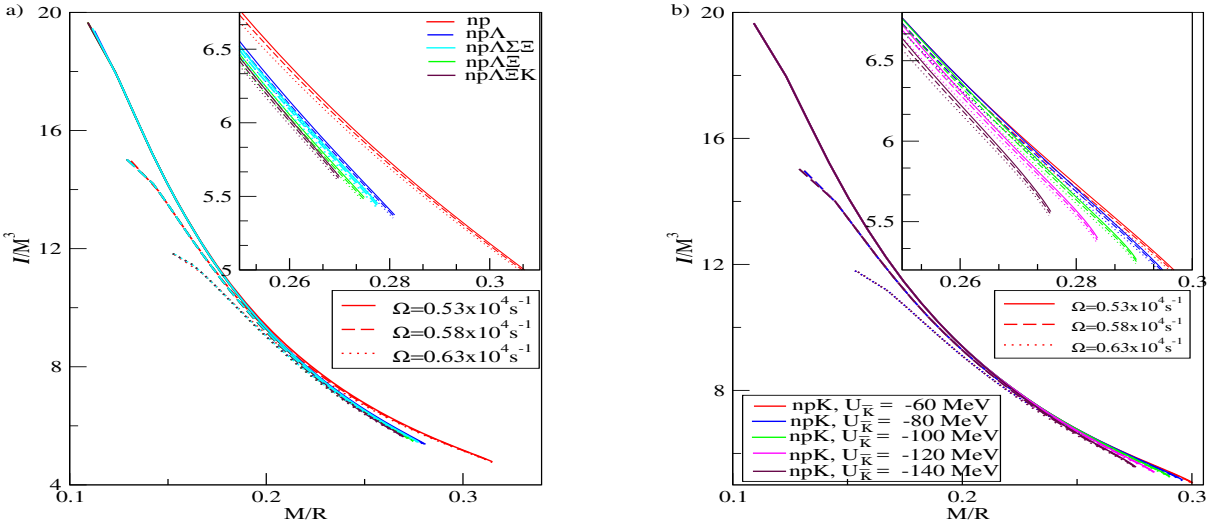

FIGURE 3.7: Normalized $I(I/M^3)$ with $\mathcal{C}$ for a) np, npΛ, npΛΣΞ, npΛΞ, npΛΞK, $U_{\bar{K}} = -140MeV$ b) np$K$ with different $U_{\bar{K}}$

We exhibit variation of I in terms of another dimensionless quantity, I/M^3 with $\mathcal{C}$ for np, npΛ, npΛΣΞ, npΛΞ, npΛΞK in Fig. 3.7(a) [59]. The three distinct bunches of lines differ in their angular velocity values Ω, increasing from top to bottom. It is clearly seen that I/M^3 is also not affected by the different EoS and respects universality relation at lower $\mathcal{C}$. However, at higher $\mathcal{C}$, a slight deviation from universality is evident. This part is zoomed in the inset. At a particular M/R value, I/M^3 drops considerably from np to npΛΞK EoS. In Fig. 3.7(b), we look into the variation of I/M^3 with $\mathcal{C}$ for np$K$ case. Here we consider different optical potential of antikaons $U_{\bar{K}} = -60$ to -140 MeV. The effect is similar as in Fig. 3.6(b). The variation of I/M^3 is dependent on Ω values at lower $\mathcal{C}$, it decreases for a faster rotating star. The variation with different composition i.e., EoS at higher $\mathcal{C}$ is clearly visible in the zoomed inset.

Finally in Fig. 3.8, we show the variation of the normalized I for the rest mass sequences I, II, III and IV of Fig. 3.2(b). Fixed rest mass sequence has also been used by Martinon et. al [112] to study quasi-stationary evolution of I-love-Q universal relations for a particular EoS.

In Fig. 3.8(a), we note I/MR^2 changes appreciably with EoS for supra-massive sequences, however is practically independent of EoS for normal sequence ($1.92M_{solar}$ rest mass). The same pattern is noted for I/M^3 in Fig. 3.8(b). The anomalous behavior between the normal and supramassive sequences in Fig. 3.8(a) and Fig. 3.8(b), may be explained as the difference between the evolutionary track of an isolated star of sequences. While the normal sequence stars never spin up, the ones in the supramassive sequence spin up differently depending on their EoSs. The universality is a signature of a balance between gravity and the response of matter to gravity. These supramassive sequences seem to disrupt the balance.

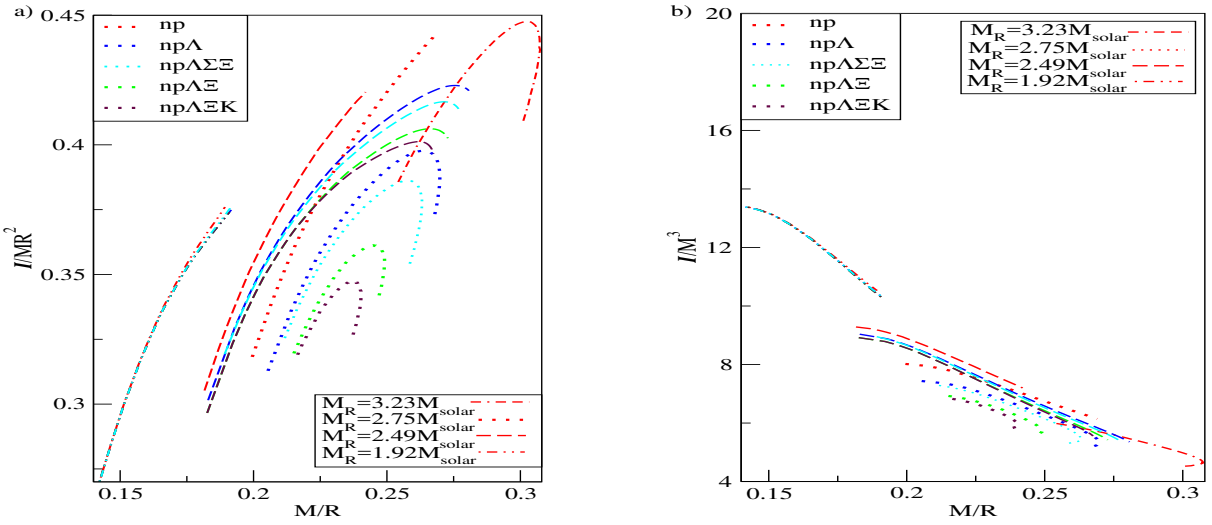

FIGURE 3.8: Normalized I as a function of $\mathcal{C}$ a) I/MR^2 versus $\mathcal{C}$ b)I/M^3 versus $\mathcal{C}$ for the rest mass sequences $M_R = 1.92$, 2.49, 2.75 and $3.23M_{solar}$.

3.3 Discussion and Conclusion

Our main objective in this chapter is to study the I and different universal relations associated with it for a NS that has several exotic particles such as hyperons (Λ, Ξ, Σ), antikaon condensates in its high density core. We have constructed a set of EoSs incorporating these exotic components individually as well as considering all of them together in the framework of a density dependent hadronic field theory using the DD2 parameter set. All our EoSs satisfy the $2M_{solar}$ observational constraint. We employ them to study the structure of rapidly rotating NSs. Also as the stars spin up, the maximum masses they can support go up and the stars become larger in size for all the EoSs considered. In this connection, we consider the equilibrium mass of the star at maximum angular momentum, beyond which the configuration becomes unstable and call this mass as critical mass following Ref [59]. We find that though different EoS give rise to different maximum masses and end up at different angular momenta, the maximum mass supported by rotation is almost 16-20% more than that supported by their corresponding static sequences for

all the EoSs. Hence, we express this critical mass sequences of rapidly rotating stars in terms of the static mass solution and normalized angular momentum and show that a universal relation holds irrespective of the different constituents or EoS, the variation at Kepler limit being 20% larger than the static limit. This number is in full agreement with the results for nucleonic EoS by Breu and Rezzolla [59].

Next we focus on I for different compositions and explore its variation with mass. The larger the value of I, the larger is the maximum mass supported by the stellar models, and more compact is the star. Also, stiffer EoS can withstand higher angular velocity. We came to these conclusions for the dense matter containing exotic degrees of freedom. We followed the fixed rest mass sequences of stellar models, both normal and supramassive and studied the variation of I. Along normal sequences, I falls off monotonically as the stars spin down. However, for the supramassive cases, we notice sudden spin up of the stars following a spin down. I drops drastically during the spin down, but the fall of I is not so prominent during the subsequent spin up. This effect was maximal in the npΛ case.

Next, we study the universal relations for normalized I. They are very useful tools in astrophysics. With the upcoming SKA telescope, measurement of I may be accomplished soon, which will help constraining the EoS. However, it is incredibly difficult because of a few things. First of all, there are very few relativistic binaries where the effect of I on the periastron advance at 2PN can be observed. Then, in addition to periastron advance, at least two other post-Keplerian parameters are needed to be measured precisely. Even if the effect of spin orbit coupling is strong enough, we need to accumulate data of periastron advance for a minimum 20% time of the precision period of the pulsar to get a minimum accuracy of 10% in the I measurement. The precision period of one of the most suitable candidates for this measurement, PSR J0737-3039, is 75 years. Hence, both mass and I measurements are needed to be combined with the universal relations to get more accurate estimation of the radius as emphasized also by Breu and Rezzolla [59].

That is why it is vitally important to know if universality relations hold for the EoS with considerable softening at higher densities in the presence of hyperons and antikaon condensates etc. Therefore, we study the variation of normalized I with respect to $\mathcal{C}$ for all the constituents np, npΛ, npΛΣΞ, npΛΞ, npΛΞK ($U_{\bar{K}} = -140$ MeV) and np$K$ ($U_{\bar{K}} = -60$ to -140 MeV). I is normalized with respect to MR^2 as well as M^3. We report a 10% deviation on an average from universality at higher $\mathcal{C}$ for all the EoSs. However, at lower $\mathcal{C}$, the normalized I is independent of our choice of composition, only vary with angular velocity. We also investigate the normalized I vs $\mathcal{C}$ relations for fixed rest mass sequences. The variation is quite large for supramassive sequences, while practically insensitive for the normal sequences. Thus, we conclude that except from the supramassive sequence stars, the universality relations holds true for a normal star with exotic components, as the deviation from universality is of the same order for stars with only nucleonic EoS previously reported.

Chapter 4

Properties of Massive Rotating Protoneutron Stars with Hyperons: Structure and Universality

4.1 Introduction

The PNS, formed just after the supernova explosion of a massive, main sequence star, is believed to have four prominent stages of evolution as it ends up as a cold catalyzed object [48, 71]. These are governed strongly by the nature of matter at very high density as well as the neutrino reaction rates and diffusion timescales. There have been many detailed studies on the global properties of the PNS with different microphysical inputs [113, 114, 115]. The simplified models of post-bounce neutrino emission [71, 115] have advanced to full solutions of the Boltzmann equation [116], with more realistic microphysics [117] in the last few years. These studies of PNS cooling used the equilibrium flux-limited diffusion (EFLD) approximation, while the variable Eddington factor method was used for neutrino transport [118].

Several studies have been done to investigate the effect of hyperons on the structure of PNS [119, 120]. But, they used mostly older EoS parametrizations which are not consistent with the recent observations or the latest experimental data. Therefore, it is our objective to revisit the problem with more suitable microphysical inputs and find out the sensitivity of these results with respect to the parameters of the theory. In this work, we will mainly focus on the dense nuclear matter containing hyperons and study its effect on global properties of massive PNS at four different stages of evolution, starting from neutrino-trapped, isoentropic PNS to cold catalyzed β-equilibrated NS. Keeping that in mind, we employ a realistic EoS including hyperons for this work. Incidentally, we construct new EoSs for the neutrino-trapped, isentropic matter and use them to study the initial stages of PNS evolution. As a matter of fact, only the electron-type

neutrinos become trapped during the core collapse. Therefore, we have considered only the electron-type neutrinos in our study . In the neutrino-trapped matter, the electron lepton number $Y_{Le} = Y_e + Y_{\nu_e} = 0.4$ [48]. Also, as no muons are present when the neutrinos are being trapped, the constraint $Y_{L\mu} = Y_\mu + Y_{\nu_\mu} = 0$ can be imposed. Hence we fix the lepton fraction $Y_L = 0.4$ in our calculation.

Another objective of this work is to study the universal relations recently discovered among various global quantities of compact objects such as normalized I and stellar compactness [35, 56, 59]. In the context of the PNS evolution, $\bar{I} - \bar{Q}$ relation has been studied by Martinon et al. [112] for nucleon-only EoS. They have found that the universality is broken during the initial stages after the core bounce, but it is satisfied at later stages. Recently, Marques et al. [76] also investigated the problem for rapidly rotating hot stars with hyperonic EoS. They found that the relation does not change in the presence of hyperons but deviates for high entropy. However, the $\bar{I}$ vs $\mathcal{C}$ relations has not been studied for the PNS till now. Previously, Breu and Rezzolla studied a large set of cold nucleonic EoSs with different stiffness and showed that universality relation holds for normalized I [59]. We report these relations in the presence of exotic components like hyperons and antikaon condensates for cold NS in the previous chapter [121]. In this work, we examine the $\bar{I}$ vs $\mathcal{C}$ relations for PNS using the fitting factors provided by Breu and Rezzolla [59].

4.2 Stages of PNS Evolution

Within a few milliseconds after the core bounce, the hydrostatic equilibrium is reached in the lepton-rich core and the star enters the Kelvin-Helmholtz cooling phase which lasts for about 10s [48, 71, 115]. In this phase, the evolution is completely determined by the neutrino diffusion. This is the formation phase of the star. The central temperature and entropy keep on increasing despite neutrino loss. The whole star starts to cool down as a whole and the total entropy decreases significantly at 20s. It fully deleptonizes at about 30s [72] and β-equilibrium is reached. Ultimately, after one minute the temperature drops down to ~ 1 MeV. We follow a well established evolutionary scenario [48, 71] that suggests that the PNS undergoes roughly four stages of evolution towards becoming a stable, cold catalyzed compact object. This picture has been used by many people to study PNS [119, 120, 122].

1. Just after its birth, the PNS initially has trapped neutrinos and the lepton fraction is $Y_L = 0.4$. The core of the PNS has an entropy per baryon $s_B = 1$ surrounded by a high entropy, neutrino trapped outer layer, which deleptonizes faster than the core.

2. While the outer layer is being deleptonized, the central object is still neutrino trapped with $Y_L = 0.4$ and the neutrino diffusion heats it upto $s_B = 2$.

3. After complete deleptonization, the core becomes neutrino-free and attains high entropy ($Y_\nu = 0, s_B = 2$).

4. Finally, the star settles as a cold stable NS in beta equilibrium.

In the results section, we will denote these four stages with I to IV. Our aim is to study the properties and structure of the star at each of these discrete stages. This way the quasi-stationary PNS evolution has been approximated to reproduce qualitatively the different evolutionary stages. However, this approximate scheme has its own limitation. It does not represent a complete picture of structural evolution of the PNS during the cooling phase.

4.3 Results and Discussions

We study the properties of a massive PNS using DD2 EoS at four different configurations (I - IV) relevant to the PNS evolution mentioned in previous section. Our aim is to study how the emergence of Λ hyperons and their interaction affect the PNS stages. We use three types of EoSs : i) HS(DD2), ii) BHBΛ, and iii) BHB$\Lambda\phi$ for our calculations.

In Fig. 4.1, pressure is plotted against number density. The left panel is for nucleons-only HS(DD2) EoS, the middle and the right panels are for EoSs with hyperons, namely BHBΛ and BHB$\Lambda\phi$. The presence of hyperons softens the EoS. The solid line represents the stage I of PNS evolution i.e. lepton trapped with $s_B = 1$. As the entropy per baryon increases to $s_B = 2$, the EoS (dot-dashed) gets stiffer for all the three variants. Once the neutrinos leave the system, the EoS is softened again (dashed line). The EoS (dotted line) for the cold catalyzed matter is the softest among all. This difference in stiffness is pronounced largest for the BHBΛ EoS, lesser for BHB$\Lambda\phi$, and least for HS(DD2). Neutrinos are produced in large number in the presence of Λ hyperons. This was observed earlier in Ref. [48]. Consequently, as the PNS passes from stage II to III, the loss of lepton pressure softens the EoS considerably for BHBΛ and BHB$\Lambda\phi$. If we compare the EoS for any particular stage, it becomes evident that the HS(DD2) is always the stiffest among the three, followed by BHB$\Lambda\phi$ and BHBΛ respectively. The difference in stiffness among the four evolutionary stages is most pronounced for the softest EoS.

M versus R for the corresponding EoSs of Fig. 4.1 are plotted in Fig. 4.2. Here also, we follow the same line style as Fig. 4.1. We find that the stiffer EoS yields a higher maximum mass, as expected. However, the difference in their corresponding radii is not so prominent. The maximum gravitational mass and their corresponding radii for static configuration are given in Table 4.1. We also notice that the hotter stars with comparatively smaller masses have larger radii than their cold counterparts. This can be attributed to the higher thermal pressure of the hot stars. Finally, our results corroborate the general notion that in nucleon-only system

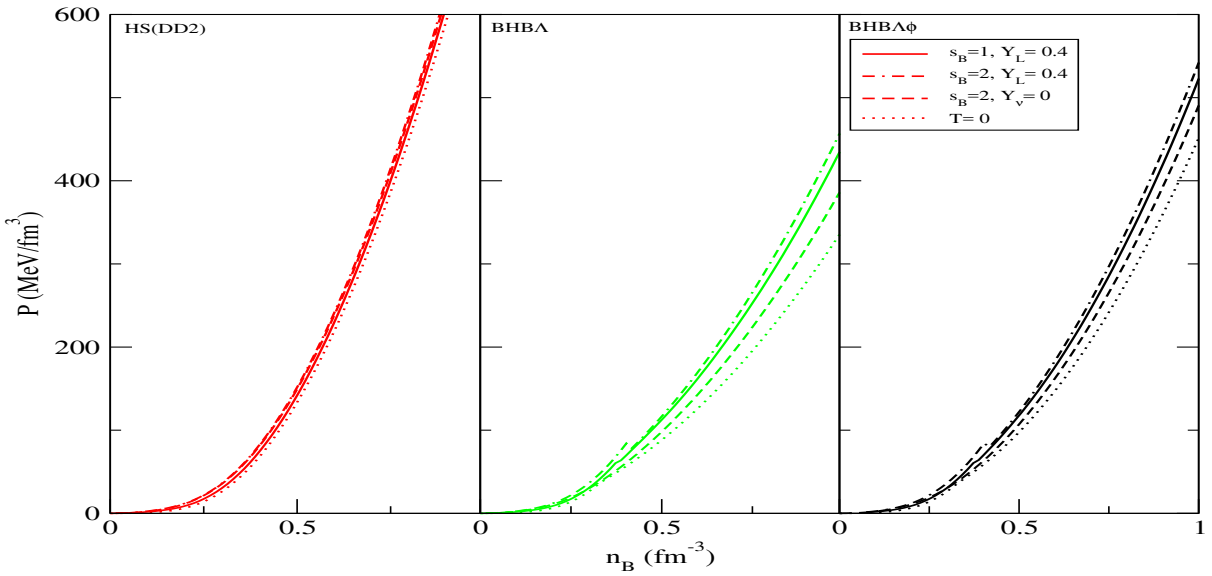

FIGURE 4.1: EoS for discrete evolutionary stages of the compact star. The three panels from left to right are for HS(DD2), BHBΛ and BHBΛϕ EoSs respectively.

TABLE 4.1: Maximum Gravitational Mass (in M_{solar}) & the corresponding Radius (in km) of static stars in the presence of Λ hyperons at different evolutionary stages.

EoS	Evolution Stages	M (M_{solar})	R (km)
HS(DD2)	s_B=1, Y_L=0.4	2.375	12.610
	s_B=2, Y_L=0.4	2.390	13.181
	s_B=2, Y_ν=0	2.437	12.889
	T= 0	2.423	11.869
BHBΛ	s_B=1, Y_L=0.4	2.108	13.044
	s_B=2, Y_L=0.4	2.150	13.888
	s_B=2, Y_ν=0	2.018	12.713
	T= 0	1.955	11.737
BHBΛϕ	s_B=1, Y_L=0.4	2.172	12.340
	s_B=2, Y_L=0.4	2.202	12.964
	s_B=2, Y_ν=0	2.126	12.488
	T= 0	2.1	11.608

neutrino-trapping reduces the maximum mass of the star, which reverses in the presence of exotic matter such as hyperons, quarks and antikaons [44, 48].

The variation of temperature as a function of baryon density is plotted in Fig. 4.3 for the first three stages of PNS evolution. In each case, the star is hot in the central region; the temperature falls off monotonically towards the surface. In individual panels of Fig. 4.3, we follow the change in temperature for a particular EoS as the PNS evolves. The entropy per baryon of the PNS increases from $s_B = 1$ to $s_B = 2$ leading to a significant increase in the temperature as well as the radius. Inclusion of hyperons lowers the temperature of the central region of the PNS. For example, at $n_B \sim 1\ fm^{-3}$, for HS(DD2) EoS, the temperature increases from ~ 33 to ~ 68 MeV from stage I to II, whereas in the presence of Λ hyperons, this rise is from ~ 27 to ~ 55 MeV.

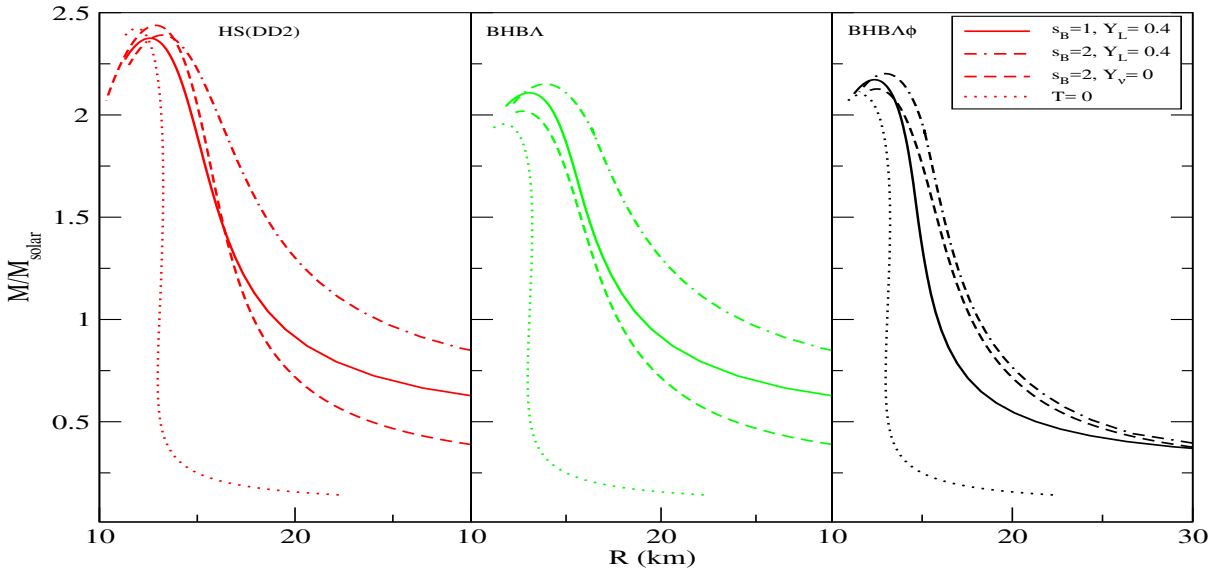

FIGURE 4.2: Gravitational mass versus radius for the corresponding EoSs of Fig. 4.1.

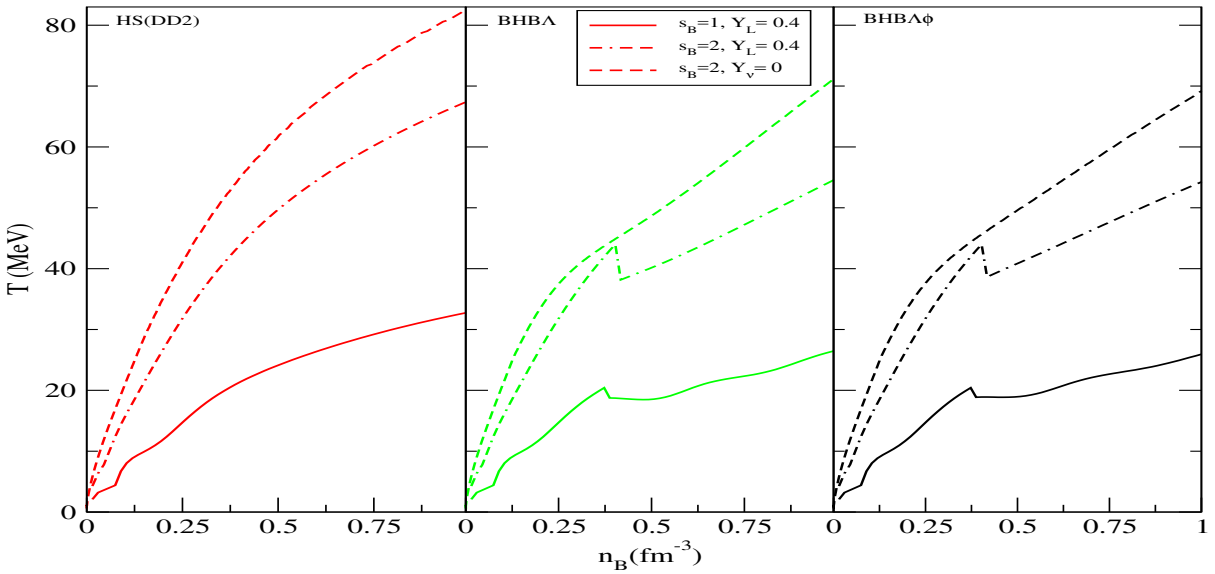

FIGURE 4.3: Temperature profile of the compact star as it evolves from $s_B = 1$, $Y_L = 0.4$ to β-equilibrated NS of $s_B = 2$, for different compositions of matter.

The kinks in the temperature mark the appearance of Λ hyperons. The corresponding threshold densities are listed in Table 4.2. This characteristic is quite expected. The additional degree of freedom, Λ, comes into the system with very low momentum. Hence, the temperature, which is the average kinetic energy per degree of freedom, will drop. When the neutrinos leave the system, the radius decreases as is evident from Fig. 4.2, thereby increasing the temperature by about ~ 15 MeV for all the EoSs, again due to compression. The neutrinos carry away most of the energy. Consequently the star becomes cold at stage IV. On the other hand, the charged particle fraction slightly goes down in order to maintain the constant lepton fraction of $Y_L = 0.4$.

Next, we study the effect of rotation on various stellar properties. Soon after its birth in a

TABLE 4.2: Threshold densities of Λ hyperons (in fm^{-3})

Evolution Stages	BHBΛ	BHBΛϕ
s_B=1, Y_L=0.4	0.387	0.386
s_B=2, Y_L=0.4	0.405	0.404
s_B=2, Y_ν=0	0.374	0.374
T= 0	0.325	0.329

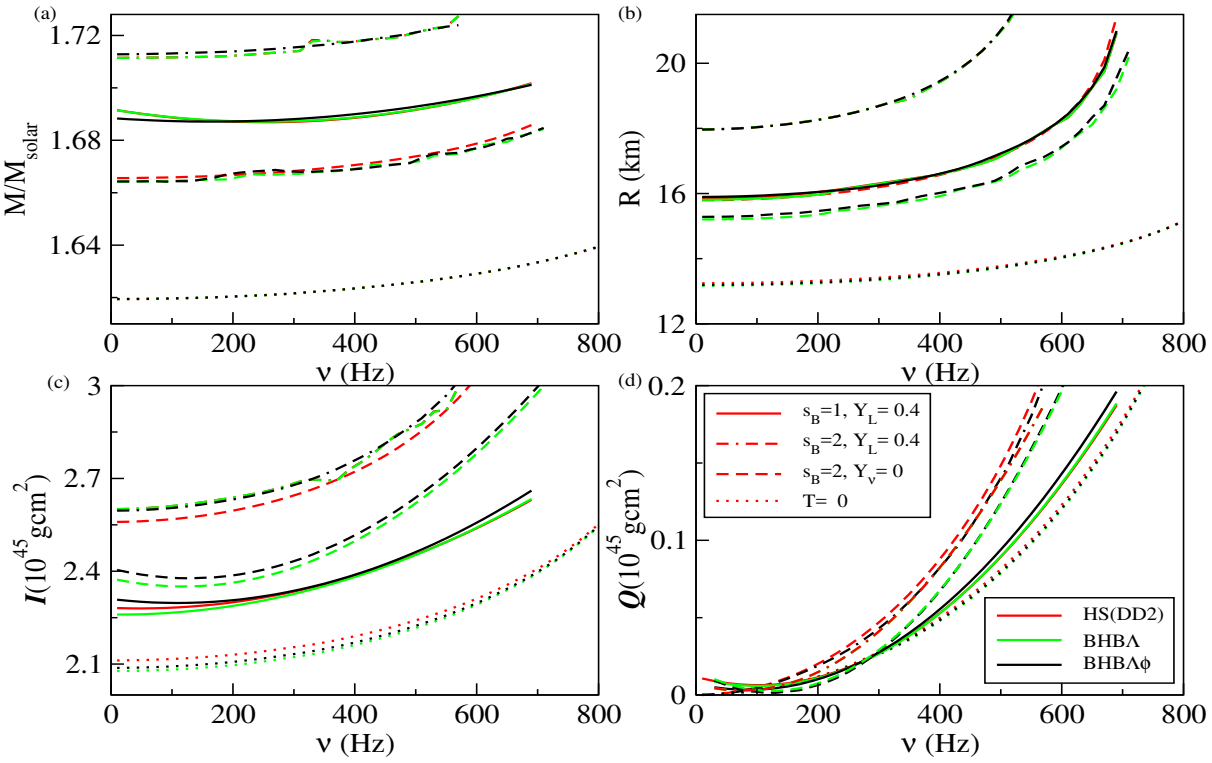

FIGURE 4.4: M, R, I and Q of a star evolving according to Sec. 4.2 are plotted in (a), (b), (c) and (d) respectively as function of rotation frequency. All plots refer to a star with fixed baryonic mass M_B=1.8M_{solar}.

gravitational collapse, neutrino-trapped PNS rotates deferentially. As it settles into β-equilibrium, viscosity dampens the non-uniformity in rotation. We consider an idealized scenario of uniform and rigid rotation about an axisymmetric axis which represents an approximation to the actual rotational state of a hot NS. We use numerical library LORENE to report our results for isentropic rotating NSs [97]. For representative purpose, let us consider a star with baryonic mass M_B=1.8 M_{solar} and follow its different properties such as M, R, I and Q. In Fig. 4.4, these quantities are plotted as a function of rotational frequency for stages I-IV, upto the corresponding Kepler limit. All the quantities are observed to increase monotonically with rotation. This nature was noted in earlier work also [112]. We have checked the stability of the stellar configurations as well. For the rigidly rotating stars with a constant total entropy $S = s_B M_B$, the stability condition is given by $\left(\frac{\partial J}{\partial n_B}\right)_{M_B,S} < 0$. J for all the cases considered here satisfies this condition upon varying the central baryon number density until they become unstable at extremal points [76]. The Kepler limit for a cold-catalysed star with baryon mass of M_B=1.8M_{solar} is 935 Hz, while for the newly

born star it is much less i.e. $\sim$ 703 Hz. Initially the PNS is rotating at a lower frequency, only to reach a higher rotation rate as it contracts and cools down to a cold catalyzed β-equilibrated NS. This can be attributed to the conservation of angular momentum (J=$I\Omega$), which restricts the PNS with large I to rotate slowly. Interestingly, as the PNS attains a higher entropy in the immediate step of evolution with $s_B = 2$ and $Y_L = 0.4$, it has to slow its rotation rate as this star can only withstand a mass-shedding frequency limit of $\sim$ 577 Hz. However, it can increase its rotation rate in the later stages of evolution as is evident from Fig. 4.4. The Kepler limit for all the EoSs in different evolution stages are given in Table 4.3. The gravitational mass remains almost independent of EoS in all the evolutionary stages. We notice an EoS-dependent spread in radii of the stars. This spread is widest for the intermediate stages, but not so explicit for initial and final stages. This is also reflected in the plots for I and Q versus frequency. Their values differ with their constituents for the higher entropy stages due to the differences in the radii. Both I and Q are less for the cold stars compared to the earlier stages.

We tabulate the global structural properties of both non-rotating and maximally rotating PNS for a fixed baryonic mass $M_B = 1.8 M_{solar}$ in Table 4.3. We can see that central density decreases from stages I to III for HS(DD2) EoS and then increases after the star attains β-equilibrium for both static and Keplerian scenarios. However, for the BHBΛ and BHB$\Lambda\phi$ EoSs, the central density starts increasing after deleptonization i.e. from stage III onwards. This can be explained in the following way. As the neutrinos carry away most of the binding energy of the system, after deleptonization, the star contracts and as a result the central density increases for both non rotating and rotating stars. The angular frequency increases for the rotating star thereby increasing the Kepler frequency. Emergence of hyperons in these two EoSs leads to greater neutrino emission resulting in an early contraction. In all stages, the central density for the Keplerian star is always lesser than their static counterparts for all the EoSs considered.

The gravitational mass and radius increase from stage I to stage II due to increase in thermal pressure, but decrease in the subsequent stages. This can be attributed to the loss of neutrino pressure from stage II to III and drop in thermal pressure from stage III to IV. This behavior is observed for both non-rotating and Keplerian cases and also for all EoSs. The values of M and R in the Table 4.3 agree with the results of Fig. 4.4. The angular momentum corresponding the Kepler limit changes the same way as the Kepler frequency already discussed in connection with Fig. 4.4. Finally, we also see the value of the ratio of rotational energy to gravitational energy ($|\mathcal{T}/W|$) steadily increasing from 0.051 to 0.115 during the evolutionary stages, with the exception in stage II. However, these values are rather insensitive to the choice of EoS. This shows the increase in the rotational kinetic energy which leads to rise in ellipticity as is evident from Table 4.3. Interestingly, the change in ellipticity is also independent of EoS. Similarly we have calculated the same set of quantities for a star with fixed baryonic mass $M_B = 2.2 M_{solar}$ and they are listed in Table 4.4. The results are qualitatively similar to those of baryonic mass $M_B = 1.8 M_{solar}$. These results are consistent with those found in earlier studies [123]. In Table

TABLE 4.3: Properties of non-rotating and rotating PNSs at the limiting frequency, for a fixed baryonic mass $M_B = 1.8\ M_{solar}$. The parameters in the table are: central baryon number density ($n_{\rm B}$), gravitational mass (M), circumferential equatorial radius ($R_{\rm eq}$), Kepler frequency ($\nu_{\rm K}$), angular momentum (J), polar to equatorial axis ratio (r_p/r_{eq}) and the rotation parameter ($|\mathcal{T}/W|$).

EoS	PNS stages	$\nu = 0$			$\nu = \nu_{\rm K}$						
		$n_{\rm B}$ [fm^{-3}]	M [M_{solar}]	$R_{\rm eq}$ [km]	$n_{\rm B}$ [fm^{-3}]	M [M_{solar}]	$R_{\rm eq}$ [km]	$\nu_{\rm K}$ [Hz]	J [GM^2_{solar}/c]	r_p/r_{eq}	$\lvert\mathcal{T}/W\rvert$
HS(DD2)	s_B=1, Y_L=0.4	0.388	1.690	15.857	0.353	1.703	22.529	703	1.388	0.612	0.054
	s_B=2, Y_L=0.4	0.346	1.711	17.969	0.322	1.723	25.909	577	1.244	0.623	0.042
	s_B=2, Y_ν=0	0.337	1.668	15.864	0.287	1.687	22.721	696	1.674	0.598	0.076
	T= 0	0.386	1.619	13.246	0.331	1.652	18.551	935	1.957	0.558	0.115
BHBΛ	s_B=1, Y_L=0.4	0.404	1.690	15.807	0.353	1.703	22.518	703	1.390	0.613	0.054
	s_B=2, Y_L=0.4	0.346	1.711	17.970	0.322	1.724	25.909	577	1.245	0.623	0.042
	s_B=2, Y_ν=0	0.409	1.664	15.205	0.333	1.682	22.042	726	1.629	0.599	0.074
	T= 0	0.436	1.619	13.165	0.332	1.652	18.636	935	1.957	0.555	0.115
BHBΛϕ	s_B=1, Y_L=0.4	0.394	1.687	15.894	0.354	1.699	22.553	702	1.357	0.615	0.054
	s_B=2, Y_L=0.4	0.347	1.713	17.964	0.322	1.723	25.893	576	1.242	0.625	0.042
	s_B=2, Y_ν=0	0.386	1.664	15.283	0.326	1.686	22.167	724	1.633	0.597	0.074
	T= 0	0.419	1.619	13.191	0.332	1.652	18.656	935	1.958	0.555	0.115

TABLE 4.4: Same as Table 4.3 but for a fixed baryonic mass $M_B = 2.2 M_{solar}$.

EoS	PNS stages	$\nu = 0$			$\nu = \nu_{\rm K}$						
		$n_{\rm B}$ [fm^{-3}]	M [M_{solar}]	$R_{\rm eq}$ [km]	$n_{\rm B}$ [fm^{-3}]	M [M_{solar}]	$R_{\rm eq}$ [km]	$\nu_{\rm K}$ [Hz]	J [GM^2_{solar}/c]	r_p/r_{eq}	$\lvert\mathcal{T}/W\rvert$
HS(DD2)	s_B=1, Y_L=0.4	0.464	2.002	14.90	0.410	2.034	20.869	851	2.094	0.610	0.066
	s_B=2, Y_L=0.4	0.436	2.04	16.244	0.389	2.065	23.184	735	1.958	0.616	0.055
	s_B=2, Y_ν=0	0.405	1.993	15.177	0.339	2.021	21.428	817	2.433	0.594	0.085
	T= 0	0.453	1.930	13.192	0.371	1.982	18.491	1028	2.815	0.550	0.124
BHBΛ	s_B=1, Y_L=0.4	0.558	1.993	14.451	0.447	2.035	20.784	862	2.102	0.603	0.067
	s_B=2, Y_L=0.4	0.522	2.042	15.987	0.389	2.064	23.159	735	1.955	0.617	0.054
	s_B=2, Y_ν=0	0.669	1.982	13.649	0.437	2.02	20.409	885	2.373	0.592	0.084
	T= 0	0.726	1.924	12.387	0.404	1.983	18.409	1037	2.82	0.551	0.124
BHBΛϕ	s_B=1, Y_L=0.4	0.543	2.001	14.494	0.442	2.036	20.722	860	2.087	0.608	0.066
	s_B=2, Y_L=0.4	0.501	2.042	16.035	0.388	2.064	23.331	735	1.96	0.611	0.055
	s_B=2, Y_ν=0	0.545	1.981	14.128	0.424	2.018	20.554	874	2.389	0.593	0.085
	T= 0	0.573	1.929	12.815	0.394	1.982	18.483	1034	2.82	0.549	0.124

I and II of Ref. [123], the changes in central density, M and R with increasing time steps are listed, while we report our results for different ad hoc stages in Table III and IV. However, we use isentropic profiles unlike theirs. In Figs. 4.5 and 4.6, we explore the universality relations for normalized I ($\bar{I}$) with HS(DD2), BHBΛ and BHBΛϕ EoSs corresponding to the four stages of PNS with respect to $\mathcal{C}$. I is normalized to M^3 and MR^2 respectively in the two figures. Both the figures have three panels indicating three different spin frequencies from left to right i.e. 100, 300 and 500 Hz. We find the $\bar{I}$ lines are almost independent of the composition of the star corresponding to each PNS stage. But the lines corresponding to different temperature and lepton fraction are distinctly separated. This pattern is seen for both types of normalization and also for a particular frequency. Therefore, we might attribute this behavior to the combined effects of temperature and lepton fraction.

Next, we try to quantify the deviations by comparing our calculated values of $\bar{I}$, plotted in

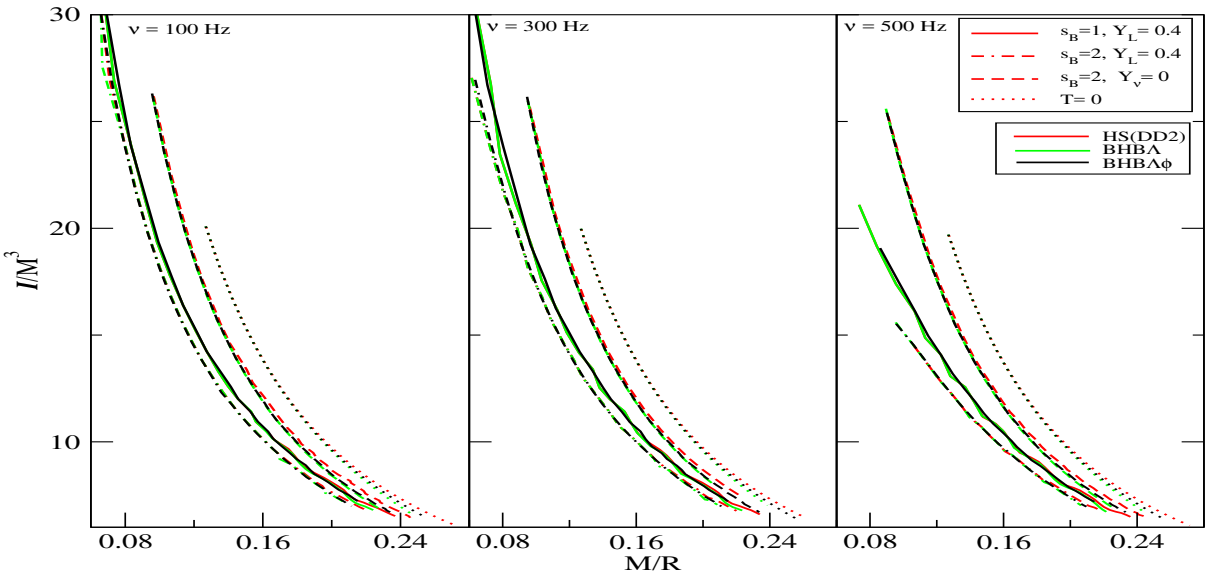

FIGURE 4.5: Normalized $I(I/M^3)$ with $\mathcal{C}$ for a star rotating at different frequencies as it evolves from PNS to NS.

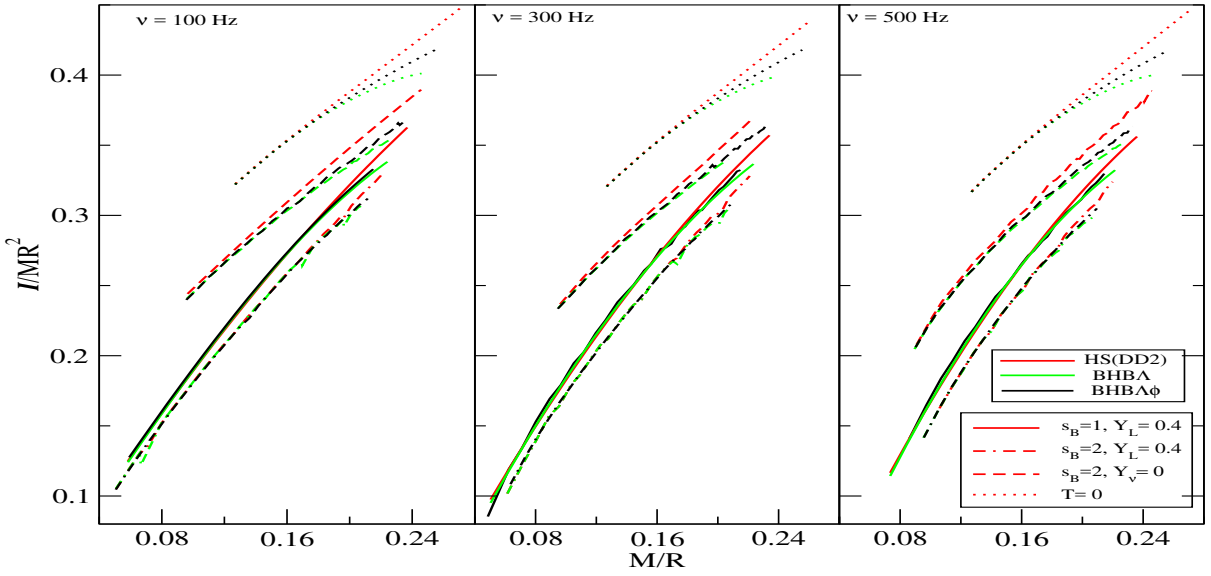

FIGURE 4.6: Normalized $I(I/MR^2)$ variation with $\mathcal{C}$ for same cases as in Fig.4.5.

Fig. 4.5 and Fig. 4.6, for a star rotating at a fixed frequency of 100 Hz with the ones we get from the fitting functions given by Breu and Rezzolla [59]. The fitting relations for $\bar{I}$ are,

$$\bar{I}_{fit} := \frac{I}{MR^2} = a_0 + a_1\mathcal{C} + a_4\mathcal{C}^4 \tag{4.1}$$

and

$$\bar{I}_{fit} := \frac{I}{M^3} = \bar{a}_1\mathcal{C}^{-1} + \bar{a}_2\mathcal{C}^{-2} + \bar{a}_3\mathcal{C}^{-3} + \bar{a}_4\mathcal{C}^{-4}. \tag{4.2}$$

The values of the constants are $a_0 = 0.244$, $a_1 = 0.638$, $a_4 = 3.202$, $\bar{a}_1 = 8.134 \times 10^{-1}$, $\bar{a}_2 = 2.101 \times 10^{-1}$, $\bar{a}_3 = 3.175 \times 10^{-3}$, and $\bar{a}_4 = -2.717 \times 10^{-4}$ [59]. We use our $\bar{I}$ data and

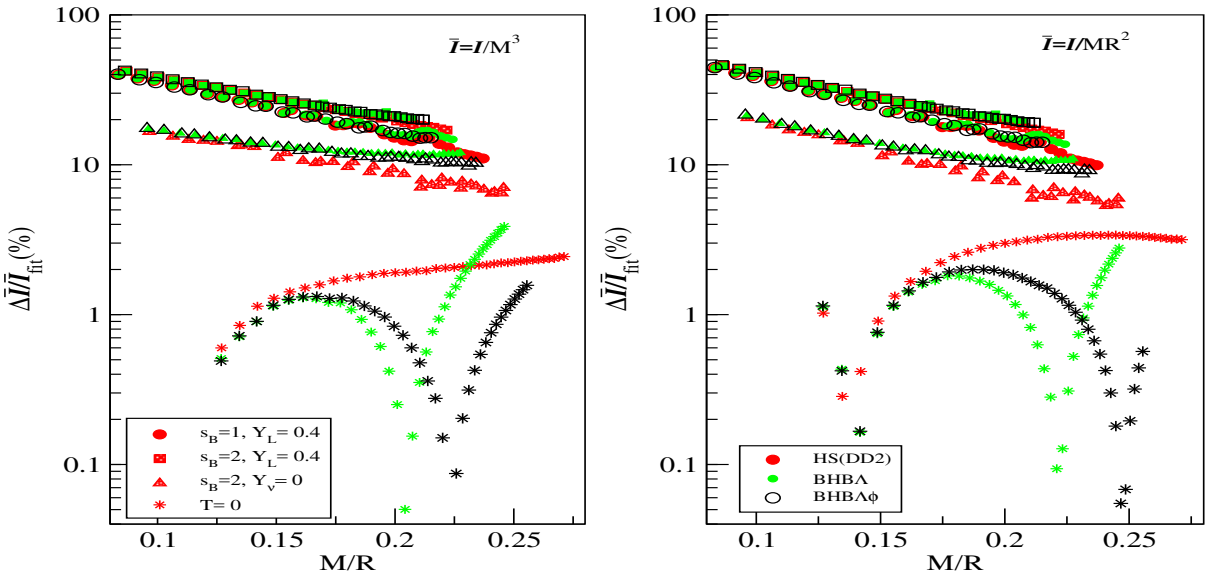

FIGURE 4.7: Relative differences ($\Delta\bar{I}/\bar{I_{fit}} = |\bar{I} - \bar{I_{fit}}|/\bar{I_{fit}}$) variation with compactness for a PNS rotating with frequency 100 Hz ; in the left panel $\bar{I} = I/M^3$ and in the right panel $\bar{I} = I/MR^2$.

compare those with the values ($\bar{I}_{fit}$) obtained from above equations. We plot their relative differences $\Delta\bar{I}/\bar{I}_{fit} = |\bar{I} - \bar{I}_{fit}|/\bar{I}_{fit}$ in Fig. 4.7. We find very high deviations ($\sim 40 - 50\%$), particularly in case of high entropy and lepton rich EoS for both the normalization. This deviation is more evident for less compact stars. The deviation becomes smaller i.e. around $\sim 10\%$ for the case of $s_B = 2$, $Y_\nu = 0$. However, the deviations are always the least, i.e. below $\sim 2 - 3\%$, for each EoS at T=0. Similar features have been observed for stars rotating at 300 and 500 Hz.

Next, we consider the stages of a rotating PNS at fixed M_B 1.8 M_{solar} and 2.2 M_{solar}. At each stage, we measure the deviations from universality as done by Martinon et al. in the context of I-love-Q relations [112]. Again we use the aforementioned fitting functions and fitting factors for $\bar{I}$. We plot these results in Fig. 4.8 for a star rotating at a very low frequency of 5 Hz. As evident from Tables 4.3 and 4.4, this is less than 1% of the average Kepler limits. Here, we have used different symbols to distinguish the four evolutionary stages and different color schemes for the three chosen EoSs. For the $M_B = 1.8$ M_{solar} star, we don't find the deviations to be sensitive to the composition of the star except for the cold catalyzed one.

The values of relative differences start with $\sim 22\%$ for stage I, followed by $\sim 30\%$ and $\sim 12\%$ for stage II and III respectively. Finally, when it reaches the cold catalyzed stage, the deviation falls down to $\sim 2\%$. Thus, we conclude that the $\bar{I} - \mathcal{C}$ relation is broken at the early stages of the life of a PNS, but the universality is restored once the star becomes cold and attains beta stability. Our result is consistent with the earlier findings of Martinon et al. regarding the $\bar{I} - \bar{Q}$ relation [112]. They have used the entropy and lepton fraction profiles from simulation results of evolving PNS at different time steps. On the other hand, Marques et. al [76] have used arbitrary profile for entropy but not considered any neutrino-trapped EoS in their calculations.

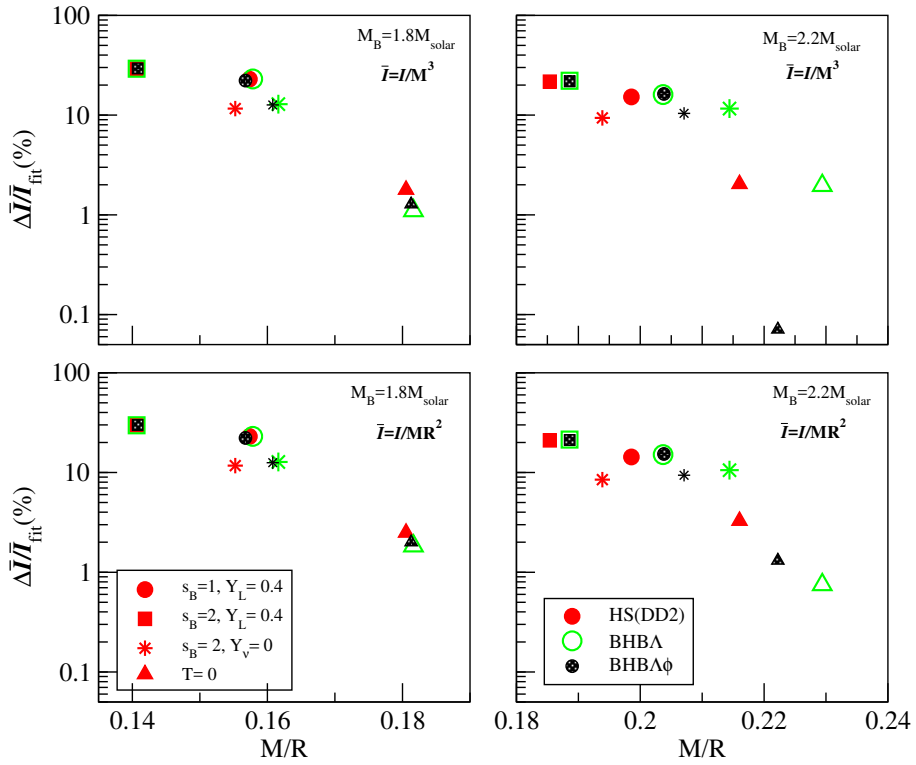

FIGURE 4.8: Same as Fig. 4.7 but for a PNS rotating with frequency 5 Hz; in the upper panels $\bar{I} = I/M^3$, whereas in the lower panel $\bar{I} = I/MR^2$. The two columns are for fixed baryon mass $M_B = 1.8 M_{solar}$ and $2.2 M_{solar}$.

We take constant entropy per baryon throughout the star. Our lepton-rich matter at stages I and II contains trapped neutrinos. The deviations in the universality can be due to the combined effect of neutrino and thermal pressure. For the $M_B = 2.2$ M_{solar} star, the situation is almost similar. The only difference is that there is a deviation for different EoSs in the cold NS stage also. Nevertheless, they remain below $\sim 2\%$. Thus the conclusion remains the same.

4.4 Summary

In the present work, we use the ad hoc profile which qualitatively represents the different evolutionary stages [71, 48] and study the properties of a massive PNS containing Λ hyperons. This is done using EoS within the framework of RMF model with density dependent couplings. The model uses the parameters which are consistent with several nuclear physics experimental data and astrophysical observational data. We construct the EoS for $s_B = 1$ and $Y_L = 0.4$; $s_B = 2$ and $Y_L = 0.4$; $s_B = 2$ and $Y_\nu = 0$; cold-catalyzed for both nucleonic and hyperonic models. The initial stages I and II contain electron-type neutrinos trapped in the PNS core. We calculate the M-R sequence for static star with those EoSs. We find a clear effect of temperature on the size of the stars. The hotter the star, the larger is the radius. Although we don't find much difference between the hyperonic stars with and without ϕ meson, the difference between

hyperonic and nucleon-only stars is quite visible in this model. We also note that the properties of less compact stars are governed mostly by their temperature and lepton content. Several global properties of PNS are studied using those EoSs from static to maximally rotating configurations for fixed baryon masses of 1.8 and 2.2 M_{solar}. We see qualitative similarities for both the cases.

Another important finding of our studies is the deviation from $\bar{I} - \mathcal{C}$ universal relations for very hot and neutrino-rich stars. The temperature dependence in the $\bar{I} - \mathcal{C}$ relations was carried out here for the first time. We take a slowly rotating star and measure the deviations for each of the stages. We have seen with the arbitrary profile, the deviation is maximal in the first three stages, while universality is satisfied at cold catalyzed stage. Therefore, applying any universal relation to make a connection between a quantity measured before merger (e.g. tidal deformability κ_2^T) and another quantity after merger (e.g. peak frequency f_2) requires utmost caution.

Chapter 5

Role of antikaon condensation on the universality relations of hot and rapidly rotating neutron stars

5.1 Introduction

Many authors have shown that the antikaon condensates replace the leptons suitably in the high density core of NS and soften the EoSs [44, 46, 48]. In this chapter, we aim to study the role of K^- condensates in the interior of stars. We investigate the properties of cold as well as hot isentropic stars with both static and rotating configurations. We consider two EoSs with different compositions, one with nucleons only (np) and other with nucleons, thermal kaons and antikaon condensates (npK) [74]. At low densities, the NS contains n, p and leptons. At higher densities, the threshold condition; $\mu_{K^-} = \mu_n - \mu_p = \mu_e$ is satisfied and K^-s appear and replace the leptons in the system. We construct the EoSs using a RMF model with density dependent couplings. The density-dependence of meson-baryon couplings [45, 63, 64, 81] give rise to the rearrangement term in the pressure term, that accounts for the energy-momentum conservation and thermodynamic consistency of the system [45]. The antikaon condensates are treated at the same footing as that of nucleons. However, the kaon-nucleon couplings are not density dependent. These condensates do not contribute to pressure, but implicitly change the rearrangement term via the interacting meson fields. These are discussed in Section 2.2 of Chapter 2.

NSs are relativistic objects and computations of their structure should be carried out in a GR framework. We solve the TOV equations to study various properties of static star and use LORENE library to study rotating hot star. The rotation causes deformation in the spherically symmetric static star, that can be quantified by the deformation parameters like quadrupole moment and tidal deformability. For a fixed baryonic mass star, we study the variation of M, R,

TABLE 5.1: Maximum gravitational mass (in M_{solar}) and the corresponding radius (in km) of static stars. The values in the parenthesis are for the npK ($U_{\bar{K}}$ =-140 MeV) matter and outside the parenthesis are for nucleons only matter.

Entropy per baryon	M (M_{solar}) np[npK]	R (km) np[npK]	$n_C(fm^{-3})$ np[npK]	Threshold for K^- condensates (fm^{-3})
T=0	2.42[2.16]	11.87[12.01]	0.851[0.881]	0.416
s_B=1	2.42[2.16]	12.07[12.10]	0.836[0.881]	0.449
s_B=2	2.43[2.22]	12.74[13.12]	0.791[0.796]	0.535
s_B=3	2.46[2.30]	14.20[14.83]	0.708[0.702]	0.674

I, Q and J as the star spins from static to its Kepler limit. We explore the universal relations of the NSs at fixed frequency with varying enthalpy. We calculate normalized I ($\overline{I}$) and normalized Q ($\overline{Q}$) where $\overline{I}$=I/M^3 and $\overline{Q}$=QM$/J^2$. We further check the validity of I-love-Q universality for the NS with our proposed EoSs assuming an isentropic profile of the star.

We have discussed all the structural analysis for NSs in Chapter 2 and calculated mass, angular momentum and quadrupole moment etc. We, then calculate the tidal deformability of an isolated NS, $\lambda = -\frac{Q_{ij}}{E_{ij}}$, where Q_{ij} is the induced quadrupole moment of the NS under the influence of a static external tidal field E_{ij}. The dimensionless, $l = 2$, electric-type love number, k_2 is related to tidal deformability by $\lambda = \frac{2}{3}k_2R^5$, where R is the radius of the NS. They can be calculated in general relativity together with TOV equations for a static NS EoS, following the prescription of Hinderer et. al [124, 125].

5.2 Result

Our choice of EoSs are np (nucleons only) and npK (neutron, proton and antikaon condensates for optical potential depth $U_{\bar{K}}$= -140 MeV). We have used different colors for the EoSs (red for np and blue for npK) and different line styles for different values of entropy per baryon in the units of Boltzmann constant k_B i.e. T=0 in solid, s_B=1 in dash dot dashed, s_B=2 in dashed and s_B=3 in dotted. We plot energy density profile in Fig. 5.1(a) for the cold star as well as the isentropic star at different s_B (1, 2, 3). We observe more-or-less similar profiles for both the np and npK EoS for a particular entropy per baryon. The appearance of antikaon condensates lowers the total energy of the system. Since antikaons form s-wave Bose condensates, they do not directly contribute to the pressure. On the other hand, as they replace the negatively charged electrons, the drop in lepton pressure results in a softer EoS. However, an EoS-dependence is not so significant towards the surface of the NS, where the density is less and the antikaon condensates do not appear at all. Also, hotter the star, larger is its radius due to increasing thermal pressure.

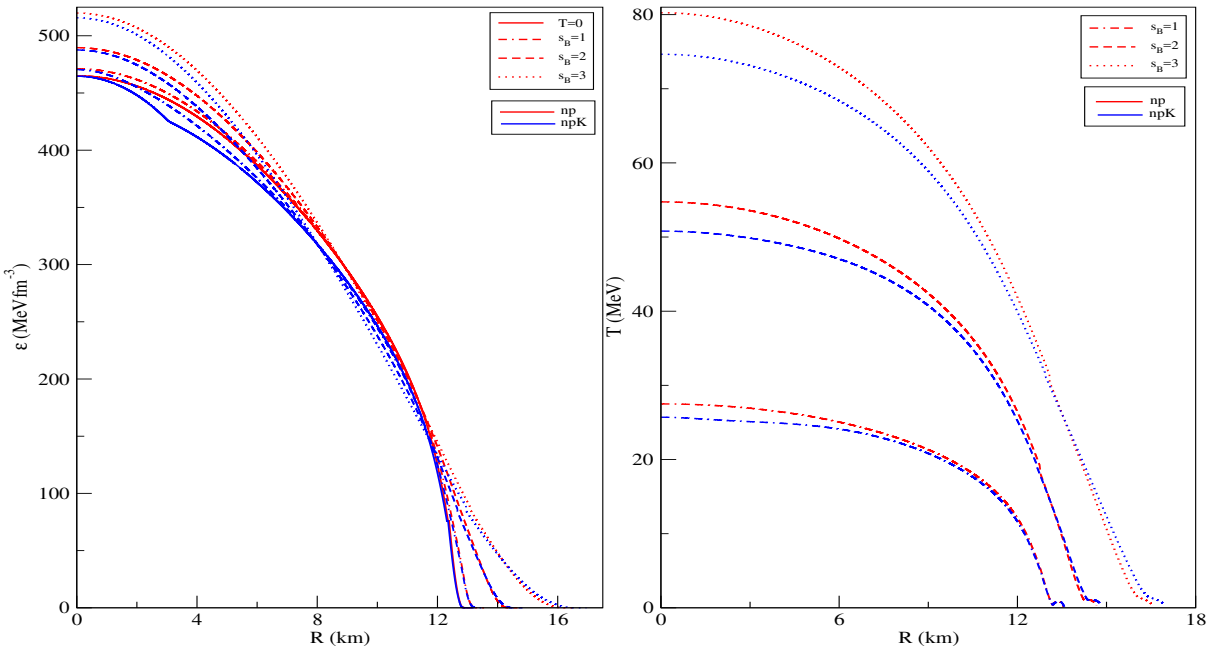

FIGURE 5.1: (a) Energy density-Radius profile for non rotating stars with different compositions. (b) Temperature-Radius profile for non rotating stars.

Fig. 5.1(b) shows temperature variation with radius. We notice higher value of core temperature at higher s_B, the temperature falls off near the surface of the NS. As the presence of antikaons effectively lowers the energy of the NS, its temperature also comes down. This is quite expected. We can see the rise in temperature from $\sim 26(28)$ to $\sim 75(80)$ for npK(np) EoS as the entropy per baryon goes up from 1 to 3.

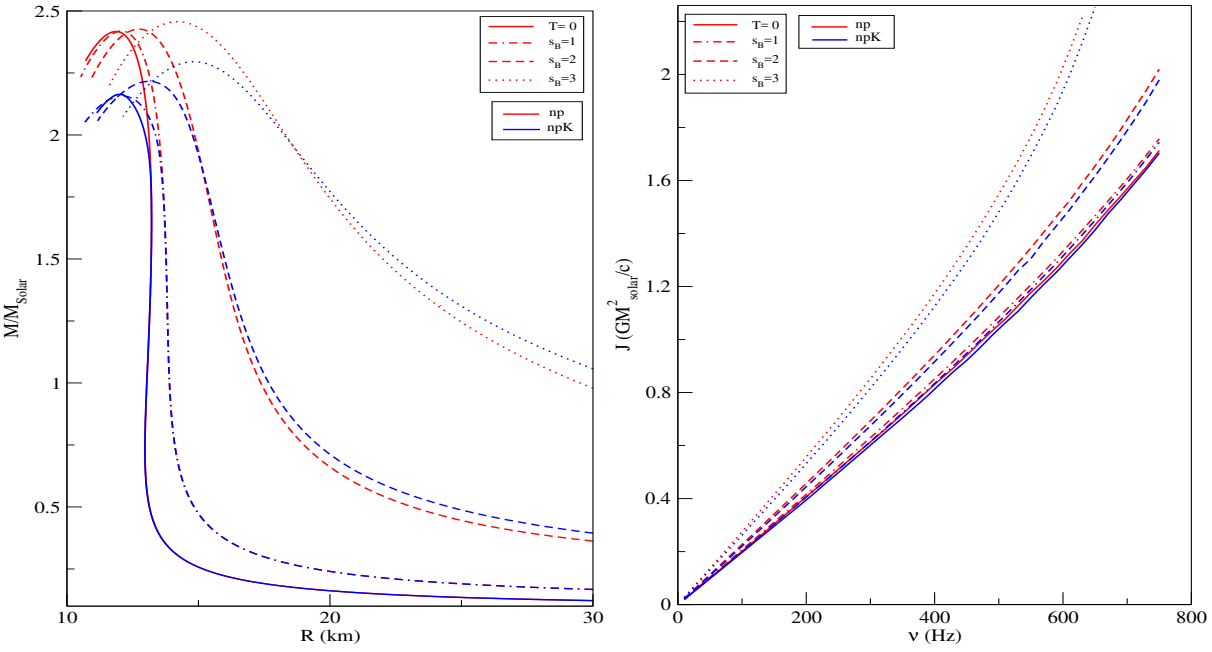

FIGURE 5.2: (a) Mass-Radius profile for non rotating stars with different compositions. (b) Angular momentum as function of frequency for a star with fixed baryonic mass $2.3M_{solar}$.

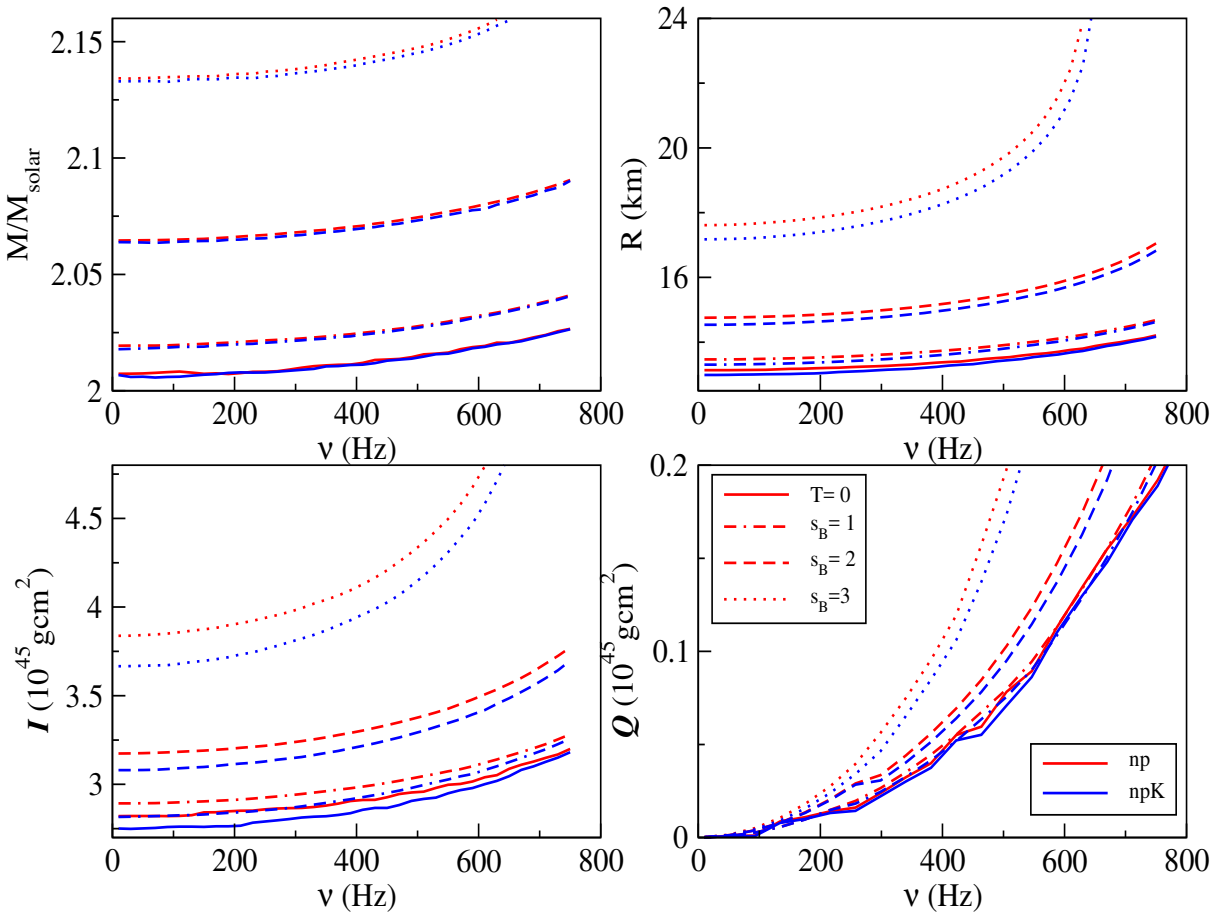

FIGURE 5.3: M, R, I and Q as function of frequency for a star of fixed baryonic mass $2.3M_{solar}$.

The mass-radius profile for static, β-equilibrated and charge neutral with different compositions and s_B are displayed in Fig. 5.2(a). The thermal pressure can support more mass. Therefore, maximum mass of the star increases with increase in s_B. The maximum mass and corresponding radius for these static stars are noted in Table 5.1. The maximum gravitational mass of np matter is $> 2.42M_{solar}$, whereas for npK matter it lies between 2.16 to $2.30M_{solar}$ as evident from Table 5.1. Our model clearly satisfies the $2M_{solar}$ observation [31, 32, 33]. The corresponding central density and the threshold number density of K^- condensates are also listed in Table 5.1. The central density of the NS with the condensates is slightly less than that of nucleons-only star, due to larger size of the former. However, there is an inherent uncertainty with the radius values for NS at finite temperature as the surface pressure never really goes to zero.

Next, we consider effect of rotation on NS in Fig. 5.2(b). Here also we use similar color scheme for EoS and line styles for s_B value as followed in Fig. 5.1. An NS with a fixed baryonic mass of $\sim 2.3M_{solar}$ contains an appreciable fraction of K^- condensates. Therefore, we choose a fixed baryonic mass of $2.3M_{solar}$ to study the role of antikaon condensates on the rotating star. In Fig. 5.2(b), we plot J with frequency for the rotating star. Each curve terminates at its Kepler limit (< 800Hz). Incidentally, the fastest known pulsar, PSR J1748-2446ad rotates with a frequency

of 716 Hz. J is, as expected, more for an NS spinning at higher frequency. The cold NSs at any particular spin frequency have same angular momentum for the np and npK EoS. As the NS gets hotter, it can support more mass; its size also grows. At a particular spin frequency and entropy, gravitational mass does not change much with the constituents. However, the radius changes, specially at higher s_B, as we will see in Fig. 5.3. This explains the higher J value at larger s_B for np EoS compared to npK EoS.

We calculate some other properties, M, R, I, and Q of the NS, with fixed baryon mass of $2.3M_{solar}$ starting from a static configuration up to the mass-shedding frequency. It can be seen that all the parameters are monotonically increasing with frequency. This was noted for other EoSs in earlier work also [112, 126]. The gravitational mass is almost independent of the constituent matter. However, the radius value differs for np and npK EoS, especially for the highest s_B. This affects the EoS-dependence of I and Q. Both I and Q values are nearly close for np and npK cold EoS. However, for higher s_B a marked difference is visible. The variation is maximum for the highest s_B. This can be attributed to the thermal pressure which is quite large for the hadrons and leptons at higher s_B, and always nil for the condensates. Hence the increase in NS size is more for the np matter compared to the npK one.

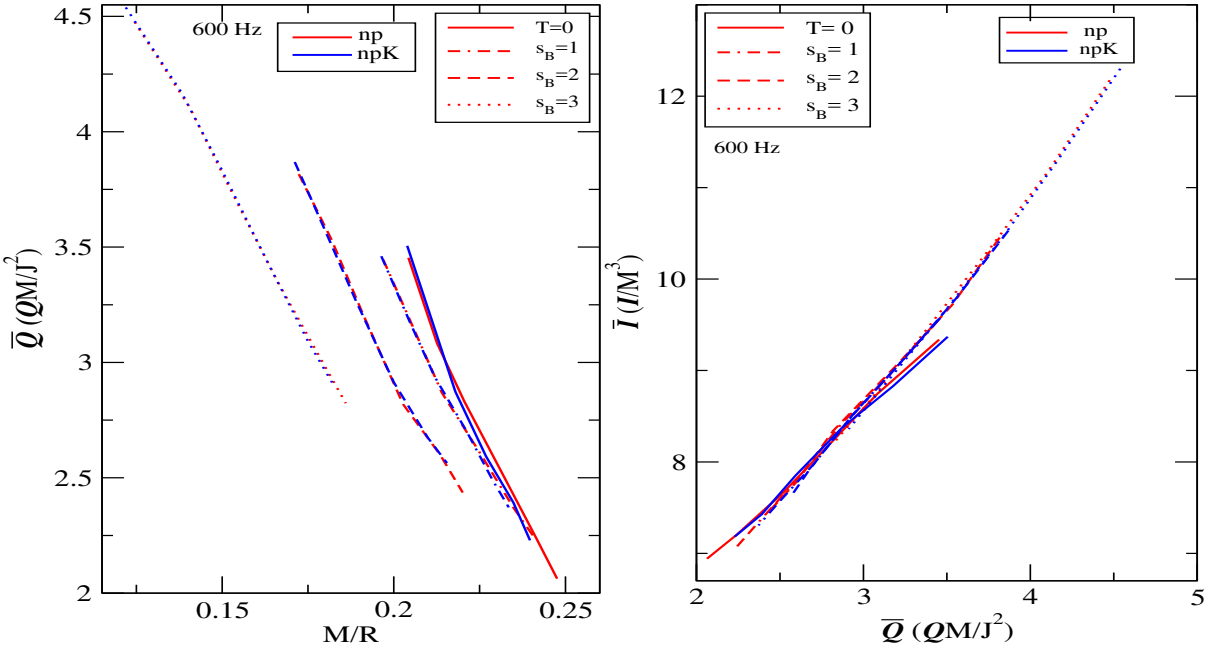

FIGURE 5.4: (a) Normalized quadrupole moment ($\bar{Q}$) versus $\mathcal{C}$ (b) Dimensionless moment of inertia ($\bar{I}$) variation with dimensionless quadrupole moment ($\bar{Q}$) for both the EoSs at a frequency of 600 Hz.

Now we move on to the investigation on universal relations. The normalized Q ($\bar{Q} = QM/J^2$) versus $\mathcal{C}$ is plotted in Fig. 5.4(a) for a star rotating at a frequency of 600Hz. $\bar{Q}$ is quite independent of the chosen np or npK EoS. The star with higher s_B is more compact and, its Q

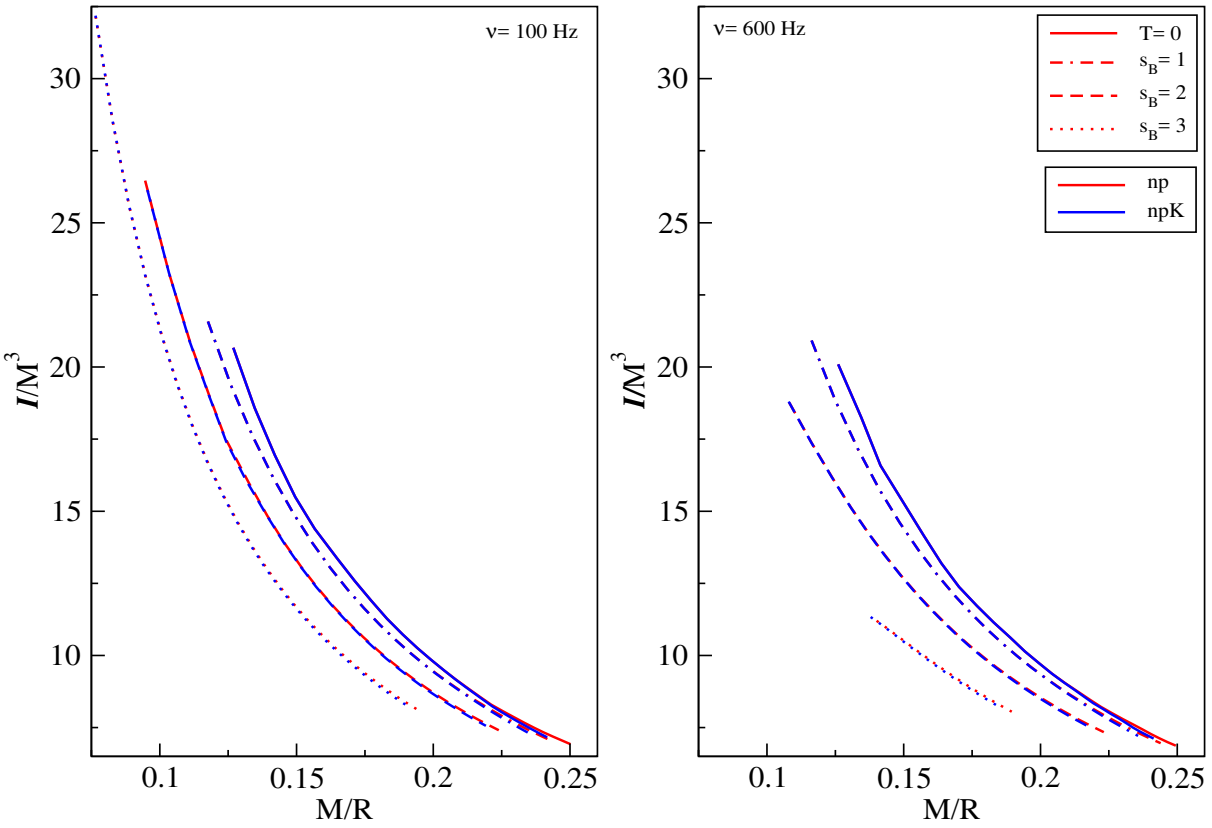

FIGURE 5.5: Dimensionless $I(I/M^3)$ as function of $\mathcal{C}$. Left plot shows the curves for frequency 100 Hz where as right side plot contains the curves for 600 Hz frequency.

value is higher. In Fig. 5.4(b) we show the variation of normalized I ($\bar{I} = I/M^3$) with normalized Q for a frequency of 600 Hz, which is almost independent of the constituents.

Next, we consider the star at two frequencies, i) rotating comparatively slowly at a frequency of 100 Hz and ii) rotating rather fast at a frequency of 600 Hz. Fig. 5.5 shows the variation of dimensionless I ($\bar{I}$)= I/M^3 with $\mathcal{C}$. Left plot shows the relation for the frequency 100 Hz where as right side plot is for 600 Hz. We observe universality at lower $\mathcal{C}$. A very slight deviation due to EoS is noticed at high $\mathcal{C}$, which is not so prominent. We show the variation of dimensionless I ($\bar{I}$)= I/MR^2 with $\mathcal{C}$ in Fig. 5.6. The plots are for the frequency 100 and 600 Hz respectively. Here also we notice universality at low $\mathcal{C}$. Slight deviation in universality relation occur at high $\mathcal{C}$ as was noticed in Fig. 5.5.

The variation of tidal love number (k_2) with $\mathcal{C}$ is shown in Fig. 5.7(a). The love number is least for higher entropy stars i.e. the thermal energy resist the deformation. The cold NS can however, be deformed easily as evident from Fig. 5.7(a). It increases upto a maximum value, then drop monotonically at higher $\mathcal{C}$. At lower $\mathcal{C}$, for a fixed s_B with both np and npK EoSs, k_2 is same. However their differences become significant at higher $\mathcal{C}$, where the fraction of antikaons is maximal. In Fig. 5.7(b), we plot the tidal deformability parameter λ with $\mathcal{C}$. The parameter $\lambda = \frac{2}{3}k_2R^5$ represents the degree of deformation of a rotating NS away from sphericity

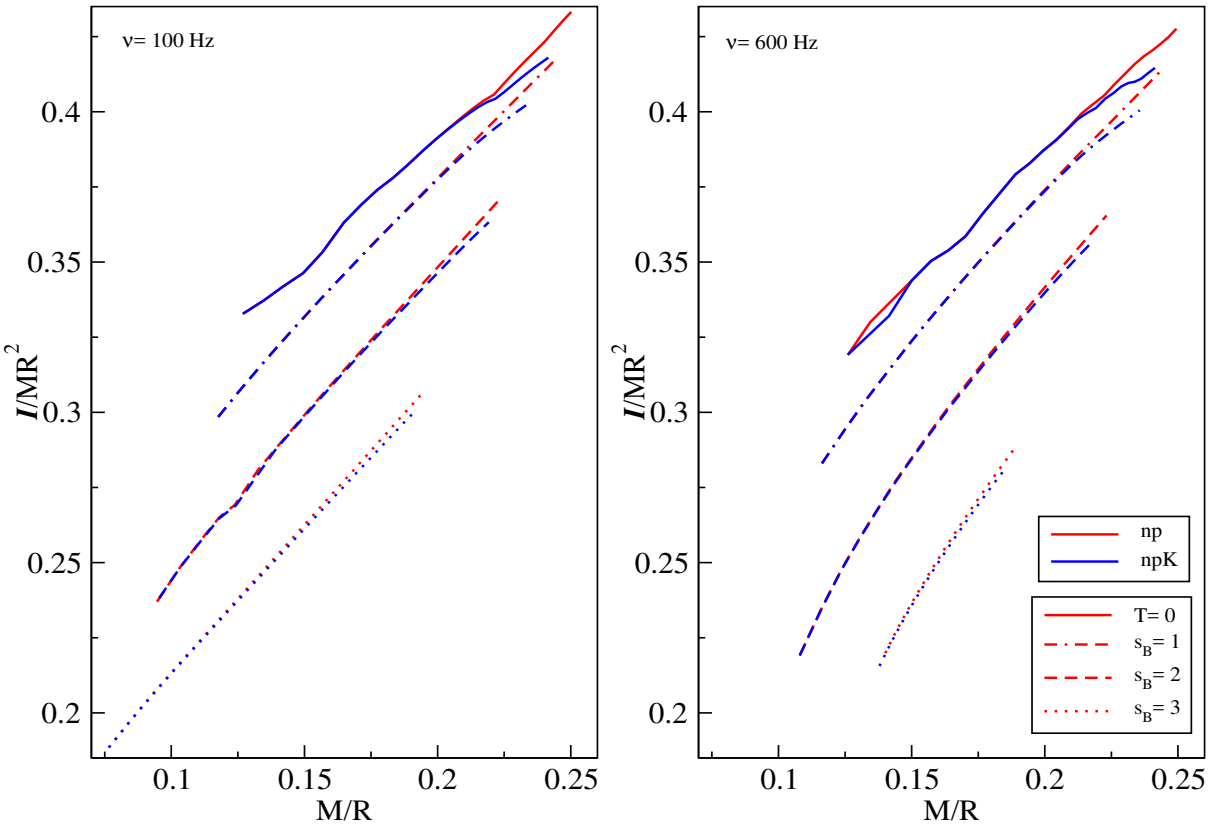

FIGURE 5.6: Dimensionless $I(I/MR^2)$ as function of $\mathcal{C}$. Left plot is for frequency 100 Hz where as right side plot is for 600 Hz frequency.

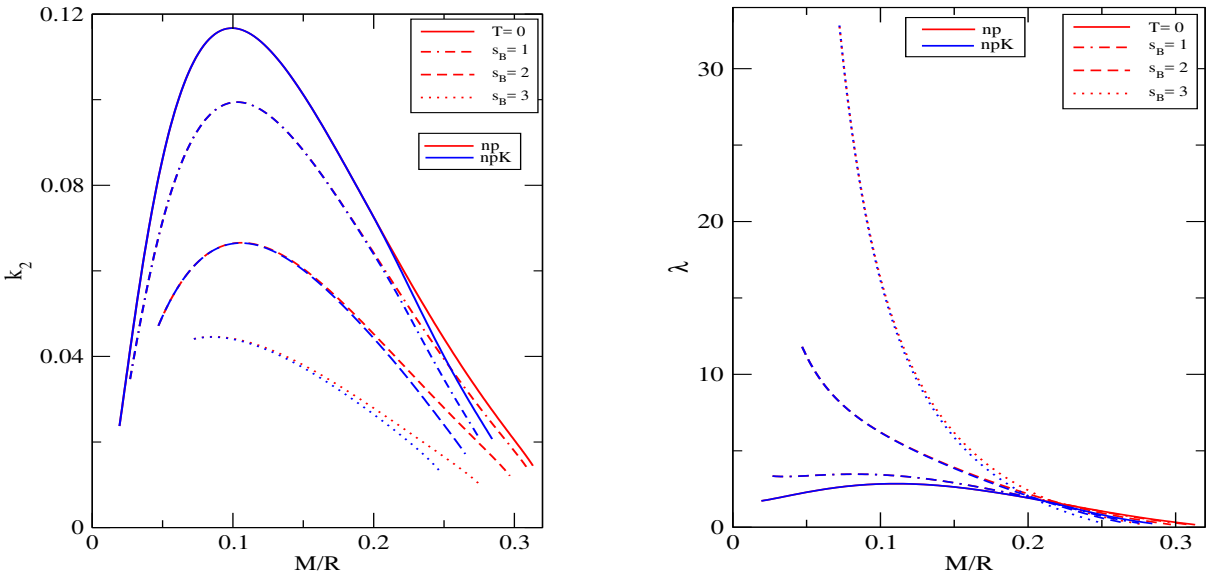

FIGURE 5.7: a) Love number k_2 with $\mathcal{C}$ b) The tidal deformability parameter λ versus $\mathcal{C}$ for np and npK from cold EoS upto $s_B = 3$.

and where k_2 is the dimensionless, $l = 2$, electric-type tidal love number, and R its radius. As $\lambda \propto R^5$, radius calculation is very important. Fortin et. al has shown that the uncertainty in radius calculations can be as high as $\sim 4\%$ unless the core-crust EoSs are obtained from

the same many-body theory [52]. We take the low density part of the EoS from Hempel and Schaffner-Bielich [75], where the interaction among the unbound nucleons are described by the same Lagrangian density as in the high density core and using the density dependent formalism [64, 75]. We notice that higher the entropy per baryon, higher is the corresponding λ. However, this difference almost vanishes at higher $\mathcal{C}$. On the other hand, at a fixed s_B, λ is independent of the composition of the star for lower $\mathcal{C}$. At the higher $\mathcal{C}$ region, λ varies considerably for np and npK EoS, finally approaches zero at the black hole limit of $\mathcal{C}$=0.5.

5.3 Discussion and Conclusion

We study various structural properties of NSs, that are closely related to the dynamics and hence the observable properties of pulsars. Two types of EoSs have been used for this purpose, one with nucleons only constituents and other one involves Bose-Einstein condensate of antikaons. These EoSs are formulated by using density dependent nucleon meson couplings in relativistic mean field model. The mass, energy density and temperature profiles of a spherically symmetric static NS are investigated for both the EoSs. These are calculated by solving TOV equations. We have carried out our study for cold EoS as well as for hot EoS at different s_B values.

Then, we study some of the properties of rotating NSs at different s_B values. Here, the calculations are done using LORENE library. We calculate some parameters, like gravitational mass, radius, moment of inertia, quadrupole moment and angular momentum for a NS with fixed baryonic mass ($M_B = 2.3 M_{solar}$), which contains a considerable fraction of antikaon condensates. We observe that all the variables increase with frequency and they have similar nature for both the EoSs. However, their values are noticed to be different for np and npK EoS at higher s_B.

We further calculate I and Q, both dimensionless, for a NS rotating at fixed frequency containing neucleons as well as the antikaon condensates and show their variation with $\mathcal{C}$. Universality is maintained for the latter, as evident from the $\bar{Q}$-$\mathcal{C}$ graph. We use two types of normalization for I. The universality remains intact at lower $\mathcal{C}$ for $\bar{I}$, which deviates slightly for different compositions at high $\mathcal{C}$. We also show $\bar{I} - \bar{Q}$ relation is independent of the chosen constituents for a rapidly rotating NS.

From the love number versus $\mathcal{C}$ plot, we conclude that, it depends on EoS at higher $\mathcal{C}$ and the value is maximum for the cold EoS. This indicates that the thermal pressure counterbalances the deformation due to rotation. Finally, we investigate the correlations between $\mathcal{C}$ and tidal deformability for a single NS, and conclude that it is independent of the chosen np or npK EoS. Also, it is quite high for NS with larger s_B at low $\mathcal{C}$. At higher $\mathcal{C}$, λ does not depend on either EoS or s_B and eventually becomes zero as the NS approaches the compactness of a black hole.

Chapter 6

Summary and Conclusion

In our study, we adopt the traditional meson exchange picture known as relativistic mean field model to study the dense matter relevant to NSs. The interior of the star contains various species of baryon octet, and/or the antikaon condensates in addition to the neutrons, protons and leptons. In this model, baryon-baryon interaction is mediated by the exchange of σ, ω and ρ meson. The model also includes hyperon-hyperon interaction through ϕ mesons. Leptons are treated non-interacting. Antikaon-baryon interaction has been studied in similar fashion as baryon-baryon interaction. Starting from the Lagrangian, we compute the Euler-Lagrange equation to find the equations of motion for the interacting mesons. Imposing the charge neutrality and baryon number conservation constraints, the meson field equations are solved numerically to construct our EoSs. In this model, the meson-nucleon couplings are density dependent and they are adjusted to reproduce properties of symmetric and asymmetric nuclear matter and finite nuclei such as nuclear compressibility, symmetry energy and binding energy at saturation density. The merit of the DD2 model lies in the fact that it is within the experimental nuclear physics constraints, namely the symmetry energy and its slope parameters. Also, this version uses experimental nuclear masses, which is an important modification over the original density dependent model by Typel. Last but not the least the NS observables calculated within DD2 model are consistent with the latest mass observations and tidal deformability results from GW170817.

NSs are hot and lepton-rich at the time of their birth. We call them PNS. During deleptonisation, the neutrinos carry most of the energy and the core temperature drops to 5-10 MeV. Finally, they settle as cold NS. We compute PNS EoS at a constant entropy per baryon where as the NS EoS is computed at zero temperature. The high and low density parts of the EoS are matched in a thermodynamically consistent way. Apart from charge neutrality and baryon conservation, we apply condition of β- equilibrium on the chemical potentials in cold NS. The chemical equilibrium

condition is different for a lepton trapped PNS as they have trapped electron-type neutrinos with lepton fraction of $Y_L = 0.4$.

Once the EoSs are constructed, the structural properties are calculated for both static and rotating star. The line element for a static star is given by the Schwarzchild metric. The structure of the spherically symmetric, static relativistic NS is determined by the TOV equations. On the other hand, the line element for a rotating star has four independent potentials. We consider a circular fluid motion around the rotation axis for rotating star and compute the structural properties of the star for rigid rotation. The global properties of the rotating stars like gravitational mass, radius, I and Q are calculated.

In chapter-3, we study several structural properties and universality relations of rotating, cold NSs with nucleonic (n, p) as well as exotic constituents such as hyperons (Λ, Ξ, Σ) and antikaon condensates. We have considered a range of values for the optical potential of antikaons in nuclear medium, considering the experimental ambiguity. The EoSs are softer for deeper optical potential. We study the static and Kepler mass-radius relations along with fixed angular velocity and fixed rest mass sequence curves. We notice $16 - 20\%$ increase in the maximum mass as we move from static to Kepler rotation for all the EoSs considered. We also calculate the critical mass which is the maximum mass sustainable at a constant angular momentum; beyond this the star becomes unstable. As we plot the normalized critical mass with normalized angular momentum we notice a universality in the stars profiles (i.s a 20% rise in critical mass for all the configurations). Next, I is calculated for various compositions and its variation is studied with respect to mass. We observe a higher maximum mass configuration for a higher I. The constant rest mass sequences are investigated following quasi-stationary evolution of rotating stars. We studied both normal and supramassive cases. We notice a fall of I for normal sequences where as a sudden spin up following a spin down is observed in case of supramassive sequences. This leads to a sudden fall of I during spin down when the fall is not notable one during spin up. We have used the RNS code for these calculations.

Further we continue to study the universal relations associated with normalized I and $\mathcal{C}$ for all the considered configurations. Some earlier studies confirmed the universal relations with nucleonic constituents. Our emphasis is to study the effect of exotic components on the universal relations inside the NS core. We follow the variation of dimensionless I with $\mathcal{C}$ where we use two types of normalization for I. We notice an average deviation of around 10% from universality in higher $\mathcal{C}$ region in the case of all configurations. However, at low $\mathcal{C}$ region, universality on normalized I is witnessed irrespective of the choice of EoS. We only notice variation of $\bar{I}$ for different angular velocity values. The plots of the normalized I with $\mathcal{C}$ for fixed rest mass sequences, show a clear variation in universality in case of supramassive sequences whereas universality holds for normal sequences. Our investigations provide important information about NS moment of inertia which could be verified observationally in forthcoming years once SKA telescope starts working.

In Chapter-4, we follow the quasi-stationary evolution of the compact stars in an approximate way. We use four discrete steps for the evolution of PNS to NS. The four stages are; s_B = 1 and $Y_L = 0.4$; $s_B = 2$ and $Y_L = 0.4$; $s_B = 2$ and $Y_\nu = 0$; T= 0. Three EoSs are considered for this study namely, (i) nucleonic (HS(DD2)), (ii) hyperonic (BHBΛ) and (iii) BHB$\Lambda\phi$, that includes ϕ vector mesons as the mediator of Λ-Λ interaction. Static mass-radius profiles and temperature profiles are shown for these three EoSs. We obtain larger radius for the hotter star, which does not differ much for hyperonic EoS with or without ϕ mesons.

We have used the numerical library LORENE to study the properties of rotating NS for the isentropic as well as cold EoS. We calculate the parameters like M, R, I and Q to study the configurations up to Kepler limit for fixed baryon masses of 1.8 and $2.2M_{solar}$. All these quantities increase with spin frequency. Then, we investigate the universal relations among the dimensionless quantities like normalized I and $\mathcal{C}$. We use same normalization for I as we have used in Chapter-3. We have shown the variation of normalized I with $\mathcal{C}$ for our three EoSs with fixed frequencies 100, 300 and 500 Hz. We notice universality at lower $\mathcal{C}$ and witness a little deviation at higher $\mathcal{C}$ region which is not so prominent. We plot the relative differences in normalized I with $\mathcal{C}$ for a slowly rotating configuration that rotates with frequency 100 Hz, and notice maximum deviation for the first three evolution stages, while universality is satisfied for cold catalyzed case. We also show the relative difference plots for normalized I and $\mathcal{C}$ in case of fixed baryonic mass stars spinning at comparatively lower frequency. Here also we observe less deviation in case of cold catalyzed matter. Thus, we can conclude that the deviations in universality arise in the compact stars at the initial stages of evolution.

Finally, we study the role of antikaon condensates on the structural properties of NSs in Chapter-5. Both cold and hot EoSs are taken into consideration with nucleonic as well as exotic constituents. The static NS mass, energy density and temperature profiles are drawn by solving TOV equations. Here, we formulate the EoSs for hot stars at constant entropy per baryon values s_B= 1, 2 and 3 in units of Boltzmann constant. We calculate the M, R, I, Q and J for a star with baryon mass fixed to $2.3M_{solar}$ and show their variation with spin frequency. Similar profiles are obtained for both the considered configurations though the scenario is slight different at higher s_B.

Next, we consider the NS rotation for fixed frequencies and investigate the universal relations associated with dimensionless quantities like normalized I, normalized Q and $\mathcal{C}$. We show the variation of normalized Q with $\mathcal{C}$ and normalized I with normalized Q for a NS rotating at a fixed frequency of 600 Hz where I is normalized to I/M^3 and Q is normalized to QM/J^2. We notice EoS-independence in case of both dimensionless I and Q. The $\bar{I}$-$\mathcal{C}$ relations have been computed for the frequencies of 100 and 600 Hz. Universality relation remains valid at lower $\mathcal{C}$. However, we observe a small variation at high $\mathcal{C}$ region. This is the case for both the frequencies.

To account for the deformation of the NS, we calculate tidal deformability parameter (λ) and love number and study their variation with $\mathcal{C}$. We notice love number dependence on EoSs at

higher $\mathcal{C}$ and obtained maximum value of love number for cold EoS. On the other hand, the tidal deformability parameter λ is independent of EoSs for both high and low $\mathcal{C}$. However, we obtain high value of λ for high s_B at lower $\mathcal{C}$. But, λ is independent of both EoSs and s_B for higher compact stars. The value of λ approaches zero as the $\mathcal{C}$ becomes ~ 0.5. This value of $\mathcal{C}$ is comparable to black hole compactness.

Chapter 7

Future Perspective

The gravitational waves from colliding black holes were first detected in 2015, a hundred years after Einstein predicted its existence. The recent observation of GW170817 is a major breakthrough and stands out on its own way. It was a binary NS inspiral and its after-effect was detected by various other detectors for a longer duration in various forms of radiation, unlike the black hole mergers. This single event of 2017 has opened the door to multi-messenger astronomy providing multiple channels to constrain the EoS. The GW and its electromagnetic counterpart have constrained the NS EoS in a novel way, that the mass-radius relation and the moment of inertia-$\mathcal{C}$ universal relations could infer only within a certain limit. It has defined an upper limit of the tidal deformability that depends on the $\mathcal{C}$, hence the EoS. The lower limit was set by the kilonova signal. The limits on the tidal deformability have constrained the NS radii for the first time. The post-merger analysis of GW170817 combined with the $2M_{solar}$ observation is expected to explore physics of NS in a new and complementary way. Interpretation of observational data demands more sophisticated microphysics in the form of fully temperature-dependent EoSs, advanced neutrino evolution schemes and long term PNS evolution in our simulations.

Main sequence stars can synthesis elements only up to Fe. The dynamically ejected mass out of the NS-NS merger was theorized to undergo rapid neutron capture process (r-process nucleosynthesis) and create heavier elements, which could decay to produce the bright glow of a kilonova. The kilonova observations in the visible and infrared after GW170817 now convincingly lead us to the answer of long-standing question: Where do the heavy elements in the universe come from? The NS mergers are now confirmed as the astrophysical site where the elements heavier than iron are born. The core-collapse supernovae may stand as the birth-place of some of the heavy elements. The GW170817 data can get constraints on both the ejecta mass and the NS merger rate. More work needs to be done in order to explain the kilonova light curve, which was detected 10.9 hours after the GW event initially in blue, fast fading to red before disappearing fully. Assuming the GW rate same as that of GW170817, a small amount of high

velocity ejected mass with a low electron fraction can be modelled for r-process nucleosynthesis, that can lead to various expected colours, durations and luminosities for such transients. The numerical models with full nuclear reaction network for a wide range of parameters such as initial electron fraction, initial entropy and the expansion timescale during nuclear burning can shed light on the abundance of the heavy elements.

Bibliography

[1] W Baade and F Zwicky. "Supernovae and Cosmic Rays". In: *Phys. Rev.* 45.38 (1934), p. 138.

[2] J Robert Oppenheimer and George M Volkoff. "On massive neutron cores". In: *Physical Review* 55.4 (1939), p. 374.

[3] Richard C Tolman. "Static solutions of Einstein's field equations for spheres of fluid". In: *Physical Review* 55.4 (1939), p. 364.

[4] B Kent Harrison, Masami Wakano, and John A Wheeler. "Matter-energy at high density; end point of thermonuclear evolution". In: *La structure et évolution de l'univers* (1958), pp. 124–140.

[5] AGW Cameron. "Pycnonuclear Reations and Nova Explosions." In: *The Astrophysical Journal* 130 (1959), p. 916.

[6] THR Skyrme. "The effective nuclear potential". In: *Nuclear Physics* 9.4 (1958), pp. 615–634.

[7] EE Salpeter. "Matter at high densities". In: *Annals of Physics* 11.4 (1960), pp. 393–413.

[8] VA Ambartsumyan and GS Saakyan. "The degenerate superdense gas of elementary particles". In: *Soviet Astronomy* 4 (1960), p. 187.

[9] Sachiko Tsuruta and AGW Cameron. "Some effects of nuclear forces on neutron-star models". In: *Canadian Journal of Physics* 44.8 (1966), pp. 1895–1922.

[10] AB Migdal. "Superfluidity and the moments of inertia of nuclei". In: *Sov. Phys. JETP* 10 (1960), p. 176.

[11] Raymond F Sawyer. "Condensed π- phase in neutron-star matter". In: *Physical Review Letters* 29.6 (1972), p. 382.

[12] RF Sawyer and DJ Scalapino. "Pion condensation in superdense nuclear matter". In: *Physical Review D* 7.4 (1973), p. 953.

[13] DB Kaplan and AE Nelson. "Strange goings on in dense nucleonic matter". In: *Physics Letters B* 175.1 (1986), pp. 57–63.

[14] JD Walecka. "A theory of highly condensed matter". In: *Annals of Physics* 83.2 (1974), pp. 491–529.

[15] M Gell-Mann. "GELL-MANN 1964". In: *phys. lett* 8 (1964), p. 214.

[16] G Zweig. *CERN preprint 8182/TH401*. 1964.

[17] DD Ivanenko and DF Kurdgelaidze. "Hypothesis concerning quark stars". In: *Astrophysics* 1.4 (1965), pp. 251–252.

[18] D Ivanenko and DF Kurdgelaidze. "Remarks on quark stars". In: *Lettere al Nuovo Cimento (1969-1970)* 2.1 (1969), pp. 13–16.

[19] Isaac Vidana. "A short walk through the physics of neutron stars". In: *The European Physical Journal Plus* 133.10 (2018), p. 445.

[20] Thomas Gold. "Rotating neutron stars as the origin of the pulsating radio sources". In: *Nature* 218.5143 (1968), p. 731.

[21] Russell A Hulse and Joseph H Taylor. "Discovery of a pulsar in a binary system". In: *The Astrophysical Journal* 195 (1975), pp. L51–L53.

[22] R. N. Manchester, G. B. Hobbs, A. Teoh, and M. Hobbs. "The Australia telescope national facility pulsar catalogue". In: *The Astronomical Journal* 129.4 (2005), p. 1993.

[23] F Acernese, M Agathos, K Agatsuma, D Aisa, N Allemandou, A Allocca, J Amarni, P Astone, G Balestri, G Ballardin, et al. "Advanced Virgo: a second-generation interferometric gravitational wave detector". In: *Classical and Quantum Gravity* 32.2 (2014), p. 024001.

[24] Junaid Aasi, BP Abbott, Richard Abbott, Thomas Abbott, MR Abernathy, Kendall Ackley, Carl Adams, Thomas Adams, Paolo Addesso, RX Adhikari, et al. "Advanced ligo". In: *Classical and quantum gravity* 32.7 (2015), p. 074001.

[25] *Square Kilometre Array*. `https://www.skatelescope.org/`. (Accessed on 12/19/2018).

[26] AL Watts, R Xu, CM Espinoza, et al. "Advancing Astrophysics with the Square Kilometre Array". In: *PoS (AASKA14)* 43 (2014).

[27] Benjamin P Abbott, Rich Abbott, TD Abbott, Fausto Acernese, Kendall Ackley, Carl Adams, Thomas Adams, Paolo Addesso, RX Adhikari, VB Adya, et al. "GW170817: observation of gravitational waves from a binary neutron star inspiral". In: *Physical Review Letters* 119.16 (2017), p. 161101.

[28] J-B Wei, A Figura, GF Burgio, H Chen, and H-J Schulze. "Neutron star universal relations with microscopic equations of state". In: *arXiv preprint arXiv:1809.04315* (2018).

[29] Masaru Shibata, Sho Fujibayashi, Kenta Hotokezaka, Kenta Kiuchi, Koutarou Kyutoku, Yuichiro Sekiguchi, and Masaomi Tanaka. "Modeling GW170817 based on numerical relativity and its implications". In: *Physical Review D* 96.12 (2017), p. 123012.

[30] Rana Nandi, Prasanta Char, and Subrata Pal. "Constraining the equation of state with gravitational wave observation". In: *arXiv preprint arXiv:1809.07108* (2018).

[31] PB Demorest, Tim Pennucci, SM Ransom, MSE Roberts, and JWT Hessels. "A two-solar-mass neutron star measured using Shapiro delay". In: *nature* 467.7319 (2010), p. 1081.

[32] John Antoniadis, Paulo CC Freire, Norbert Wex, Thomas M Tauris, Ryan S Lynch, Marten H van Kerkwijk, Michael Kramer, Cees Bassa, Vik S Dhillon, Thomas Driebe, et al. "A massive pulsar in a compact relativistic binary". In: *Science* 340.6131 (2013), p. 1233232.

[33] Emmanuel Fonseca, Timothy T Pennucci, Justin A Ellis, Ingrid H Stairs, David J Nice, Scott M Ransom, Paul B Demorest, Zaven Arzoumanian, Kathryn Crowter, Timothy Dolch, et al. "The NANOGrav nine-year data set: Mass and geometric measurements of binary millisecond pulsars". In: *The Astrophysical Journal* 832.2 (2016), p. 167.

[34] Sudip Bhattacharyya. "Measurement of neutron star parameters: A review of methods for low-mass X-ray binaries". In: *Advances in Space Research* 45.8 (2010), pp. 949–978.

[35] James M Lattimer and Bernard F Schutz. "Constraining the equation of state with moment of inertia measurements". In: *The Astrophysical Journal* 629.2 (2005), p. 979.

[36] *NICER — NASA*. `https://www.nasa.gov/nicer`. (Accessed on 12/19/2018).

[37] *Athena X-ray observatory - Athena X-ray observatory*. `https://www.the-athena-x-ray-observatory.eu/`. (Accessed on 12/19/2018).

[38] SL Shapiro, SA Teukolsky, and AP Lightman. "Black holes, white dwarfs, and neutron stars: the physics of compact objects". In: *Physics Today* 36 (1983), p. 89.

[39] JWT Hessels, SM Ransom, IH Stairs, PCC Freire, VM Kaspi, and F Camilo. "A radio pulsar spinning at 716 Hz". In: *Science* 311.5769 (2006), pp. 1901–1904.

[40] M Coleman Miller and Jon M Miller. "The masses and spins of neutron stars and stellar-mass black holes". In: *Physics Reports* 548 (2015), pp. 1–34.

[41] CM Tan, CG Bassa, S Cooper, TJ Dijkema, P Esposito, JWT Hessels, VI Kondratiev, M Kramer, D Michilli, S Sanidas, et al. "LOFAR Discovery of a 23.5 s Radio Pulsar". In: *The Astrophysical Journal* 866.1 (2018), p. 54.

[42] Paweł Haensel, Aleksander Yu Potekhin, and Dmitry G Yakovlev. *Neutron stars 1: Equation of state and structure*. Vol. 326. Springer Science & Business Media, 2007.

[43] NK Glendenning. "Compact stars springer". In: *New York* (1997).

[44] Sarmistha Banik and Debades Bandyopadhyay. "Antikaon condensation and the metastability of protoneutron stars". In: *Physical Review C* 63.3 (2001), p. 035802.

[45] Sarmistha Banik and Debades Bandyopadhyay. "Density dependent hadron field theory for neutron stars with antikaon condensates". In: *Physical Review C* 66.6 (2002), p. 065801.

[46] Sarmistha Banik and Debades Bandyopadhyay. "Third family of superdense stars in the presence of antikaon condensates". In: *Physical Review C* 64.5 (2001), p. 055805.

[47] Subrata Pal, Debades Bandyopadhyay, and Walter Greiner. "Antikaon condensation in neutron stars". In: *Nuclear Physics A* 674.3-4 (2000), pp. 553–577.

[48] Madappa Prakash, Ignazio Bombaci, Manju Prakash, Paul J Ellis, James M Lattimer, and Roland Knorren. "Composition and structure of protoneutron stars". In: *Physics Reports* 280.1 (1997), pp. 1–77.

[49] Sarmistha Banik, Matthias Hempel, and Debades Bandyopadhyay. "New Hyperon Equations of State for Supernovae and Neutron Stars in Density-dependent Hadron Field Theory". In: *The Astrophysical Journal Supplement Series* 214.2 (2014), p. 22.

[50] Gordon Baym, Christopher Pethick, and Peter Sutherland. "The ground state of matter at high densities: equation of state and stellar models". In: *The Astrophysical Journal* 170 (1971), p. 299.

[51] JL Zdunik, M Fortin, and P Haensel. "Neutron star properties and the equation of state for the core". In: *Astronomy & Astrophysics* 599 (2017), A119.

[52] M Fortin, C Providência, Ad R Raduta, F Gulminelli, JL Zdunik, P Haensel, and M Bejger. "Neutron star radii and crusts: uncertainties and unified equations of state". In: *Physical Review C* 94.3 (2016), p. 035804.

[53] Daniela D Doneva, Stoytcho S Yazadjiev, Nikolaos Stergioulas, and Kostas D Kokkotas. "Breakdown of I-Love-Q universality in rapidly rotating relativistic stars". In: *The Astrophysical Journal Letters* 781.1 (2013), p. L6.

[54] Brynmor Haskell, Riccardo Ciolfi, Francesco Pannarale, and Luciano Rezzolla. "On the universality of I–Love–Q relations in magnetized neutron stars". In: *Monthly Notices of the Royal Astronomical Society: Letters* 438.1 (2013), pp. L71–L75.

[55] Kent Yagi and Nicolas Yunes. "I-Love-Q relations in neutron stars and their applications to astrophysics, gravitational waves, and fundamental physics". In: *Physical Review D* 88.2 (2013), p. 023009.

[56] Kent Yagi and Nicolás Yunes. "I-Love-Q: Unexpected universal relations for neutron stars and quark stars". In: *Science* 341.6144 (2013), pp. 365–368.

[57] JM Lattimer and M Prakash. "Neutron star structure and the equation of state". In: *The Astrophysical Journal* 550.1 (2001), p. 426.

[58] Sayan Chakrabarti, Térence Delsate, Norman Gürlebeck, and Jan Steinhoff. "I- Q Relation for Rapidly Rotating Neutron Stars". In: *Physical Review Letters* 112.20 (2014), p. 201102.

[59] Cosima Breu and Luciano Rezzolla. "Maximum mass, moment of inertia and compactness of relativistic stars". In: *Monthly Notices of the Royal Astronomical Society* 459.1 (2016), pp. 646–656.

[60] DG Ravenhall and Christopher J Pethick. "Neutron star moments of inertia". In: *The Astrophysical Journal* 424 (1994), pp. 846–851.

[61] NK Glendenning and SA Moszkowski. "Reconciliation of neutron-star masses and binding of the Λ in hypernuclei". In: *Physical Review Letters* 67.18 (1991), p. 2414.

[62] Jürgen Schaffner and Igor N Mishustin. "Hyperon-rich matter in neutron stars". In: *Physical Review C* 53.3 (1996), p. 1416.

[63] S Typel. "Relativistic model for nuclear matter and atomic nuclei with momentum-dependent self-energies". In: *Physical Review C* 71.6 (2005), p. 064301.

[64] S Typel, G Röpke, T Klähn, D Blaschke, and HH Wolter. "Composition and thermodynamics of nuclear matter with light clusters". In: *Physical Review C* 81.1 (2010), p. 015803.

[65] H Lenske and CH Fuchs. "Rearrangement in the density dependent relativistic field theory of nuclei". In: *Physics Letters B* 345.4 (1995), pp. 355–360.

[66] James M Lattimer and Yeunhwan Lim. "Constraining the symmetry parameters of the nuclear interaction". In: *The Astrophysical Journal* 771.1 (2013), p. 51.

[67] T Fischer, M Hempel, I Sagert, Y Suwa, and J Schaffner-Bielich. "Symmetry energy impact in simulations of core-collapse supernovae". In: *The European physical journal A* 50.2 (2014), p. 46.

[68] Ch Fuchs, H Lenske, and HH Wolter. "Density dependent hadron field theory". In: *Physical Review C* 52.6 (1995), p. 3043.

[69] J Schaffner, CB Dover, A Gal, C Greiner, DJ Millener, and H Stöcker. "Multiply strange nuclear systems". In: *Annals of Physics* 235.1 (1994), pp. 35–76.

[70] Norman K Glendenning and Jürgen Schaffner-Bielich. "First order kaon condensate". In: *Physical Review C* 60.2 (1999), p. 025803.

[71] A Burrows and JM Lattimer. "The birth of neutron stars". In: *The Astrophysical Journal* 307 (1986), pp. 178–196.

[72] JA Pons, S Reddy, M Prakash, JM Lattimer, and JA Miralles. "Evolution of proto-neutron stars". In: *The Astrophysical Journal* 513.2 (1999), p. 780.

[73] Jose A Pons, Sanjay Reddy, Paul J Ellis, Madappa Prakash, and James M Lattimer. "Kaon condensation in proto-neutron star matter". In: *Physical Review C* 62.3 (2000), p. 035803.

[74] Neelam Dhanda Batra, Krishna Prakash Nunna, and Sarmistha Banik. "Properties of rapidly rotating hot neutron stars with antikaon condensates at constant entropy per baryon". In: *Physical Review C* 98.3 (2018), p. 035801.

[75] M Hempel and J Schaffner-Bielich. "A statistical model for a complete supernova equation of state". In: *Nuclear Physics A* 837.3-4 (2010), pp. 210–254.

[76] Miguel Marques, Micaela Oertel, Matthias Hempel, and Jérôme Novak. "New temperature dependent hyperonic equation of state: Application to rotating neutron star models and I- Q relations". In: *Physical Review C* 96.4 (2017), p. 045806.

[77] S Typel and HH Wolter. "Relativistic mean field calculations with density-dependent meson-nucleon coupling". In: *Nuclear Physics A* 656.3-4 (1999), pp. 331–364.

[78] Tamara Nikšić, Dario Vretenar, P Finelli, and Peter Ring. "Relativistic Hartree-Bogoliubov model with density-dependent meson-nucleon couplings". In: *Physical Review C* 66.2 (2002), p. 024306.

[79] GA Lalazissis, Tamara Nikšić, Dario Vretenar, and Peter Ring. "New relativistic mean-field interaction with density-dependent meson-nucleon couplings". In: *Physical Review C* 71.2 (2005), p. 024312.

[80] Giuseppe Colucci and Armen Sedrakian. "Equation of state of hypernuclear matter: impact of hyperon–scalar-meson couplings". In: *Physical Review C* 87.5 (2013), p. 055806.

[81] Prasanta Char and Sarmistha Banik. "Massive neutron stars with antikaon condensates in a density-dependent hadron field theory". In: *Physical Review C* 90.1 (2014), p. 015801.

[82] Robert E Chrien and Carl B Dover. "Nuclear systems with strangeness". In: *Annual Review of Nuclear and Particle Science* 39.1 (1989), pp. 113–150.

[83] CB Dover and A Gal. "Hyperon-nucleus potentials". In: *Progress in Particle and Nuclear Physics* 12 (1984), pp. 171–239.

[84] T Fukuda, A Higashi, Y Matsuyama, C Nagoshi, J Nakano, M Sekimoto, P Tlustỳ, Jung Keun Ahn, H En'yo, H Funahashi, et al. "Cascade hypernuclei in the (K-, K+) reaction on 12 C". In: *Physical Review C* 58.2 (1998), p. 1306.

[85] P Khaustov, DE Alburger, PD Barnes, B Bassalleck, AR Berdoz, A Biglan, T Bürger, DS Carman, RE Chrien, CA Davis, et al. "Evidence of Ξ hypernuclear production in the 12 C (K-, K+) Ξ 12 Be reaction". In: *Physical Review C* 61.5 (2000), p. 054603.

[86] Laura Tolos, Mario Centelles, and Angels Ramos. "Equation of state for nucleonic and hyperonic neutron stars with mass and radius constraints". In: *The Astrophysical Journal* 834.1 (2016), p. 3.

[87] S Weissenborn, D Chatterjee, and J Schaffner-Bielich. "Hyperons and massive neutron stars: The role of hyperon potentials". In: *Nuclear Physics A* 881 (2012), pp. 62–77.

[88] VK Magas, Junko Yamagata-Sekihara, Satoru Hirenzaki, E Oset, and A Ramos. "Latest results for the antikaon–nucleon optical potential". In: *Few-Body Systems* 50.1-4 (2011), pp. 343–345.

[89] Éric Gourgoulhon. "An introduction to the theory of rotating relativistic stars". In: *arXiv preprint arXiv:1003.5015* (2010).

[90] John Friedman, Peter Schneider, Ramesh Narayan, Jeffrey E. McClintock, Peter Mészáros, and Martin J. Rees. "Relativistic Astrophysics". In: *General Relativity and Gravitation: A Centennial Perspective*. Ed. by Abhay Ashtekar, Beverly K. Berger, James Isenberg, and MalcolmEditors MacCallum. Cambridge University Press, 2015, 97–161. DOI: 10.1017/CBO9781139583961.005.

[91] JO Goussard, P Haensel, and JL Zdunik. "Rapid uniform rotation of protoneutron stars". In: *Astron. Astrophys* 321 (1997), pp. 822–834.

[92] M Salgado, S Bonazzola, E Gourgoulhon, and P Haensel. "High precision rotating netron star models 1: Analysis of neutron star properties". In: *Astronomy and Astrophysics* 291 (1994), pp. 155–170.

[93] George Pappas and Theocharis A Apostolatos. "Revising the multipole moments of numerical spacetimes and its consequences". In: *Physical Review Letters* 108.23 (2012), p. 231104.

[94] John L Friedman and Nikolaos Stergioulas. *Rotating relativistic stars*. Cambridge University Press, 2013.

[95] S Bonazzola, E Gourgoulhon, M Salgado, and JA Marck. "Axisymmetric rotating relativistic bodies: A new numerical approach for'exact'solutions". In: *Astronomy and Astrophysics* 278 (1993), pp. 421–443.

[96] N Stergioulas. "Rapidly rotating neutron star". In: *URL http://www. gravity. phys. uwm. edu/rns* (1997).

[97] Silvano Bonazzola, Eric Gourgoulhon, and Jean-Alain Marck. "Numerical models of irrotational binary neutron stars in general relativity". In: *Physical Review Letters* 82.5 (1999), p. 892.

[98] Thibault Damour and G Schäeer. "Higher-order relativistic periastron advances and binary pulsars". In: *Il Nuovo Cimento B (1971-1996)* 101.2 (1988), pp. 127–176.

[99] Yong Shao and Xiang-Dong Li. "FORMATION OF THE DOUBLE NEUTRON STAR SYSTEM PSR J1930–1852". In: *The Astrophysical Journal* 816.1 (2015), p. 45.

[100] M Kramer and N Wex. "The double pulsar system: A unique laboratory for gravity". In: *Classical and Quantum Gravity* 26.7 (2009), p. 073001.

[101] P Haensel, M Bejger, M Fortin, and L Zdunik. "Rotating neutron stars with exotic cores: masses, radii, stability". In: *The European Physical Journal A* 52.3 (2016), p. 59.

[102] NK Glendenning and S Pei. "NK Glendenning, S. Pei, and F. Weber, Phys. Rev. Lett. 79, 1603 (1997)." In: *Phys. Rev. Lett.* 79 (1997), p. 1603.

[103] JL Zdunik, M Bejger, P Haensel, and E Gourgoulhon. "Phase transitions in rotating neutron stars cores: back bending, stability, corequakes, and pulsar timing". In: *Astronomy & Astrophysics* 450.2 (2006), pp. 747–758.

[104] N Stergioulas and JL Friedman. "Comparing models of rapidly rotating relativistic stars constructed by two numerical methods". In: *Astrophys. J.* 444 (1995), pp. 306–311.

[105] Hidemi Komatsu, Yoshiharu Eriguchi, and Izumi Hachisu. "Rapidly rotating general relativistic stars–I. Numerical method and its application to uniformly rotating polytropes". In: *Monthly Notices of the Royal Astronomical Society* 237.2 (1989), pp. 355–379.

[106] Gregory B Cook, Stuart L Shapiro, and Saul A Teukolsky. "Rapidly rotating polytropes in general relativity". In: *The Astrophysical Journal* 422 (1994), pp. 227–242.

[107] Gregory B Cook, Stuart L Shapiro, and Saul A Teukolsky. "Rapidly rotating neutron stars in general relativity: Realistic equations of state". In: *The Astrophysical Journal* 424 (1994), pp. 823–845.

[108] AA Abdo, Markus Ackermann, Marco Ajello, B Anderson, WB Atwood, Magnus Axelsson, Luca Baldini, Jean Ballet, Guido Barbiellini, MG Baring, et al. "Detection of 16 gamma-ray pulsars through blind frequency searches using the Fermi LAT". In: *Science* 325.5942 (2009), pp. 840–844.

[109] Fridolin Weber. *Pulsars as astrophysical laboratories for nuclear and particle physics*. Routledge, 2017.

[110] Julian L Zdunik, P Haensel, E Gourgoulhon, and M Bejger. "Hyperon softening of the EOS of dense matter and the spin evolution of isolated neutron stars". In: *Astronomy & Astrophysics* 416.3 (2004), pp. 1013–1022.

[111] Sarmistha Banik, Matthias Hanauske, Debades Bandyopadhyay, and Walter Greiner. "Rotating compact stars with exotic matter". In: *Physical Review D* 70.12 (2004), p. 123004.

[112] Grégoire Martinon, Andrea Maselli, Leonardo Gualtieri, and Valeria Ferrari. "Rotating protoneutron stars: Spin evolution, maximum mass, and I-Love-Q relations". In: *Physical Review D* 90.6 (2014), p. 064026.

[113] Jose A Pons, Andrew W Steiner, Madappa Prakash, and James M Lattimer. "Evolution of proto-neutron stars with quarks". In: *Physical Review Letters* 86.23 (2001), p. 5223.

[114] JA Pons, JA Miralles, M Prakash, and JM Lattimer. "Evolution of proto-neutron stars with kaon condensates". In: *The Astrophysical Journal* 553.1 (2001), p. 382.

[115] Wolfgang Keil and H-T Janka. "Hadronic phase transitions at supranuclear densities and the delayed collapse of newly formed neutron stars." In: *Astronomy and Astrophysics* 296 (1995), p. 145.

[116] T Fischer, SC Whitehouse, Anthony Mezzacappa, F-K Thielemann, and M Liebendörfer. "Protoneutron star evolution and the neutrino-driven wind in general relativistic neutrino radiation hydrodynamics simulations". In: *Astronomy & Astrophysics* 517 (2010), A80.

[117] L Hüdepohl, B Müller, H-T Janka, A Marek, and GG Raffelt. "Neutrino signal of electron-capture supernovae from core collapse to cooling". In: *Physical Review Letters* 104.25 (2010), p. 251101.

[118] Luke F Roberts. "A new code for proto-neutron star evolution". In: *The Astrophysical Journal* 755.2 (2012), p. 126.

[119] Ilona Bednarek and Ryszard Manka. "Properties of a protoneutron star in effective field theory". In: *Physical Review C* 73.4 (2006), p. 045804.

[120] Xueling Mu, Huanyu Jia, Xia Zhou, and Hui Wang. "Effects of the and ϕ Mesons on the Properties of Massive Protoneutron Stars". In: *The Astrophysical Journal* 846.2 (2017), p. 140.

[121] Smruti Smita Lenka, Prasanta Char, and Sarmistha Banik. "Critical mass, moment of inertia and universal relations of rapidly rotating neutron stars with exotic matter". In: *International Journal of Modern Physics D* 26.11 (2017), p. 1750127.

[122] Veronica Dexheimer and Stefan Schramm. "Proto-neutron and neutron stars in a chiral SU (3) model". In: *The Astrophysical Journal* 683.2 (2008), p. 943.

[123] Loic Villain, Jose A Pons, Pablo Cerdá-Durán, and Eric Gourgoulhon. "Evolutionary sequences of rotating protoneutron stars". In: *Astronomy & Astrophysics* 418.1 (2004), pp. 283–294.

[124] Tanja Hinderer. "Tidal Love numbers of neutron stars". In: *The Astrophysical Journal* 677.2 (2008), p. 1216.

[125] Tanja Hinderer, Benjamin D Lackey, Ryan N Lang, and Jocelyn S Read. "Tidal deformability of neutron stars with realistic equations of state and their gravitational wave signatures in binary inspiral". In: *Physical Review D* 81.12 (2010), p. 123016.

[126] Smruti Smita Lenka, Prasanta Char, and Sarmistha Banik. "Properties of Massive Rotating Protoneutron Stars with Hyperons: Evolution and Universality". In: *arXiv preprint arXiv:1805.09492* (2018).

List of Publications

From Thesis Work

1. Smruti Smita Lenka and Sarmistha Banik, "Role of antikaon condensation on the universality relations of hot and rapidly rotating neutron stars", (manuscript under review).

2. Smruti Smita Lenka, Prasanta Char and Sarmistha Banik, "Properties of Massive Rotating Protoneutron Stars with Hyperons: Structure and Universality", (manuscript under review) [arXiv:1805.09492].

3. Smruti Smita Lenka, Prasanta Char and Sarmistha Banik, "Critical mass, moment of inertia and universal relations of rapidly rotating neutron stars with exotic matter", *International Journal of Modern Physics D* **26** 11, 1750127, 2017**.**

From Other Work

1. Smruti Smita Lenka, B. Hareesh Gautham and Sarmistha Banik, "Nucleosynthesis in Neutron Stars Crust", *Journal of Nuclear Physics, Material Sciences, Radiation and Applications* **3,** 1, 103–109, 2015**.**

Conference Proceedings

1. Smruti Smita Lenka and Sarmistha Banik, "Moment of inertia of massive rotating protoneutron stars with hyperons: Evolution and Universality", *DAE Symposium on Nuclear Physics* **63** 796–797, 2018**.**

2. Smruti Smita Lenka, Prasanta Char and Sarmistha Banik, "Universality of different properties of rotating neutron stars with realistic equation of state", *DAE Symposium on Nuclear Physics* **61** 928–929, 2016**.**

3. Smruti Smita Lenka, B. Hareesh Gautham and Sarmistha Banik, "Nucleosynthesis in decompressed Neutron stars crust matter"**,** *DAE Symposium on Nuclear Physics* **60** 844–845, 2015**.**

Participation in Seminar and Workshops

1. 30^{th} meeting of the Indian Association for General Relativity and Gravitation(IAGRG) on "New Eras in Cosmology and Multi-messenger Astronomy" held at BITS-Pilani, Hyderabad, India, January-2019.

2. Young Physicists Colloquium held at Saha Institute of Nuclear Physics, Kolkata, India, August-2018.

3. Pulsar Astronomy with uGMRT Boot-Camp and Multi-wavelength Neutron Star Workshop held at BITS-Pilani, Hyderabad Campus, India, January -2018.

4. Neutron Stars: A Pathfinder Workshop held at NCRA-TIFR, Pune, India, January-2016.

5. 60^{th} DAE-BRNS symposium on Nuclear physics held at SSSIHL, Prasanthi Nilayam, Andhra Pradesh, India, December-2015.

6. Winter School on Nuclear astrophysics held at VECC, Kolkata, India, January-2015.

7. Winter School on Accelerator, Nuclear and Particle physics at BHU, Varanasi, India, March-2014.

Biography of Smruti Smita Lenka

Ms. Smruti Smita Lenka completed her Bachelor of Science (Physics) in the year 2010 from Utkal University, Odisha, India. She completed her Master of Science (Applied Physics and Ballistics) in the year 2012 from Fakir Mohan University, Odisha, India. She did Master of Philosophy (Physics) from Fakir Mohan University, Odisha, India in the year 2012-2013. Ms Lenka joined Departmnet of Physics, Birla Institute of Technology and Science-Pilani, Hyderabad Campus as a DST-INSPIRE fellow in the year 2014 to carry out her doctoral research work under the supervision of Prof. Sarmistha Banik. She was upgraded to Senior Research Fellow in the year 2017 through DST-INSPIRE JRF to SRF upgradation assessment. She has presented her research work in different scientific conferences and attended various workshops related to her research area.

Biography of Prof. Sarmistha Banik

Dr Sarmistha Banik is presently working as an Associate Professor in the Department of Physics, Birla Institute of Technology and Science, Pilani, Hyderabad Campus. She has also been a visiting associate at the Inter-University Center for Astronomy & Astrophysics (IUCAA), Pune, India since 2015. She got PhD degree from Calcutta University and pursued her postdoctoral studies at School of Physics & Astronomy, University of Manchester, UK. Dr Banik is an Alexander von Humboldt Fellow and worked as a guest scientist at Frankfurt Institute for Advanced Studies, Germany with Humboldt fellowship. She is involved in neutron star research for the last 20 years. She has published more than 30 research articles and delivered invited lectures at various national and international institutions. Prof. Banik has visited many reputed institutes in the world and established joint collaborations. Her small research group comprising of research scholars and postdoctoral fellows have successfully hosted national level workshop on neutron stars. Teaching physics is a passion that Prof. Banik takes a keen interest in.